NISTIR 6075

PB98-108707

Cumulative Seismic Damage of Reinforced Concrete Bridge Piers

Sashi K. Kunnath
Ashraf El-Bahy

University of Central Florida
Orlando, Florida 32816

Andrew W. Taylor
William C. Stone

Building and Fire Research Laboratory
Gaithersburg, Maryland 20899

United States Department of Commerce
Technology Administration
National Institute of Standards and Technology

NISTIR 6075

Cumulative Seismic Damage of Reinforced Concrete Bridge Piers

Sashi K. Kunnath
Ashraf El-Bahy
Andrew W. Taylor
William C. Stone

October 1997

Building and Fire Research Laboratory
National Institute of Standards and Technology
Gaithersburg, MD 20899

U.S. Department of Commerce
William M. Daley, *Secretary*
Technology Administration
Gary R. Bachula, *Acting Under Secretary for Technology*
National Institute of Standards and Technology
Robert E. Hebner, *Acting Director*

Abstract

A comprehensive experimental study was undertaken in this research effort to investigate cumulative damage in reinforced concrete circular bridge piers. Twelve identical quarter-scale bridge columns, designed and fabricated in accordance with current AASHTO specifications, were tested in two phases. Phase I testing consisted of benchmark tests to establish the monotonic force-deformation envelope, the energy capacity under standard cyclic loads, and constant amplitude tests to determine the low-cycle fatigue characteristics of the bridge column. Phase II testing was composed of a series of analytically predicted displacement amplitudes representing the bridge response to typical earthquakes. The results of Phase I testing provided information on the fatigue behavior of reinforced concrete and Phase II provided data on the effects of load path on cumulative damage.

Test observations indicate two potential failure modes: low cycle fatigue of the longitudinal reinforcing bars; and confinement failure due to rupture of the confining spirals. The former failure mode is associated with relatively large displacement amplitudes in excess of 4% lateral drift while the latter is associated with a larger number of smaller amplitude cycles. The results of the testing were also used in an analytical study of cumulative damage. It was found that none of the currently available damage models consistently predict observed damage limit states though fatigue-based models demonstrated better reliability. It was further observed that the energy-dissipation capacity of members is path-dependent, hence, models of seismic damage that rely only on measures of energy dissipation cannot predict failure if it is not related to ductility. Findings from this study will provide additional input into the development of performance-based design specifications wherein design is linked to damage limit states.

Keywords: bridges; columns; confinement; cyclic load; ductility; energy capacity; experimental testing; low-cycle fatigue; modeling; reinforced concrete; seismic damage.

Acknowledgements

Financial support for this project provided by the National Center for Earthquake Engineering Research (NCEER), the Federal Highway Administration (FHWA), and the California Department of Transportation (CALTRANS) is gratefully acknowledged. The following individuals are recognized for being instrumental in supporting and coordinating this project: at NCEER Dr. Ian Buckle, Dr. John Mander and Mr. Ian Friedland; at FHWA Mr. James Cooper and Dr. Phillip Yen; and at CALTRANS Mr. James Roberts and Mr. James Gates.

In addition, special thanks are due to the technical staff in the Structural Testing Laboratory at the National Institute of Standards and Technology - Steve Johnson, Frank Rankin, Erik Anderson, Max Peltz and James Little - whose assistance was critical in completing the experimental phase of this study.

Table of Contents

List of Figures

List of Tables

1.0 INTRODUCTION

The failure of numerous structures during the 1971 San Fernando earthquake ushered in a new era of seismic design. It recognized the need to detail critical sections for ductility so that the imposed seismic forces may be resisted by the ability of these sections to dissipate energy. Past and current design practices are being put to the test regularly with each severe earthquake. Each failure points to either a flaw in the basic design approach or a lack of understanding of the inelastic behavior of structural systems resulting from seismic loads.

The function of a structure during and after an earthquake usually dictates the methodology employed in the design of the structure. Lifeline structures, such as bridges, are assigned a much higher "importance" factor in the design process since these structures are "essential facilities" necessary for emergency operations subsequent to an earthquake. Such structures should resist minor earthquakes without damage, moderate earthquakes without significant structural damage, and in the case of a major earthquake, some structural and non-structural damage is allowed, provided it does not affect the functioning of the structure after the earthquake.

Damage to bridge structures in past earthquakes have been significant. The 1971 San Fernando earthquake significantly damaged as many as forty-one bridges. More recently, the 1989 Loma Prieta earthquake caused over $5.5 billion in damage of which almost a third was attributed to highway failures, the most notable of course being the collapse of a section of the Cypress viaduct (Housner, 1990). Post-earthquake reconnaissance and follow-on research studies have indicated that most of the damage in highway bridges is a result of some or all of the following reasons: (a) insufficient column ductility and/or energy dissipation capacity to sustain the large imposed lateral displacements; (b) insufficient shear capacity in short columns; and (c) lack of adequate anchorage length in the longitudinal reinforcing bars of the piers.

Pre-1950 highway construction (of which the Cypress viaduct is an example) in seismic zones which followed either CALTRANS or AASHTO had very low seismic requirements compared to those for buildings which used the Uniform Building Code (UBC). Despite many changes in seismic design codes over the years, the basic philosophy behind prescribing design guidelines have remain unchanged. For example, past and current AASHTO specifications for the seismic design of bridge columns have taken a generally prescriptive approach. That is, the specifications place constraints on such factors as material properties, minimum reinforcement or confinement requirements, and column geometry, without specifically linking these requirements to the performance of the column when it is subjected to a particular earthquake. A designer who follows the prescriptive code requirements is ostensibly assured that the structural safety of the bridge pier will be preserved under maximum likely earthquakes at the bridge site. However, the designer cannot make a clear or precise decision on the amount of damage suffered by the bridge column under small or moderate earthquakes. The larger issue of seismic safety under future earthquakes, as well as the criteria to be used in upgrading, remains unresolved.

Much of the strength and deformation requirements in current highway bridge design procedures have been derived from experimental testing and limited analytical studies. However, it must be noted that most of the testing conducted in the past was directed towards the objective of understanding post-yield behavior under cyclic load reversals to develop detailing strategies to

ensure satisfactory performance under seismic action. As such, these tests have provided pertinent knowledge regarding the effects of various important parameters, such as the influence of varying axial forces, the presence of high shear, confinement, and multidirectional loading, on the failure of reinforced concrete components. Issues related to performance or correlation of observed behavior to damage have not been addressed directly, hence efforts related to calibrating damage models have not met with any success. Additionally, a number of analytical models to predict seismic damage have been proposed by many researchers. These models, either derived from or verified against results of past laboratory testing of RC components and structures, have offered some clues on the factors affecting damage but fall short of the objective of assessing structural integrity in terms of serviceability and reparability.

A major factor that has hindered the development of a performance-based design methodology is the fact that no systematic experimental program has yet been undertaken wherein the imposed loading, the system variables, and the measured or observed response were tailored to specifically monitor, model and calibrate cumulative seismic damage.

1.1 Research Issues

The motivation for this research study stems from the following questions:

- Is it possible to predict failure in highway bridges due to a potential earthquake event, in the context of the damage model theories to be found in the literature ?
- Is it possible to predict the associated mode of failure ?
- Can damage models be used to measure level of performance, or reserve capacity in a structural member, following a seismic event ?
- Can the predicted "level of performance" or "reserve strength" be used to assist engineers in deciding between rehabilitation, retrofit and demolition ?
- Is energy capacity of a member independent of the applied load history, or is it load path dependent ?
- Can damage estimates be related to simple measurable quantities such as dissipated energy, ductility and the loss of strength or stiffness ?

1.2 Research Objectives and Scope of Study

Numerous analytical and experimental studies have been conducted in the past to study the inelastic response of typical bridge piers. The objective in such studies, as pointed out in the previous sub-section, has been to quantify the influence of certain material or system parameters (level of axial load, amount of transverse reinforcement, etc.) on the cyclic response of columns. Very few experimental programs have been designed to reproduce observed failure modes in bridge piers. Another issue that has received very little attention is the effect of load path on the response and failure of typical components and subassemblages. Almost without exception, imposed displacement histories in standard cyclic tests are based on a fixed number of reversed cycles applied at increasing levels of ductility until failure.

While this work is concerned with the behavior of bridge piers in general, it was decided to focus initially on the response of circular piers which have the advantage of possessing fairly uniform

properties about any arbitrary cross-section. It was considered important to keep other system variables to an absolute minimum so that the effects of load path on the structural response could be isolated.

This research endeavor is concerned primarily with load path and the effect of ductility on energy dissipation capacity. It is also concerned with identifying criteria for low-cycle fatigue and the role of confinement, as prescribed in modern codes, in altering flexural failure modes. Ultimately, the results of this study will contribute to the overall task of damage modeling and the prediction of flexural failure modes.

The primary objectives of the study may be summarized as follows:

1. Develop an experimental program dedicated to the study of progressive damage in bridge piers through an examination of critical damage parameters such as ductility, low-cycle fatigue, energy-dissipation capacity and loss of confinement due to repeated cyclic loads resulting from earthquake motions.
2. Study the influence of ductility on energy dissipation capacity of members.
3. Study the effects of random cyclic loads and load path on the cumulative damage of bridge piers.
4. Correlate visually observed damage with damage-limit states.
5. Investigate existing models of cumulative damage against observed behavior, and identify the relationship between damage parameters and observed failure modes.
6. Suggest an alternate test method, using random displacement cycles or some combination of equivalent ductility cycles, which reflect realistic displacement histories under imposed seismic motions.
7. Suggest further studies, based on the findings of this work, to address issues related to damage prediction and the development of performance-based design criteria for highway bridges.

1.3 Organization of Report

The remainder of this report is organized into six sections. Section 2 begins with an overview of past work on experimental investigations on the seismic response of bridge piers. This is followed by details of the test setup and various aspects of the design and construction of the model specimens. Section 3 presents the analytical model of the bridge pier, calibration of the hysteresis model used in the analyses, validation of the dynamic response of the scaled model specimen, and the process of generating the random displacement histories used in the second phase of the testing. The results of Phase I testing are summarized in Section 4. The testing is composed of two phases: in the first phase, two benchmark tests consisting of monotonic loading and a standard cyclic load is followed by constant amplitude fatigue-type loading. The second phase of testing, reported in Section 5, is devoted exclusively to random load tests. Various existing theories of damage are examined in Section 6. A few selected models, representing distinct approaches to damage indexing are applied to the results of the test program. Relevant findings from the study and suggestions for additional work are discussed in the seventh and final section.

2.0 DESIGN OF TESTING PROGRAM, SETUP AND INSTRUMENTATION

The objectives set forth in Section 1 of this report were addressed as part of a comprehensive study on cumulative damage of bridge piers under seismic loads. It was considered appropriate to begin on a simple scale: hence flexural columns with circular cross-sections were used in the testing. While the literature is abundant with cyclic tests on columns, both circular and rectangular, it does not provide the essential information needed to calibrate damage. Dynamic loads, such as those imposed by an earthquake, are random. The effect of such randomness, wherein large amplitude cycles are interspersed with innumerable small amplitude cycles, on the response of structures is unclear.

This project is an attempt to correlate observed damage with well recognized damage parameters. As such, a new test methodology using random cycles is proposed. Prior to describing the experimental program, a brief overview of previous experimental work in bridge testing is presented.

2.1 Review of Previous Experimental Work

The earliest tests on bridge columns under simulated seismic loads were carried out in Japan and New Zealand. Davey (1975) tested three 1:3 scale model piers with different shear span ratios. Numerous cyclic tests were conducted by the Building Research Institute (1975, 1978) in Japan on columns bent in double curvature. The first shaking table study was conducted by Munro et al. (1976) on a 1:6 scale model pier. Since then, a number of additional experiments have been carried out in Japan, New Zealand and the United States on the inelastic shear and flexural behavior of bridge columns, the most significant of which are summarized below.

Mander et al. (1984, 1988) tested the first large scale square hollow bridge piers under lateral cyclic loading. They attempted to experimentally establish the ductility capacity of hollow bridge piers that are commonly used in New Zealand. A theoretical stress-strain model for confined concrete was developed. The model took into consideration the effects of confinement, shear deformation and strain rate. Confinement was modeled by equating the strain energy required to first fracture the lateral reinforcement with the strain stored in concrete due to confinement. It was determined that the main parameter that controlled the ductility capacity of the columns was the amount of the lateral reinforcement.

Ang et al. (1985, 1989) investigated the shear strength of circular bridge piers subjected to seismic action. Twenty five one-third scaled model columns with aspect ratios of 1.5, 1.75, 2.0 and 2.5 were tested under a sequence of imposed displacements.

Stone et al. (1989, 1990) tested the first set of full scale bridge piers under combined quasi-static cyclic lateral and axial loading at the National Institute of Standards and Technology (NIST). The full scale columns had aspect ratios of 6 and 3, to simulate flexural and shear behavior, respectively. Both columns were designed to meet CALTRANS specifications for seismic loads. The loading history used on both columns were standard ductility-based displacement inputs. The study concluded that the predicted ductility capacity based on the New Zealand code

(NZ-3101) was higher than that actually observed during the experiment. It was also observed in both the flexure and shear specimens that the energy dissipated below a certain threshold displacement stabilized without substantial decrease in load carrying capacity. The testing indicated that the design requirements of CALTRANS were sufficient to provide a ductility of 6 for flexural bridge piers.

A parallel series of testing at NIST consisted of six circular model columns with a 1:6 ratio compared to the full scale columns (Cheok and Stone, 1986, 1990). The variables in the study were the load history, concrete mix and size of aggregate. It was concluded that the CALTRANS design specifications for embedment length of longitudinal bars inside the footings are adequate to prevent pullout failure. Fracture of the spiral reinforcement and buckling of the longitudinal bars occurred at displacement ductilities beyond ten for flexural columns, and above five for the shear columns. The observed moment capacity during the tests were higher by 10% - 25% than those predicted by ACI procedures (ACI-318, 1989). Higher displacement ductilities were observed on increasing the axial load. But no so-called "threshold displacement" was observed similar to that of the full scale columns.

Wong et al. (1990, 1993) tested sixteen 400 mm diameter columns with an aspect ratio of 2. The objective of the testing was to determine the strength and the deformation capacity of columns primarily in shear. The displacement pattern of the first column was uniaxial cyclic loading. Of the remaining, fourteen columns were tested under different sequence of biaxial cyclic loading. The sixteenth column was tested under random cyclic loading. The axial load ranged between $0.10 - 0.39 f_c'$. This work concluded that biaxial loading patterns led to more severe stiffness degradation than uniaxially imposed loads. The hysteretic response and the ductility capacity were distinctly improved by increasing the volume of spiral reinforcement. The elastic shear deformation of squat circular columns was determined to be significant enough that it should be considered in the initial estimation of the stiffness so that dependable ductility and drift values are established.

The adequacy of interlocking spiral reinforcement has been investigated by Tanaka and Park (1993) who conclude that the specifications of CALTRANS (1990) for this type of confinement is sufficient to ensure reliable behavior under cyclic loads compared to similar specimens with rectangular hoops and cross-ties. Recently, Priestley and Benzoni (1996) tested two large-scale circular columns with low longitudinal reinforcement ratios. One of the columns had 0.5% longitudinal steel while the second column had 1%, which represents 50% and 100% of the minimum reinforcement requirement by ACI. Both columns performed well, pointing to the possibility that the ACI minimum requirements for flexure can be further reduced.

Additionally, there have been a number of tests conducted at the University of San Diego examining retrofit of columns and bridge bents. Priestley et al. (1993a, 1993b) tested a half-scale model of a typical section of a double-deck viaduct under simulated seismic loading. The 90,000 kg model was controlled by fourteen hydraulic actuators and represents one of the most complex civil structures ever tested. The test was used to validate capacity design procedures that were proposed to retrofit existing double-deck bents in the California freeway system following the collapse of the Cypress viaduct in the 1989 Loma Prieta earthquake. Later, Priestley et al. (1994) conducted large-scale tests of as-built rectangular and circular columns and

companion specimens with steel jacket retrofit. All as-built columns failed in shear at low ductility levels (less than 3.0), while similar columns with steel jackets achieved ductility ratios in excess of 8.0.

While such tests provided invaluable insight into performance of RC members and some information on damage mechanisms, they fail to provide the kind of fundamental information necessary to calibrate seismic damage. Also, most of the above mentioned laboratory testing of components usually involve large inelastic reversals with unrealistic drift demands. Any attempt to calibrate a damage model using such tests cannot be applied to real structures wherein the sequence, magnitude and reversals are arbitrary. Evidence to this is provided by Hwang and Scribner (1984) who were the first and perhaps only investigators to study the effect of variations in displacement history. They clearly conclude that methods previously used to calculate energy dissipation capacity of members (for standard cyclic tests) do not predict consistently the cyclic capacity of a flexural member subjected to an arbitrary displacement history. This is despite the fact that the tests conducted by Hwang and Scriber were not truly random, but a small variation from the customary process in which they alternated cycles of low ductility with cycles of larger ductility demand.

Based on the current state-of-the-art in experimental dynamics of reinforced concrete, it is obvious that the literature is lacking in data on RC behavior which examines failure as a low-cycle fatigue phenomena or the consequence of random load paths on the energy dissipation capacity of specimens. A new test program is, therefore, proposed to address these important issues. The proposed scheme will include characteristics of RC member response under realistic seismic action. These will include, but are not limited to: (1) arbitrary displacement history; (2) duration and sequence of applied histories; (3) relative magnitudes of successive histories; and (4) the effect of ductility on energy dissipation capacity.

2.2 Details of Testing Program

As indicated earlier, the test program was designed to keep material, geometric and section variables to a minimum. Since different failure modes may result in different critical damage parameters, only flexural failure modes were considered in this study. The experimental program was composed of testing twelve quarter-scale circular reinforced concrete columns. Only dimensional scaling was considered and material properties were kept constant in both the model and the prototype. In keeping with the main objectives of the study, the primary variables considered were the amplitude, sequence and type of loading pattern. Two specimens were used for benchmark testing: the first specimen was loaded monotonically and unidirectionally up to failure, and the second specimen was subjected to a standard quasi-static cyclic load. Four specimens were tested for fatigue characteristics under constant amplitude cycling. The final set of six specimens were subjected to random displacement histories.

In subsequent sections, details of the prototype and model design, scaling considerations, test setup, material properties, construction and assembly of specimens, instrumentation and data acquisition are described.

2.2.1 Design of Prototype Circular Bridge Pier

A full scale single-bent bridge pier was designed to specifications of the CALTRANS (1990) code though the same design can be achieved using AASHTO (1994). The CALTRANS design procedure assumes a linear elastic, lumped mass and space frame model subjected to a design spectral acceleration. This design response spectrum uses three factors: *A*, the peak rock acceleration determined from records of fault activity and attenuation data; *R*, the peak spectral acceleration based on actual recorded earthquake data; and *S*, the soil amplification factor. The equivalent static force for design also incorporates a ductility/risk reduction factor, Z. The product of A*R*S yields an elastic response spectra curve for the site which represents the maximum credible seismic event corresponding to the closest active fault.

The design procedure involves the determination of "T", the natural period of the single bent column from:

$$T = 2\pi \sqrt{m / K} \tag{2-1}$$

where m is the mass of the bridge deck $(= W / g)$ and K is the lateral stiffness of the bridge pier.

$$W = 0.1 * f_c' * A_g \tag{2-2}$$

$$K = \frac{3EI}{L^3} \tag{2-3}$$

where A_g is the gross cross-sectional area, E is the Young's Modulus of the concrete, I is the moment of inertia and L is the height of the bridge.

Assuming a 28-day concrete compressive strength of *27.6 MPa*, column diameter $D = 1.22\ m$ and length $L = 5.5\ m$, we get $W \approx 3225\ kN$ and $T = 0.515\ sec.$ Using $A = 0.3\ g$ and *0 - 3 m* alluvium for the soil parameter, the static coefficient for the acceleration response spectrum, $ARS = 0.7$. The design lateral force is determined from:

$$F = ARS * W / Z \tag{2-4}$$

Taking $Z = 6$ for a well confined single bent ductile column, the design lateral load $F = 376\ kN$. Using CALTRANS *Pn-Mn* interaction diagrams, it is required to use 2% reinforcing steel ratio which is equivalent to 24 # 11. The spirals were designed using a plastic moment (M_p) of 130% of the balanced moment (M_b) as follows.

$$M_p = 1.3\, M_b = 1.3 * 6570\ kN - m \tag{2-5}$$

$$V_p = \frac{M_p}{L} = 1550\ kN \tag{2-6}$$

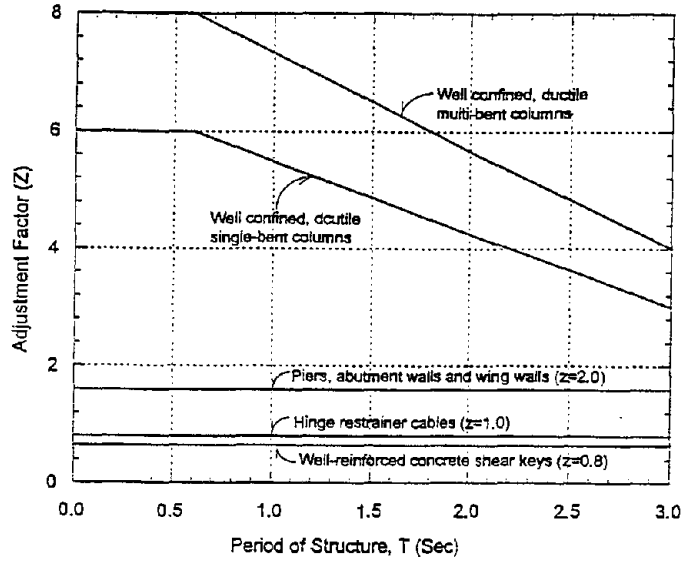

Adjustment for Ductility and Risk Assessment

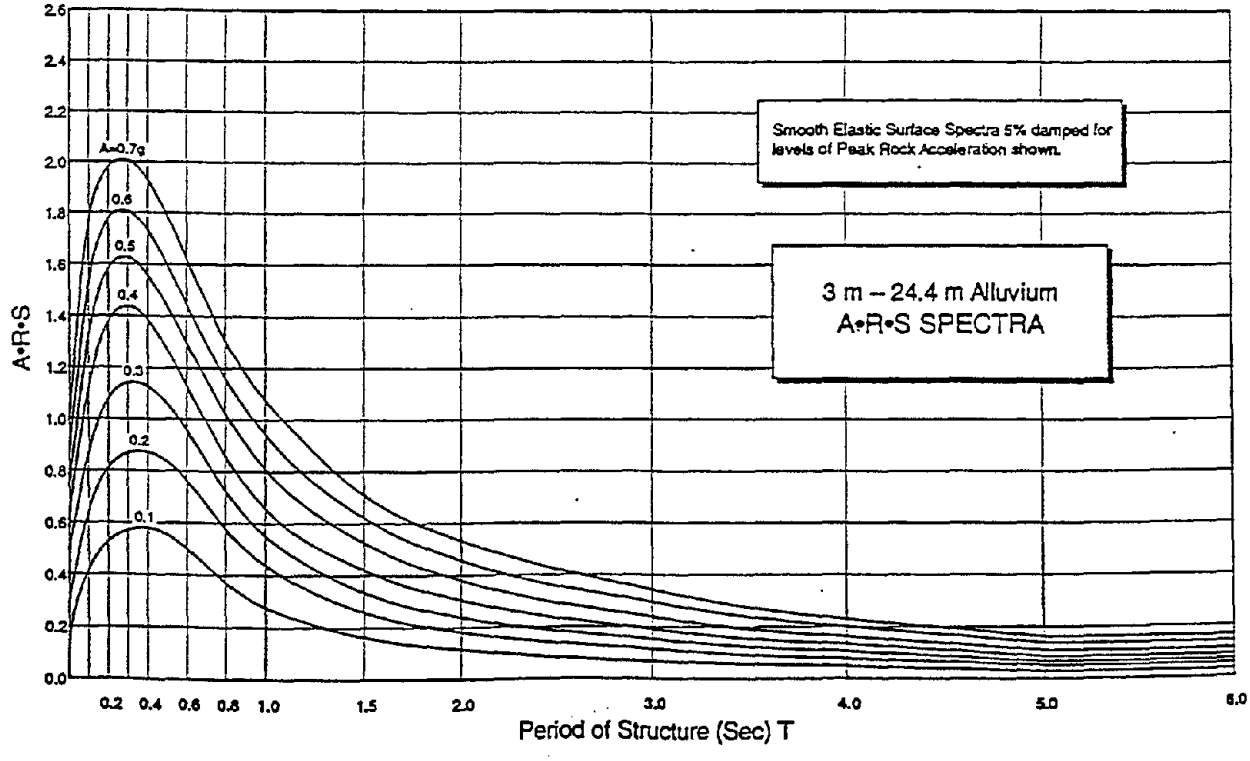

FIGURE 2-1 CALTRANS Design Spectra Used in Prototype Design

$$V_p = V_c + V_s \tag{2-7}$$

$$V_c = 0.166\sqrt{f_c'}\, b_w\, d = 1100\, kN \tag{2-8}$$

where b_w is taken as the column diameter and d is the distance from the centroid of the longitudinal reinforcement to the extreme compression fiber. The minimum shear reinforcement is given by the following expression:

$$\rho_{s\,min} = 0.45\left(\frac{A_g}{A_c} - 1\right)\frac{f_c'}{f_y} = 1\% \tag{2-9}$$

where A_c is the area of the confined core. Using # 5 (16 mm) bars for ties, the required spacing was approximately 75 mm.

2.2.2 Design of Model Specimen

The model scale was dictated by several factors: (1) available actuators for application of vertical and lateral loads; and (2) minimum size for which primary reinforcement could be scaled without use of special model materials. A quarter scale model was selected as an appropriate size for which no special modeling treatment was necessary. Only dimensional scaling was used. Material properties were selected to match those of the prototype. Table 2-1 shows the dimensions, reinforcement details, applied axial load and lateral load capacity for both the prototype and the model.

TABLE 2-1 Details of Prototype and Model

ITEM	PROTOTYPE	MODEL	REMARKS
Longitudinal Steel	24 # 11 (36 mm)	21 # 3 (9.5 mm)	$\rho = 2\,\%$
Spirals	# 5 (16 mm)	wire = 4 mm dia.	
Spiral Pitch	76 mm	19 mm	
Spiral Yield Strength	414 MPa	380 - 450 MPa	
Column Diameter	1.22 m	0.3 m	Scale 1:4
Column Length	5.5 m	0.32 m	Scale 1:4
Cover	50 mm	12.5 mm	Scale 1:4
Embedment length	Tension = 1.4 m Comp. = 0.72 m	Tension = 0.35 m Comp. = 0.18 m	
Axial Load	3225 kN	806 kN	$0.1\, f_c' A_g$
Lateral Load Capacity	1550 kN	388 kN	$V_p = M_p / L$
Spacing of long. steel	100 mm	25 mm	

2.2.3 Material Properties

Similitude relationships require that the model materials must have the same stress-strain characteristics as the prototype. This was achieved easily for the main longitudinal reinforcement. However, the column ties could not be scaled adequately using available steel. Some heat treatment was required to alter the characteristics of commercially available wire reinforcement to achieve proper similitude requirements.

2.2.3.1 Properties of Reinforcing Steel

The reinforcing steel used in the bridge pier construction was Grade 60 reinforcing bars. At a scale of 1:4, the model pier required 9.5 mm (# 3) Grade 60 longitudinal bars conforming to ASTM A615-90, which was not a problem since this size is commercially available. Figure 2-2 shows typical stress-strain curve of the #3 bars used as main longitudial reinforcement. However, for the hoop reinforcement, the dimensional scaling resulted in the use of 4 mm diameter wires. These wires do not have the specified yield strength (414 MPa) of the prototype nor a yield plateau similar to the # 3 (9.5 mm) bars that were used as spirals for the full scale bridge pier. The gage wire had to be annealed through extensive heat treatment of the cold formed wires. After several laboratory oven heat tests of samples, a temperature of approximately 565°C to 577°C was used to heat treat the spiral wires. This heat treatment produced a wire yield strength of 380 MPa to 450 MPa with similar yield characteristics of Grade 60 bars. Figure 2-3 displays the achieved stress-strain behavior of the annealed wire used as confining spirals following heat treatment. The footings and the end blocks were reinforced with # 5 bars conforming to ASTM 615-90. Figure 2-4 shows the stress strain relationship for the #5 rebar used in the footings and end blocks.

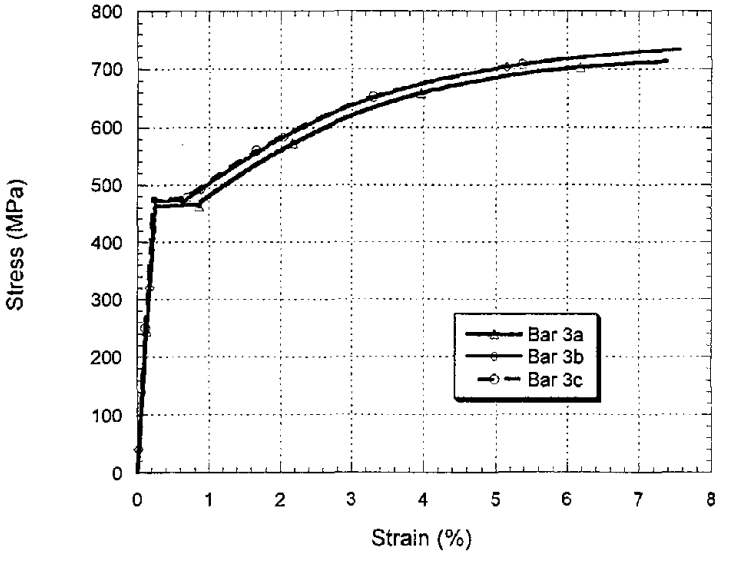

FIGURE 2-2 Stress vs. Strain Curve for #3 Longitudinal Steel

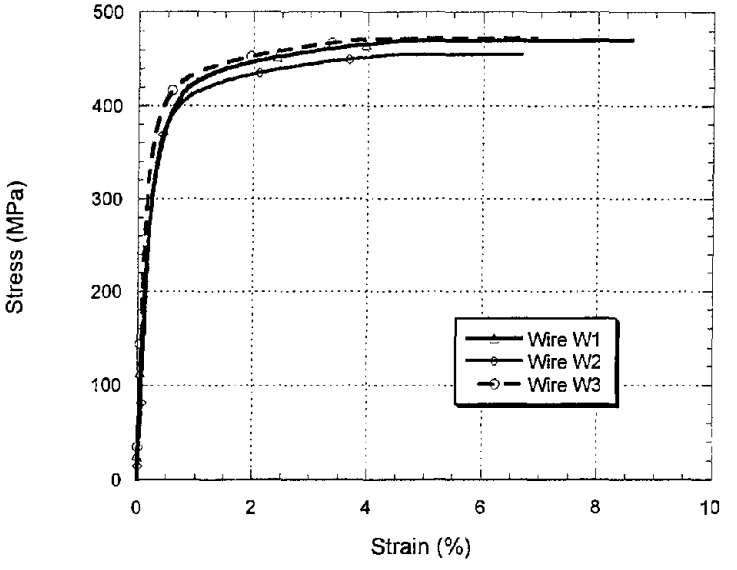

FIGURE 2-3 Stress vs. Strain Behavior of Annealed Wire Used for Spirals

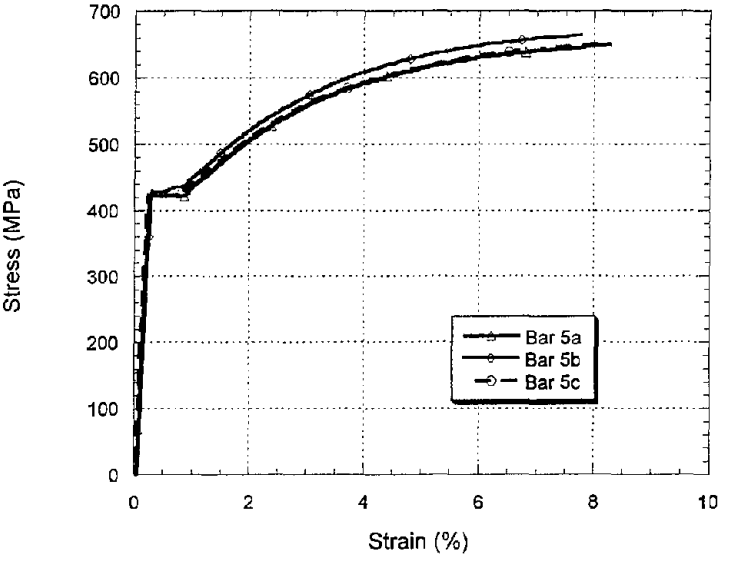

FIGURE 2-4 Stress-Strain Curve for # 5 Rebars Used in Footings and End Blocks

The stress-strain curves presented in Figures 2-2 through 2-4 do not include the fracture strain. The extensometers used to measure the specimen elongation had to be removed prior to fracture to prevent damage to the instrument. However, the total elongation of the gage length was measured, the resulting final strain calculated, and these results are tabulated in Table 2-2. The energy to fracture was computed by assuming that the stress-strain diagram was linear from the last instrumented strain reading to the fracture strain. Assuming that a typical hoop bar exhibits characteristics similar to a 9.5 mm (#3) or a 16 mm (#5) bar, strength and ductility parameters obtained for the annealed steel wire may be considered acceptable in terms of fracture energy and peak strength with variations not exceeding 15 to 20%. Additionally, there is no well-distinguished ultimate strain because of the lack of a yield plateau and strain hardening regime. A comparative summary of the different rebar test results is displayed in Table 2-2.

TABLE 2-2 Summary of Rebar Characteristics

SPECIMEN		f_y	E_s	f_{su}	ε_{su}	ε_{sf}	E_{fr}
Group	No.	*(MPa)*	*(MPa)*	*(MPa)*	*(%)*	*(%)*	*(MPa)*
Rebar	3a	463	213,500	733	8.5	14.6	9,925
	3b	472	215,900	714	9.7	13.8	9,095
	3c	476	227,300	723	7.9	15.7	10,659
Wire	W1	419	234,600	471	-	17.5	8,044
	W2	407	210,900	455	-	19.1	8,501
	W3	398	216,100	475	-	16.9	7,840
Rebar	5a	422	220,600	650	8.2	16.9	10,270
	5b	430	226,100	664	7.7	17.3	10,580
	5c	423	203,200	656	8.3	16.2	9,772

Notations: f_y = Yield stress ; E_s = Young's modulus
f_{su} = Ultimate (peak) stress
ε_{su} = Strain at peak stress
ε_{sf} = Fracture strain ; E_{fr} = Fracture Energy

2.2.3.2 Concrete Properties

In order to ensure monolithic reinforced concrete specimens, the columns were poured with footings at the same time. All the specimen were cast in an inverted position, as described later. This required a concrete with an average slump of 8 inches and a maximum aggregate size of 1/2 inch. The specimens were cast in two batches of six specimens each. The cement used in the concrete mix was Portland Blast Furnace slag cement, Type IS, meeting ASTM C599-85 specifications and the requirements of ACI 318 and 301. The fine aggregate used was concrete sand meeting requirements of ASTM C-33-90. The coarse aggregate used was SR #7/ASTM #8 crushed limestone, meeting the requirements of ASTM C-33-90. Air entraining admixtures complying with ASTM C-260 were also used in the mix. In order to achieve 8 inches of slump, a

high range water reducer which complies with ASTM C-494 was added. The concrete mix proportions used are presented in Table 2-3.

TABLE 2-3 Mix Proportions

Batch	Material	Quantity *(kg/m^3)*	Concrete Strength *(MPa)* Average
PIERS			
Mix 1: Batch 1 & 2			30.9
	Cement	280	
	Fine aggregate	1136	
	1/2" Coarse Aggr.	848	
	Water	184	
Mix 2: Batch 3 & 4			40.1
	Cement	336	
	Fine aggregate	984	
	1/2" Coarse Aggr.	848	
	Water	201	
END BLOCKS			45.6
	Cement	476	
	Fine aggregate	898	
	1/2" Coarse Aggr.	988	
	Water	149	

Mix 1 was used for the first six specimens. The specimens were cast in two batches of three specimens per batch. Due to project delays, testing did not commence for over 12 months. Hence, Mix II was designed with a higher strength so that all twelve specimens would have approximately the same strength during testing. The target strength was based on cylinder tests of the concrete used in the construction of the first six columns. As shown in Figures 2-5 through 2-8, there is considerable variation in concrete strength even for the same mix.

The end blocks were poured from a different concrete mix and was designed to achieve a strength of 42 MPa at 28 days. The design mix for the end blocks is also shown in Table 2-3. Six cylinders were cast from each batch: three to be used to determine the 28-day strength, and the remaining three to be tested at the same time as the corresponding column test.

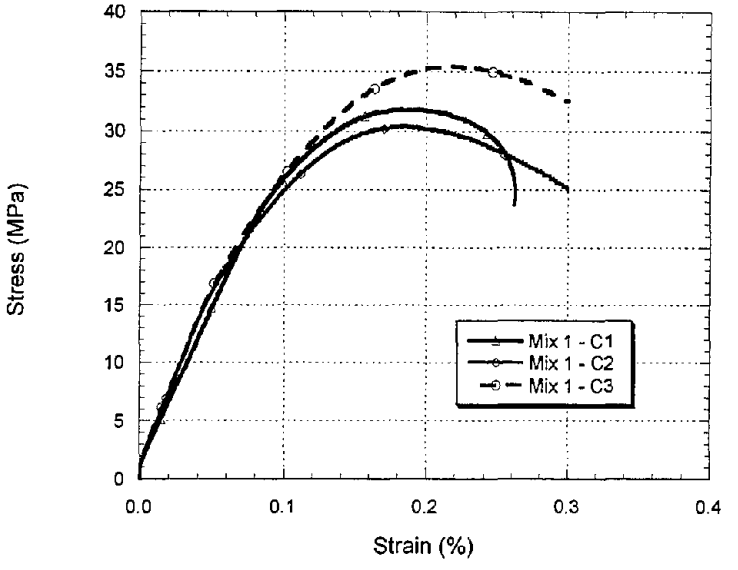

FIGURE 2-5 Stress vs. Strain for Concrete Mix 1 at 28 days

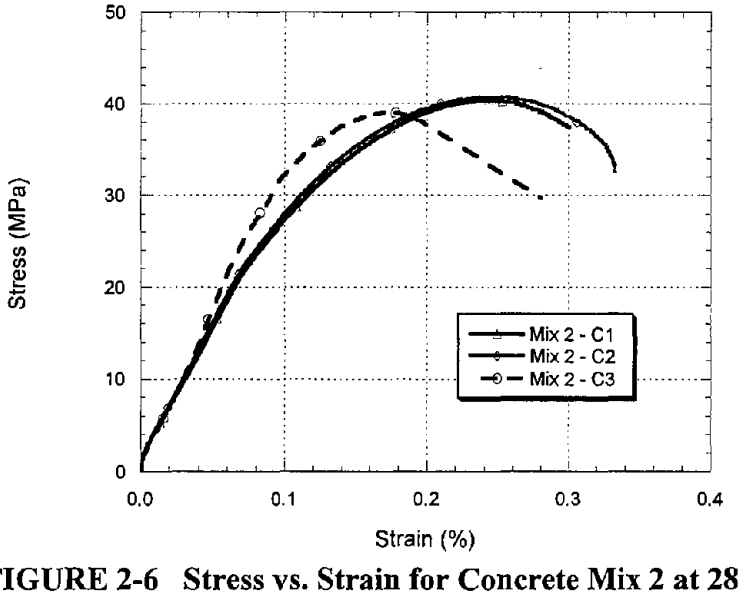

FIGURE 2-6 Stress vs. Strain for Concrete Mix 2 at 28 days

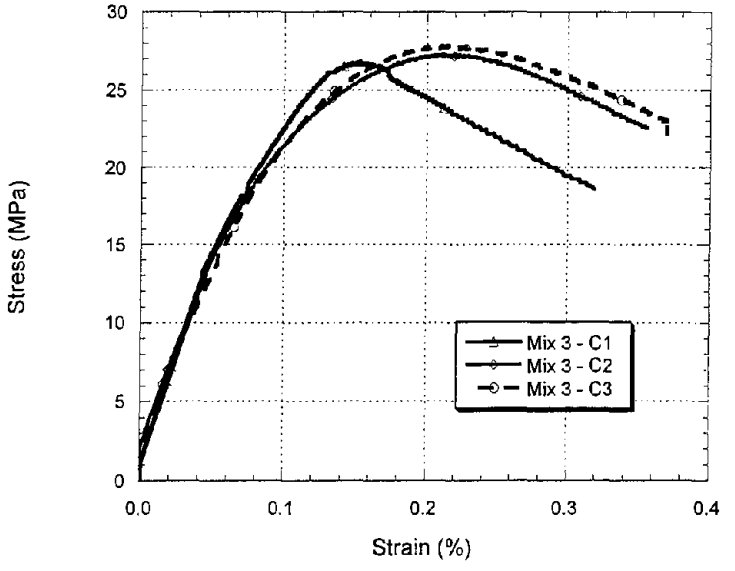

FIGURE 2-7 Stress vs. Strain for Concrete Mix 3 at 28 days

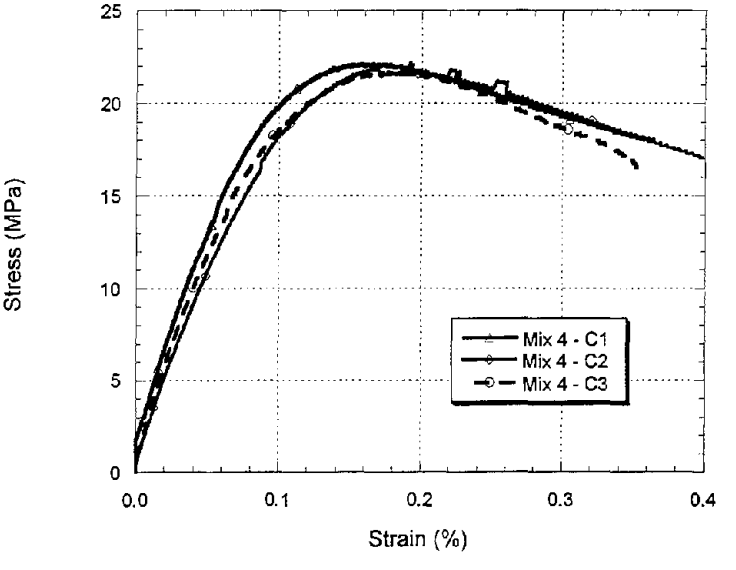

FIGURE 2-8 Stress vs. Strain for Concrete Mix 4 at 28 days

2.2.4 Construction of Columns and Base Blocks

It was decided to construct the pier and foundation for all specimens monolithically, which meant that the base block and the column would be poured together at the same time. Based on this decision, the form had to be designed to accommodate both the column and the foundation block. The forms, which were cut and assembled together on top of a steel frame shoring, were constructed in a manner so that it could be folded together and be reused later. Additionally, forms were tied together to permit six specimens to be cast in a single pour. For ease of construction and pouring, all specimens were cast in an inverted position. The completed formwork is shown in Figure 2-9.

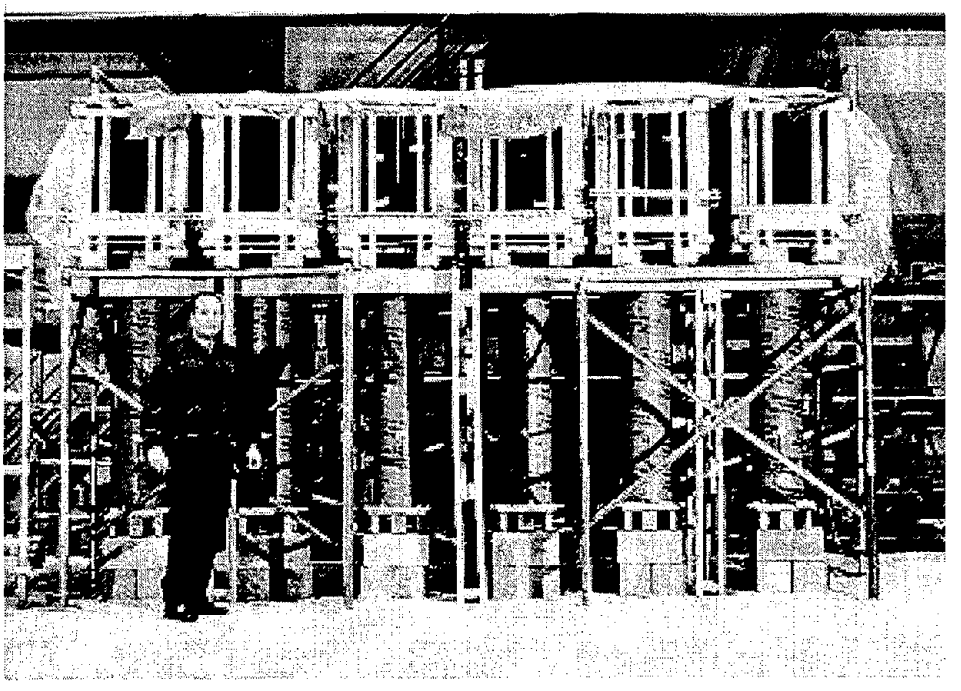

FIGURE 2-9 Formwork for Six Specimens

Steel cages for the columns were assembled first. The steel reinforcement for the footings were then constructed around the column cages. As shown in Figure 2-10, the columns were assembled on three discs which were notched to allow exact spacing and placement of the longitudinal bars. The spirals were tied to the longitudinal # 3 bars at a spacing of 0.75 inch. This spacing was kept constant throughout the column. The side base blocks were designed to allow post tensioning of the foundation block (Figure 2-11). The foundation block is composed of three parts: the mid-section is cast as part of the pier, while the side blocks were cast separately as re-usable blocks which were to be connected to the specimen through post-tensioning.

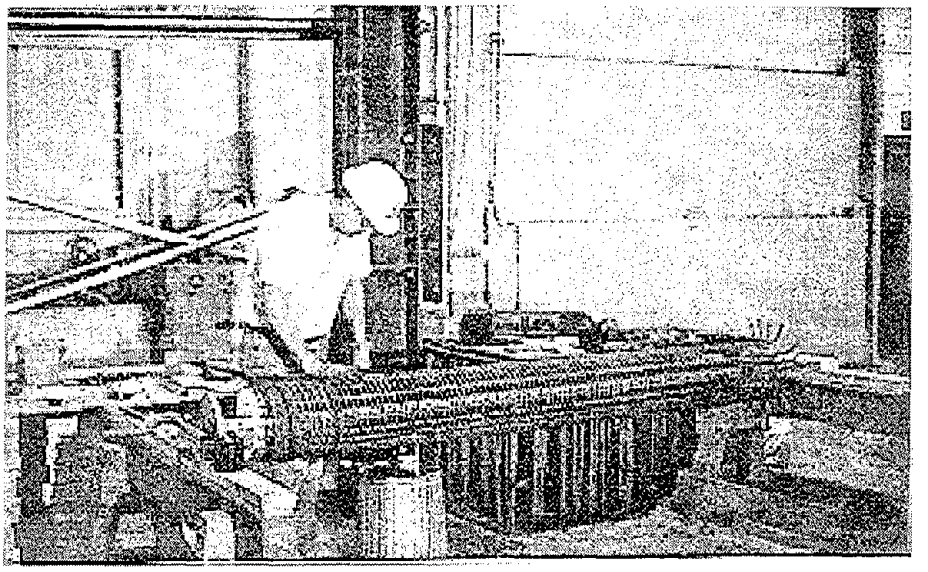

FIGURE 2-10 Cage Assembly for 1:4 Scale Model Piers

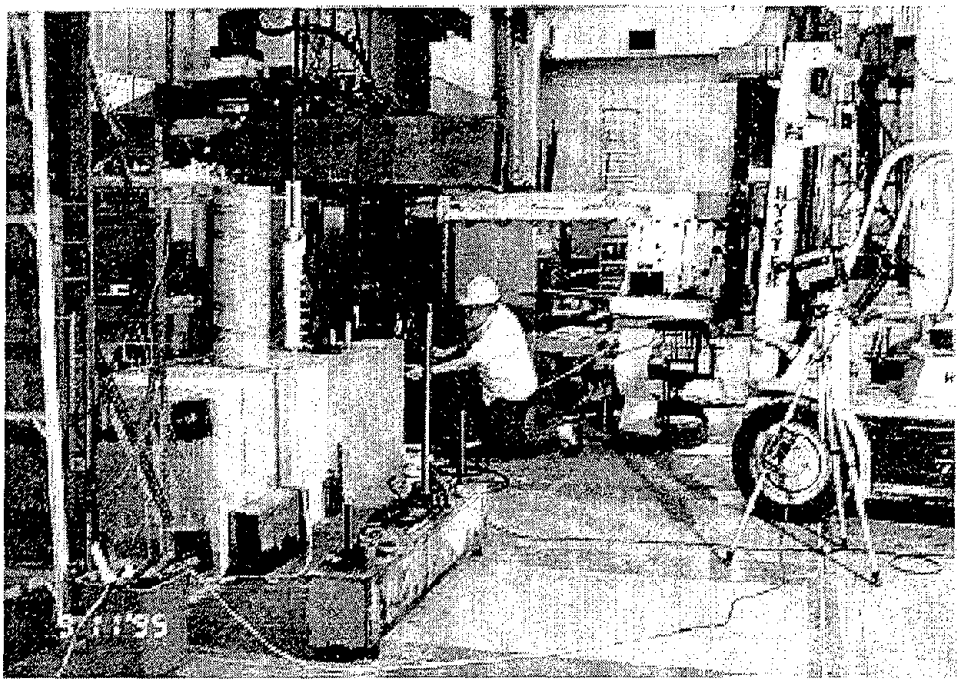

FIGURE 2-11 Post Tensioning of End Blocks to Footing

Four prestressing ducts were installed inside the specimen footings and in corresponding locations in the end blocks such that 1-5/8" high-strength high alloy threadbars could be passed through the two end blocks and footing and post-tensioned before testing each specimen. One such post-tensioning operation for one of the specimens is shown in Figure 2-11. Figure 2-12 shows the reinforcement details for a typical column and its footing.

Dimensional details of the final specimen of the final specimen are presented in Figure 2-13 and 2-14. Two views of the reinforcement used in the column and the base block are shown in Figure 2-13. A number of U-stirrups were used in both directions of the foundation block as shown in the figure to provide the necessary flexural capacity. Essential dimensional details of the finished specimen are displayed in Figure 2-14. The height of the column above the base block is 1525 mm. The center of gravity of the point of application of the load was approximately 1370 mm from the base. Prestressing forces were applied at four locations spaced approximately 610 mm in either direction. The foundation block of the specimen, as poured in-place, measures approximately 460 X 875 mm. However, once the side blocks are attached and post-tensioned, the width of the foundation in the direction of loading is approximately 2.08 meters. The horizontal dashed lines in the figures represent the post-tensioned bars and the vertical dashed lines represent threaded rods used to anchor the base blocks to the floor.

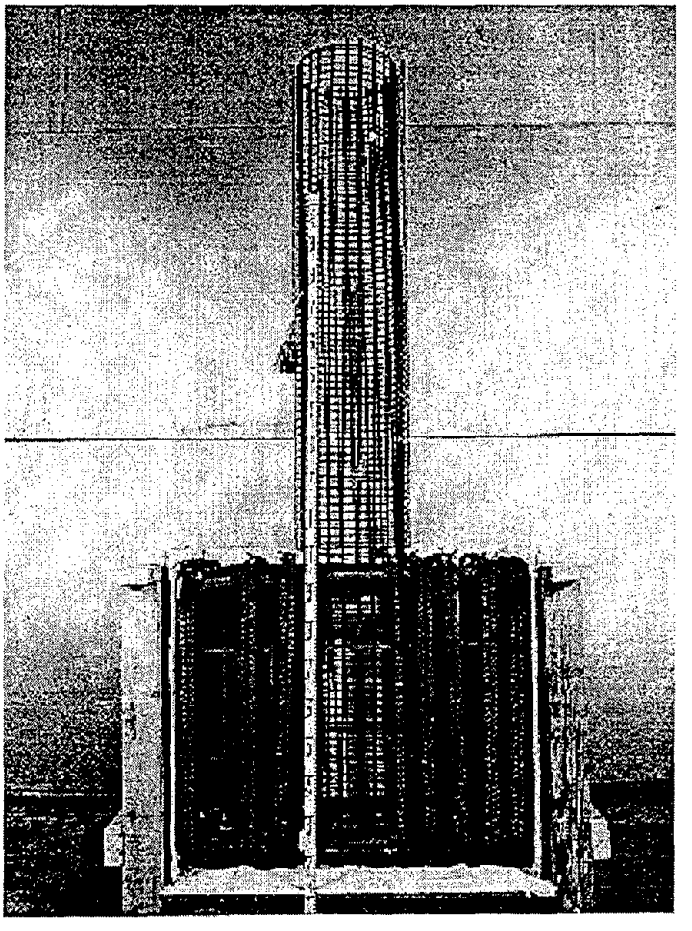

FIGURE 2-12 Cage Assembly for 1:4 Scale Model Column

The post-tensioned end-blocks are shown in Figures 2-15 and 2-16. Three views of a single block are shown in the figures. Two such blocks were used on either side of the column specimen. The blocks were anchored to the strong floor by means of threaded rods, displayed by dashed vertical lines in the both figures. The use of post-tensioned blocks considerably reduced the amount of concrete required to cast each specimen.

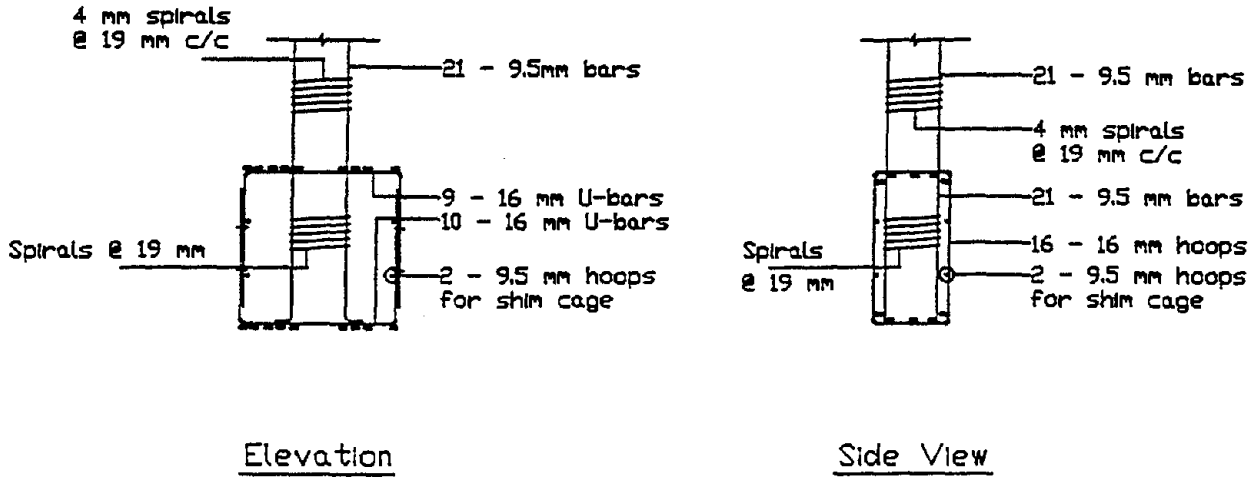

FIGURE 2-13 Reinforcement Arrangement for Specimen with Base Block

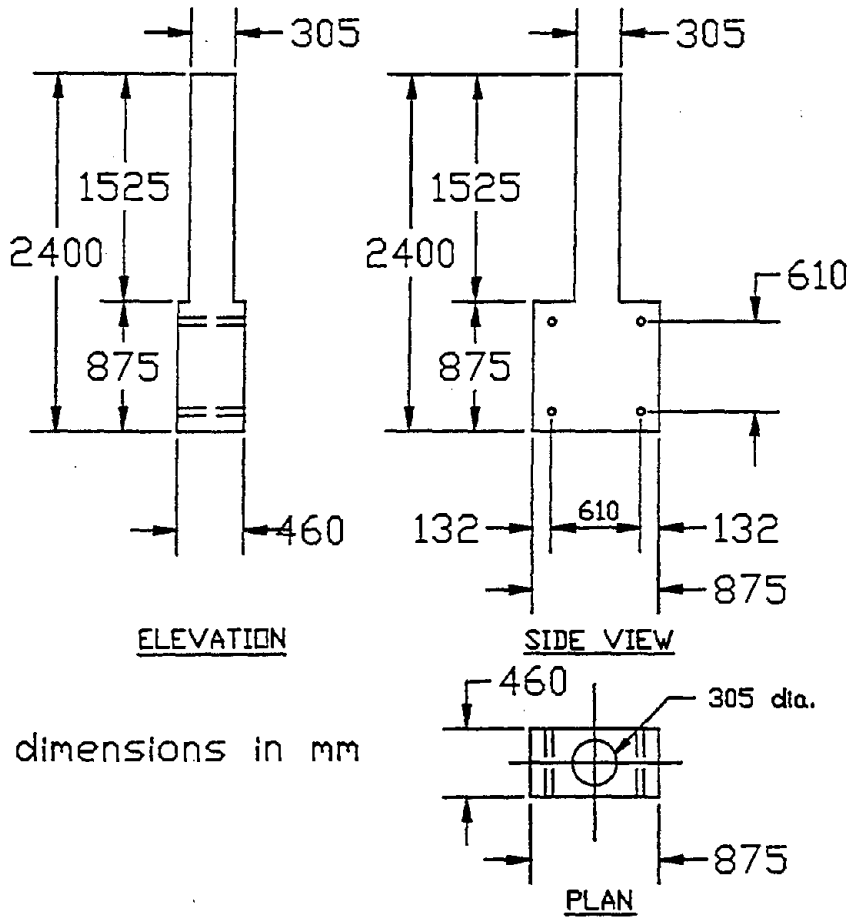

FIGURE 2-14 Configuration and Dimensional Details of Specimen with Base Block

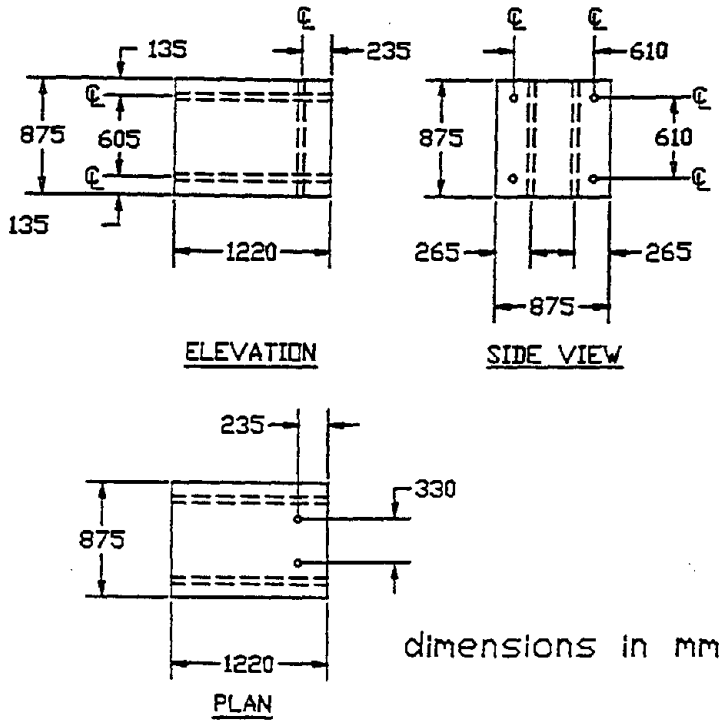

FIGURE 2-15 Dimensional Details of End-Block Attached to Right Side of Specimen

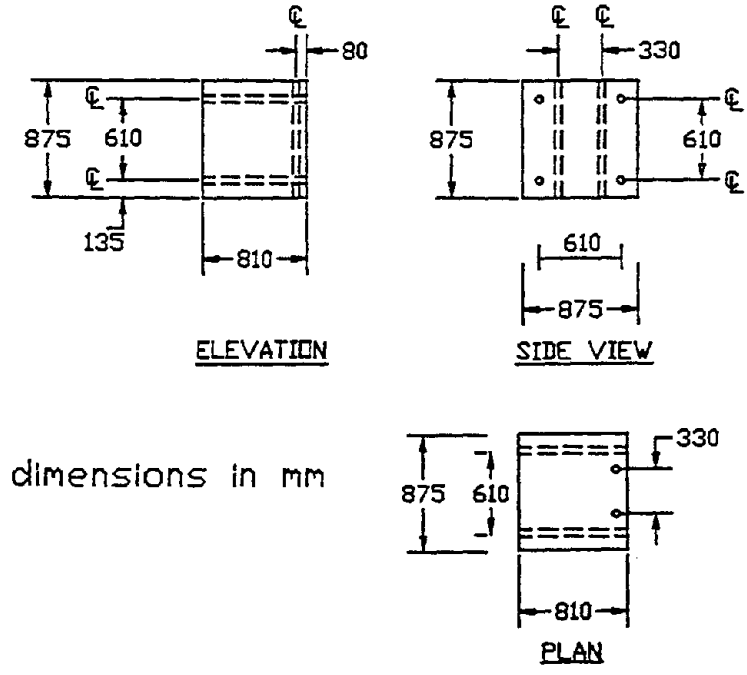

FIGURE 2-16 Dimensional Details of End-Block Attached to Left Side of Specimen

2.2.5 Test Setup

The test setup was assembled from available steel sections. The main consideration, after the prediction of the expected maximum strength of the built specimen, was to minimize the deformation and stresses in the members and connections of the test frame. The calculated maximum deformation of the testing frame was 0.001 inches. A lateral brace was provided to resist a significant portion of the reaction from the horizontal actuator. The second concern was the floor anchoring pattern. The NIST strong floor is a 1.8 m thick heavily reinforced slab with anchorage points for connecting test fixtures located in a grid 1.5 m on center. Each anchorage point consists of two 40 mm bolt holes capable of resisting 900 kN in both the vertical and horizontal direction. The placement of the two end blocks, the tying of the specimen base block to the strong floor, and the layout of the test frame along with the loading actuators were carried out with sufficient precision to allow a ± 6 inches testing displacement in the main lateral degree of freedom.

The final setup with the specimen and the loading mechanisms is shown in Figure 2-17. This figure does not show the support system designed to prevent out-of-plane movement which is described in the paragraph below. A photograph of the as-built test-rig with the specimen in place is shown in Figure 2-18. Details of the specimen instrumentation is discussed in the next sub-section.

To avoid any out-of-plane displacement during testing, two steel beams with smooth surface plates were attached to the testing frame on either side of the specimen parallel to the direction of loading. Four rollers were attached to the column head to permit relatively friction-free movement on the side plates and confine the specimen against any out of plane displacements. Figure 2-19 shows a top view of the support system with the top of the column grip in contact with the side plates.

2.2.6 Instrumentation of Model Columns

The objectives of the testing typically dictate the required instrumentation. The instrumentation program for the experimental testing consisted of measurements of linear (lateral), curvature and rotational response of the specimens. A minimal set of strain gages were also installed to monitor yielding of the longitudinal reinforcing steel bars in the potential plastic hinge zones. The placement of the various measuring instruments is displayed in Figure 2-20. Pertinent details of the instrumentation and measurements are described below.

2.2.6.1 Force-Displacement Measurement

The lateral displacement was applied by a servo controlled 670 kN MTS hydraulic actuator. The hydraulic power supply is a 4.5 cubic meter per second, variable volume pump rated at a pressure of 34 MPa. The actuator stroke was ± 150 mm contolled by a D/A & A/D assembled and programmed data aquisition system. The applied lateral displacement and load were measured from the MTS ram using a calibrated LVDT and load cell, respectively. On the opposite side of the loading actuator a string potentiometer and two LVDT's were mounted against the specimen to measure the lateral displacemnt of the specimen at different elevations.

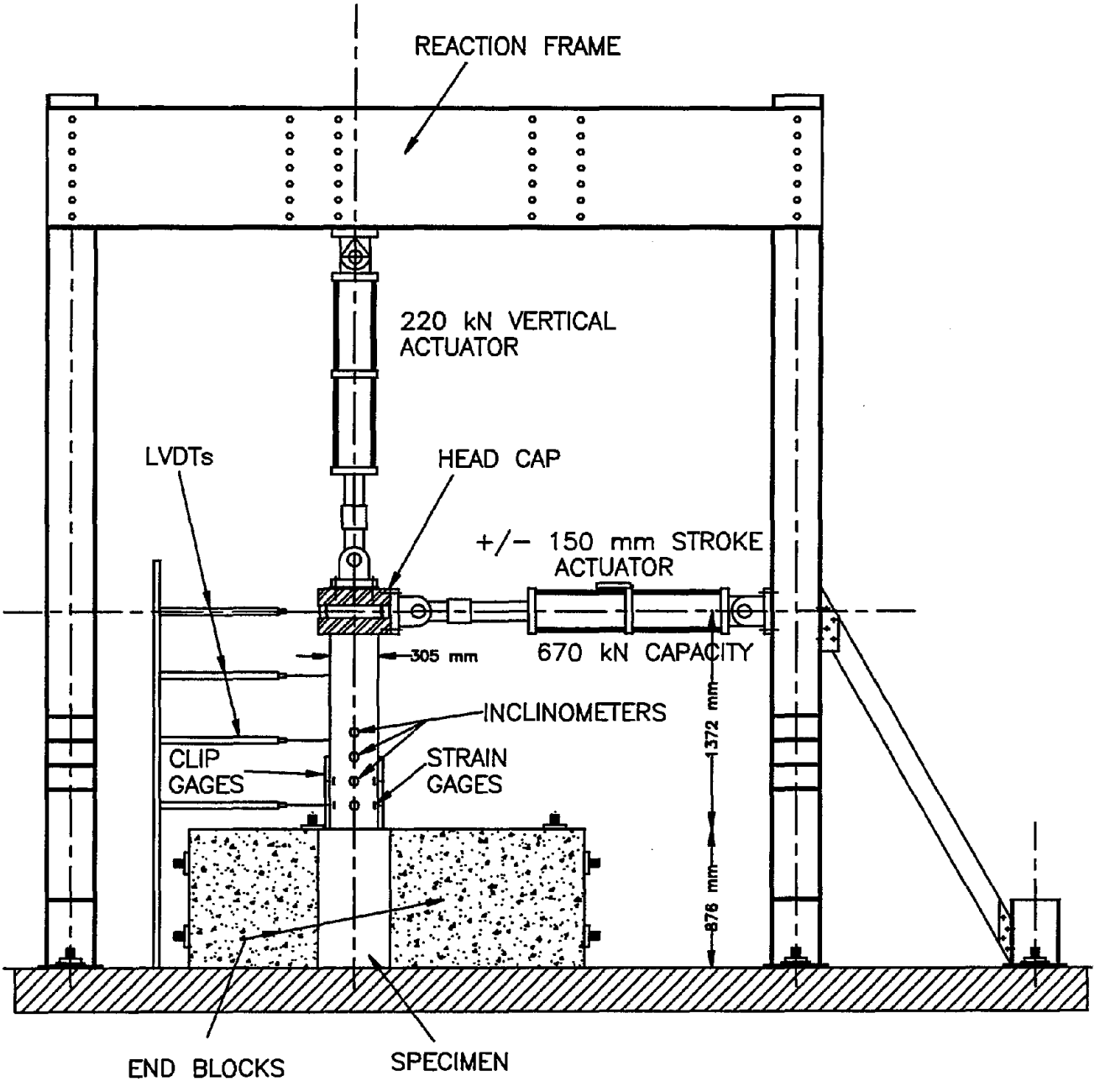

FIGURE 2-17 Details of Load Frame and Test Set-Up

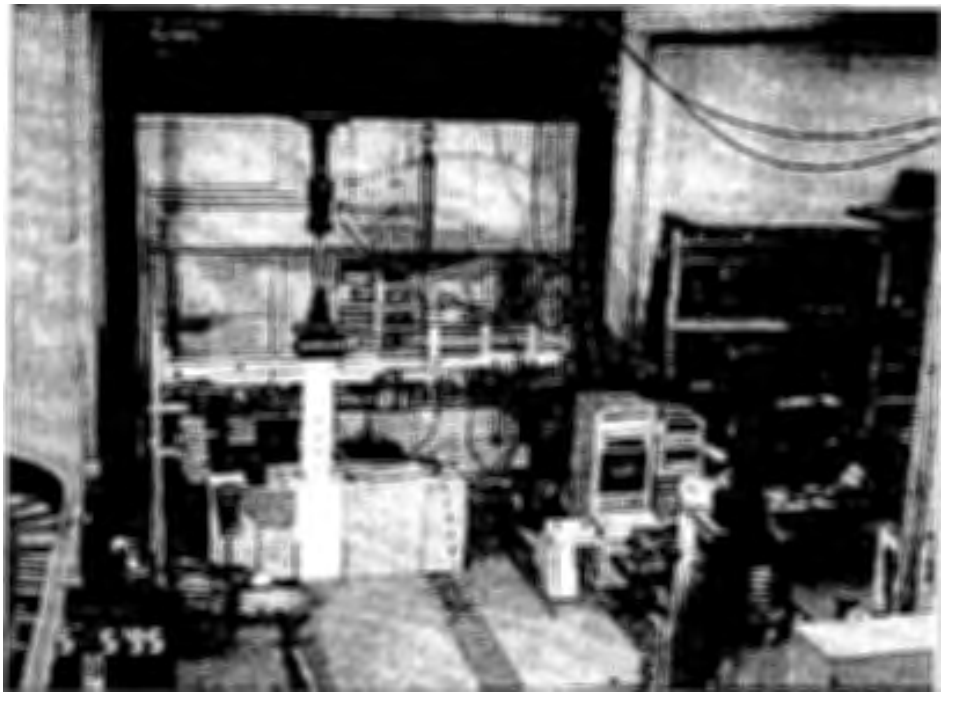

FIGURE 2-18 View of Test Set-Up Prior to Attaching Out-of-Plane Support System

FIGURE 2-19 Overhead View of Out-of-Plane Support System

The string potentiometer was placed at the same level of the actuator center line 1370 mm from the top of the footing. The two LVDTs were placed at 455 mm and 910 mm from the top of the footing. The vertical load was applied using a 220 kN servo-controlled MTS ram. The vertical load was recorded using the calibrated load cell of the vertical actuator. The applied vertical load during testing was approximately constant at $0.1 f_c' A_g$ which is the estimated weight of the bridge deck.

2.2.6.2 Curvature Measurement

The curvature was calculated using six clip gages mounted on opposite sides of the specimen in a plane parallel to the loading direction. The clip gages were designed and manufactured at NIST. These clip gages were used successfully in previous testing of full scale columns at NIST.

The clip gages consist of two strain gages mounted on light gage C-shaped steel sections which in turn are hooked between two points on the specimen equal to the gage length, L (Figure 2-21). The curvature is calculated using the following expression:

$$\Phi = \frac{(\Delta_2 - \Delta_1)}{L\,x} \qquad (2\text{-}11)$$

where

Δ_1 is the contraction or expansion measured by clip gage 1.
Δ_2 is the expansion or contraction measured by the opposite clip gage 2.
L is the gage length
x is the distance between the gage mount points

The above equation is generally valid only under the assumed condition that plane sections remain plane after bending. Curvature measurements beyond yield were also affected by spalling of the cover concrete.

2.2.6.3 Rotational Measurement

Four electric clinometers were mounted on the specimen in the central plane to measure the angle of rotation at the base of the column during testing. The clinometers were connected to a special base, which in turn was connected to threaded rods that were embedded inside the specimens. The clinometers were attached to the specimen at 150, 300, 450 and 600 mm, respectively, from the base of the column (top of the footing). The electric clinometer is composed of a metal gravity sensor with no moving parts such that when rotated, its sensitive axis provides a linear variation in capacitance, which is electronically converted into angular data (Figure 2-22).

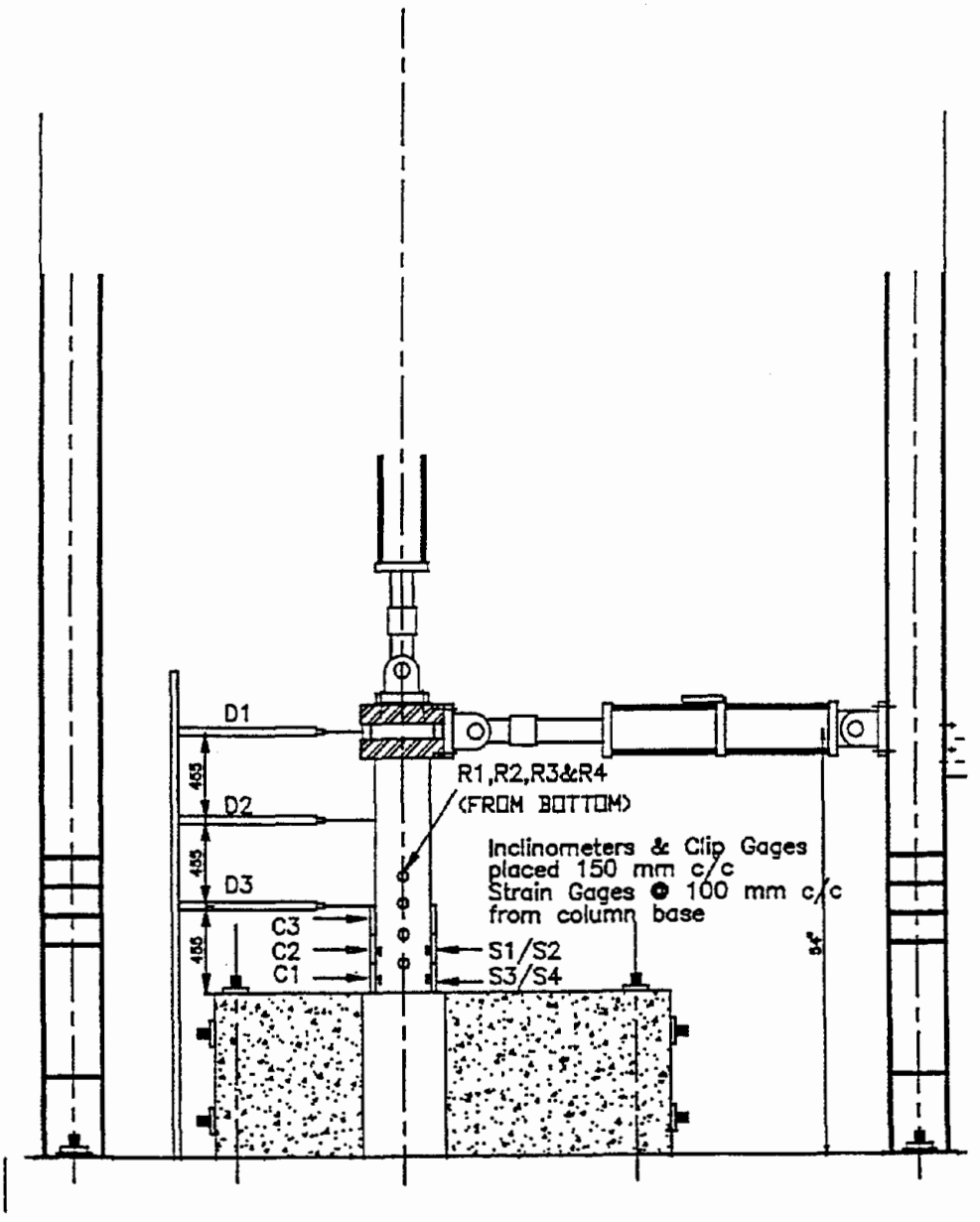

FIGURE 2-20 Test Setup with Instrumentation

FIGURE 2-21 Clip Gage Mounted on Column for Curvature Measurement

FIGURE 2-22 Electric Clinometers Used for Rotational Measurement

2.2.6.4 Strain Measurements

Four strain gages were installed: two each on opposite longitudinal reinforcing bars in the loading plane. The strain gages were installed at 100 mm and 200 mm from the base of the column. These locations were based on estimates of the plastic hinge length of the specimen after yielding, which is typically a distance equal to the depth of the specimen. The strain gages readings were used primarily to check the yielding load of the specimens.

2.2.7 Control and Data Acquisition Systems

The set up of the control system to coordinate (a) the movement of the hydraulic actuator, (b) the data acquisition, and (c) the data display, was a significant and tedious task since there was no existing controller or data acquisition system readily available for use with the experiment. The control system consisted of a microcomputer with the usual peripherals, an analog-to-digital (A/D) converter, a digital-to-analog (D/A) converter, two servo-controllers (one for the vertical actuator applying the gravity load on the specimen and the other for the lateral actuator applying the simulated earthquake displacements) and computer software (see Figure 2-23). Both controllers had a full scale range of ± 10 volts.

The data acquisition system had 2 - 32 channel real time A/D cards and 1- 2 channel D/A card. The control system was programmed to send a voltage signal through the D/A card to impose the required displacement history on the lateral hydraulic actuator. A special-purpose computer program was written using system software to achieve various levels of control during testing. This included the ability to stop the testing at any intermediate loading point and altering the displacement history, if necessary. A predefined set of A/D channels which were to be sampled during testing were established. Sampling rates were based on available disk storage space since the system was capable of sampling 50,000 samples per second. The data acquisition program also had the capability of reading different output channels at previously specified frequencies.

2.2.8 Ultrasonic Measurement

Nondestructive test methods are gaining popularity these days as a means of assessing structural integrity. It was, therefore, decided to validate the feasibility of using ultrasonic measurements in assessing the damaged state of selected specimens after testing. Consequently, ultrasonic readings were taken across the column in a plane parallel to the loading at different heights. The readings for the travel time of an ultrasonic wave across the concrete specimen were taken once before testing and later after the test was completed. Figure 2-23 shows the locations at which the readings were taken. It was very difficult to take measurements during testing since the noise and vibrations of the hydraulic pump interfered with ultrasonic measurements. The objective of including this measurement in the experimental program was to seek a correlation between damage and the wave travel time through concrete.

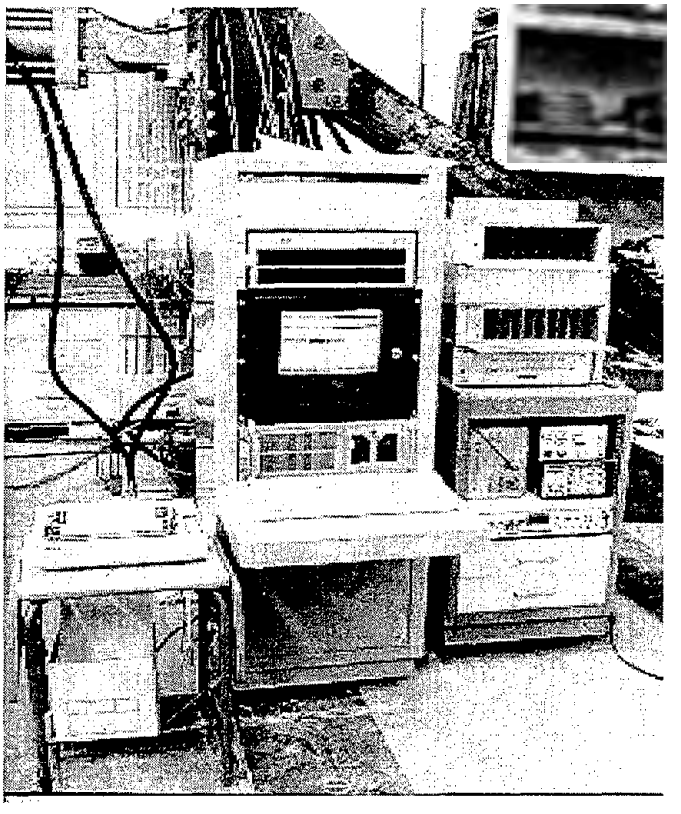

FIGURE 2-23 Control and Data Acquisition System

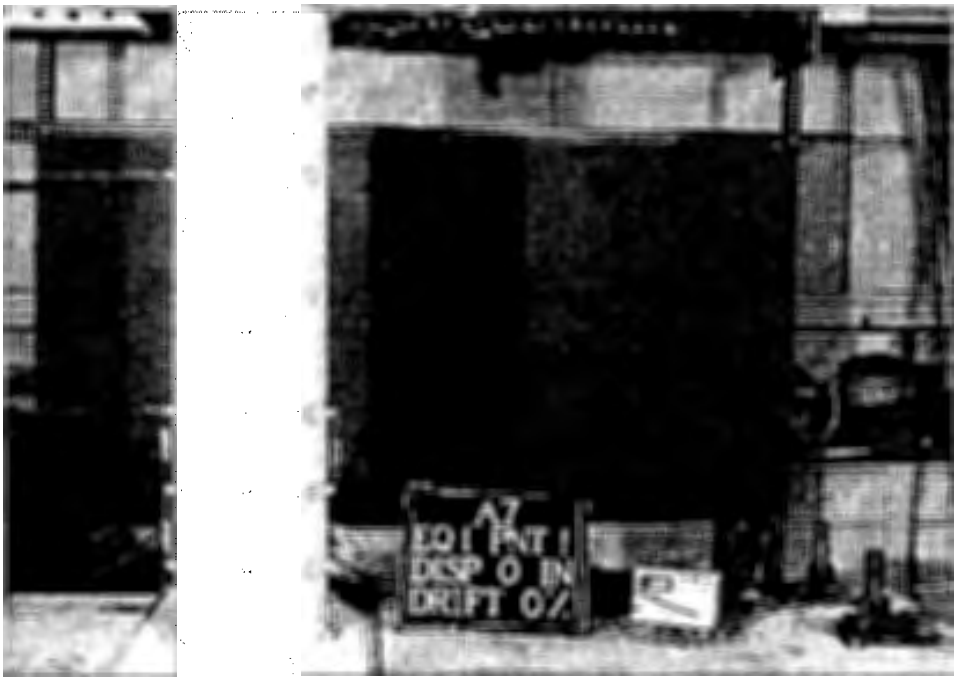

FIGURE 2-24 Ultrasonic Readings Across Concrete Column

3.0 ANALYTICAL MODELING AND DEVELOPMENT OF LOAD HISTORIES

The development of load histories for the random phase of testing was accomplished through the use of a nonlinear computer program, IDARC (Kunnath et al., 1992). Prior to using random loads, however, it was essential to conduct certain benchmark tests to permit rational interpretation of the results. The benchmark testing was composed of monotonic, standard cyclic and constant-amplitude fatigue loading. Following this, a series of random displacement histories were analytically simulated for the second phase of testing. Details of the bridge column model used in analytical simulations, calibration of the hysteresis loops and selection of the load histories are outlined in this section.

3.1 Analytical Model of Bridge Column

The prediction of the inelastic response of the model column was an important subset of the overall task of developing the experimental test program. The imposed random displacement histories were meant to reflect realistic displacements under actual earthquake loads. Hence, every effort was made to use reliable element and material models to predict displacements under inelastic load reversals. The conceptual framework in which the nonlinear time-history evaluations are carried out represent a macromodel approach, summarized in Kunnath and Reinhorn (1995). It consists of characterizing member behavior through assumed flexibility distributions and monitoring stiffness at selected critical location through prescribed hysteresis models. The success of this approach has been documented in Kunnath et al. (1992). The two main elements of the macromodel are: (1) a flexibility-based member model; and (2) a versatile hysteresis model that characterized moment-curvature behavior at the plastic hinge zone. Details of each are briefly described.

3.1.1 Component Modeling

Seismic moments induced in the bridge column have a linear variation along the length as shown in Figure 3-1. When the tensile stress due to these moments exceed the tensile strength of concrete, cracks form along the length of the member which in turn influences the moment of inertia of the section. The member curvature parameter is inversely proportional to the moment of inertia of the section and varies along the member length. The bridge column was modeled as a single component with distributed flexibility. A linear variation of flexibility is used up to the yield point of the member, after which a constant plastic region is assumed, as shown in Figure 3-1. Flexibility coefficients for this assumed distribution is calculated from the principles of virtual work:

$$f_{ij} = \int_0^L m_i(x) m_j(x) / EI(x) d(x) \qquad (3\text{-}1)$$

where: $m_i(x)$ = moment distribution for unit moment at end i

$m_j(x)$ = moment distribution for unit moment at end j

$EI(x)$ = flexural rigidity

The flexural rigidity, EI, at the ends of the member is monitored throughout the analysis. The moment rotation relationship for such an element can be derived by integrating the M/EI diagram across the length of the member, as follows:

$$\begin{Bmatrix} \Delta\theta_A \\ \Delta\theta_B \end{Bmatrix} = \begin{bmatrix} f_{11} & f_{12} \\ f_{21} & f_{22} \end{bmatrix} \begin{Bmatrix} \Delta M_A \\ \Delta M_B \end{Bmatrix} \tag{3-2}$$

where $\Delta\theta$ and ΔM are the incremental rotations and moments at the ends A and B of the member, respectively. The flexibility coefficients of the above matrix are:

$$f_{11} = (3+3\alpha-3\alpha^2+\alpha^3-\beta-\beta^2-\beta^3+2\alpha\beta-\alpha^2\beta+\alpha\beta^2)/(12EI_a) + (1-3\alpha+3\alpha^2-\alpha^3+\beta+\beta^2+\beta^3-2\alpha\beta+\alpha^2\beta-\alpha\beta^2)/(12EI_b) \tag{3-3}$$

$$f_{12} = -f_{21} = (1+\alpha+\alpha^2-\alpha^3-\beta-\beta^2+\beta^3+\alpha^2\beta-\alpha\beta^2)/(12EI_a) + (1-\alpha-\alpha^2+\alpha^3+\beta+\beta^2-\beta^3+\alpha\beta^2-\alpha^2\beta)/(12EI_b) \tag{3-4}$$

$$f_{22} = (1+\alpha+\alpha^2+\alpha^3-3\beta+3\beta^2-\beta^3-2\alpha\beta-\alpha^2\beta+\alpha\beta^2)/(12EI_a) + (3-\alpha-\alpha^2-\alpha^3+3\beta-3\beta^2+\beta^3+2\alpha\beta+\alpha^2\beta-\alpha\beta^2)/(12EI_b) \tag{3-5}$$

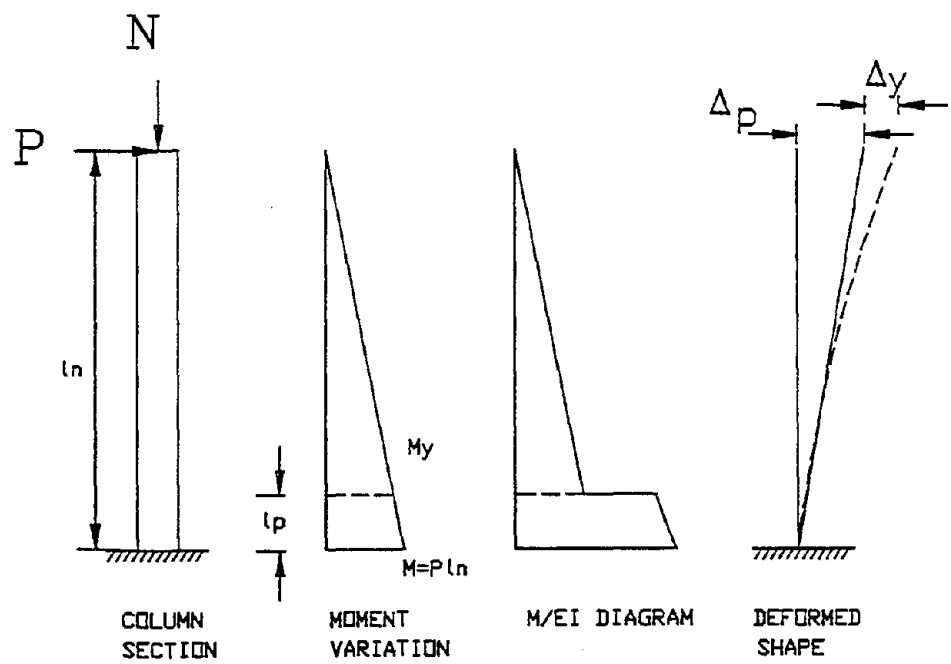

FIGURE 3-1 Inelastic Component Model of Bridge Pier

where α and β are the plastic hinge length ratios (expressed as a function of the member length) at the ends *A* and *B*, respectively. The term *(EI)* represents the instantaneous flexural rigidity at the ends of the member. In the case of a single bridge column, the top end always remains elastic and no plastic hinge length needs to be computed which greatly simplifies the above expressions (i.e. $\beta = 0$).

Since lateral loads, such as those caused by an earthquake, produce only linear variations in the moment diagram, the above formulation works effectively and efficiently. If additional moments, such as those caused by distributed member loads, are significant, then the nonlinear distribution of moments may not be sufficiently overcome by the lateral loads leading to potential errors in the assumed flexibility distribution. In such cases, it is necessary to sub-divide the element into smaller sections so that the assumed linear distribution is valid.

The element stiffness matrix is derived from the equilibrium of forces at the ends of the member and can be expressed in the following form:

$$[K_B] = [R_B][k_s][R_B]^T \tag{3-6}$$

where $[k_s]$ is sub-local stiffness matrix determined through inversion of the flexibility matrix given in Equation (3-2), and:

$$[R_B] = \begin{bmatrix} -1/L & -1/L \\ 1 & 0 \\ 1/L & 1/L \\ 0 & 1 \end{bmatrix} \tag{3-7}$$

in which L is the length of the member. In general, the system of equations to be solved, at any stage of analysis, is in the form:

$$[K]\{u\} = \{F\} \tag{3-8}$$

where $[K]$ is the global stiffness matrix, u is the vector of unknown nodal displacement and $[F]$ is the vector of applied equivalent forces on the system. Since the stiffness matrix is symmetric, only one half band width is stored by offsetting the main diagonal. The global stiffness matrix is obtained by assembling the element matrices and updated only in the event of a stiffness change.

The rest of the analysis procedure is similar to matrix frame analysis wherein the assembled structure stiffness matrix is inverted through numerical techniques and solved for each step of the imposed force or displacement. Dynamic time-history analysis is carried out by explicit direct integration using Newmark's unconditionally stable "beta" method (Newmark, 1959). The moments at the base of the column are updated at every step. The corresponding stiffness is established from a predetermined hysteresis model with user-specified control parameters for stiffness and strength degradation. The hysteresis model was calibrated using observed results from Specimens A-1 and A-2 as described in the next section.

Equilibrium errors resulting from changes in state (stiffness transition) are treated by means of a single-step force correction. This consists in computing unbalanced forces at the end of any given analysis step and applying them as corrective forces in the next step. Such a procedure was first used in DRAIN-2D (Kanaan and Powell, 1973) since the compuational effort required for a fully iterative nonlinear analysis is substantial.

3.1.2 Hysteretic Modeling

The primary difference between a macromodel approach as used in the present study and standard finite element representation is that, in the present scheme, no constitutive equations are used. Instead, the inelastic behavior is described using force-deformation rules which attempt to capture overall member behavior. In theory, it is possible to construct force-deformation curves using constitutive models. However, constitutive laws hold true only for a microscopic point in the material. For an inhomogeneous material such as reinforced concrete, it will take a very fine discretization of the cross-section to represent the material behavior in terms of local concrete-steel interaction. Such an approach, however, is tedious and computationally intensive.

The force-deformation model used in the IDARC program is based on three primary control parameters and an additional secondary parameter to establish the rules under which inelastic loading reversals take place. Details of the model and the control parameters can be found in Kunnath and Reinhorn (1995). A variety of hysteretic loop shapes can be achieved by a proper combination of a monotonic trilinear force-deformation envelope and the control parameters which characterize stiffness degradation, strength deterioration and pinching or slip behavior.

While automatic identification of hysteretic parameters is possible (Kunnath et al., 1996), the control parameters were identified directly from one of the experiments conducted in this study. A graphical evaluation of the hysteresis loops generated from the cyclic testing of Specimen A2 yielded control parameters as shown in Table 3-1. The simulated loops using these parameters are shown in Figure 3-2. Except for some minor discrepancy in the shape of the loops just above and below the zero-force axis, the overall behavior matches the experiment with adequate accuracy. The identified control parameters listed in Table 3-1 were used in all IDARC analyses for the generation of the random displacement histories.

TABLE 3-1 Identified Control Parameters

Parameter	Meaning	Value
α	Degree of Stiffness degradation	8.0
β_d	Strength degradation based on ductility	0.025
βe	Strength degradation based on ductility	0.0
γ	Pinching coefficient	1.0

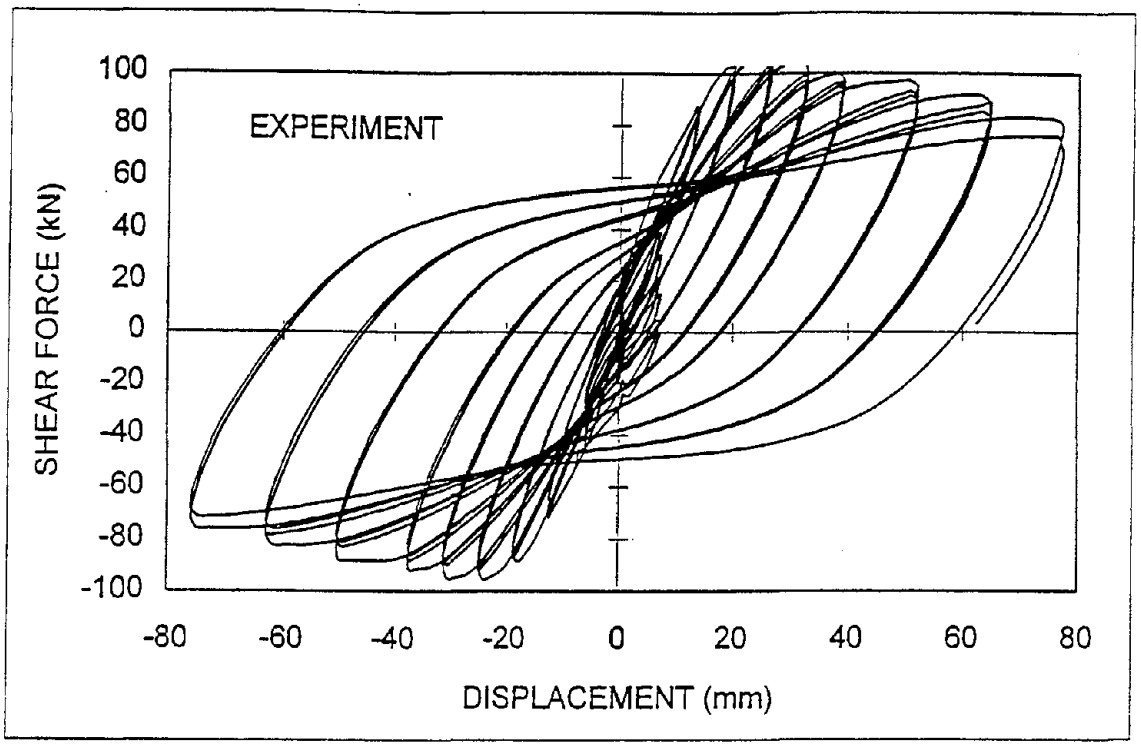

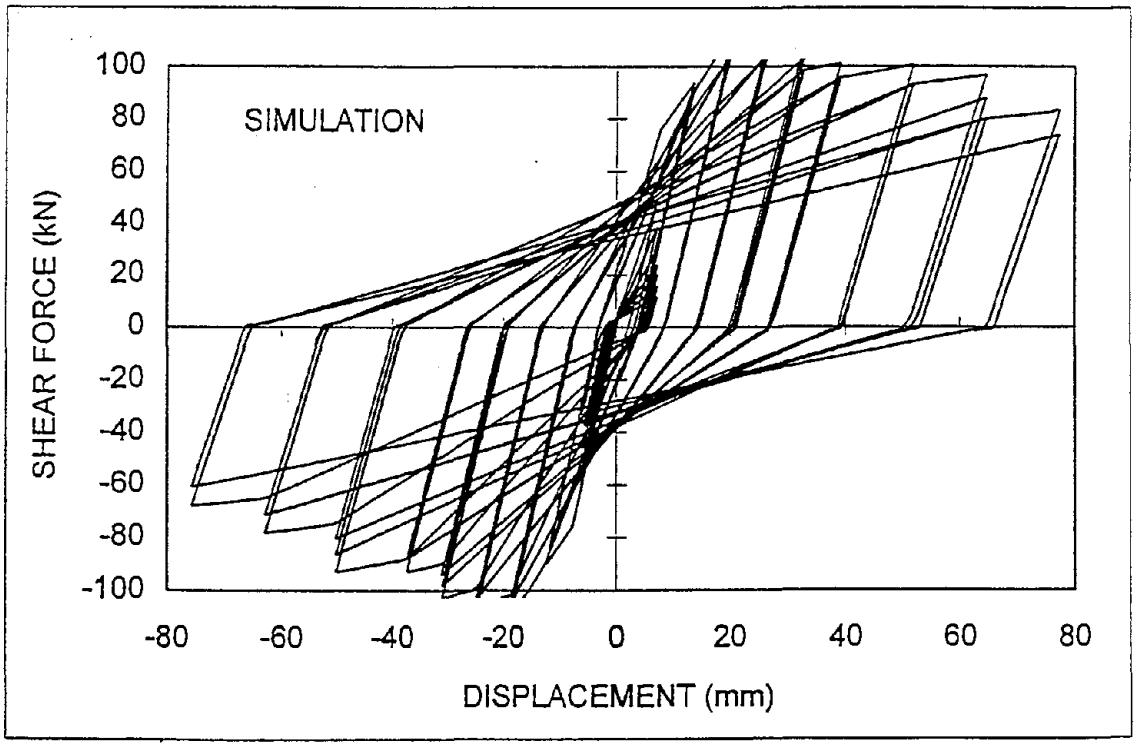

FIGURE 3-2 Calibration of Hysteresis Model

3.2 Prototype vs. Model Calibration

The IDARC runs to generate the random displacement histories were carried out on the model specimen. If similitude requirements had been satisfied in every aspect, it would have been equally logical to carry out the analyses on the prototype and scale the resulting displacements by a factor of 4.0. However, given the probability that some discrepancy in material property similitude may exist, it was decided to carry out the simulations using the model geometry and material properties. A verification analysis was conducted, however, to check model response against corresponding prototype response for a specified ground motion. The prototype bridge column was subjected to the 1940 El Centro earthquake, assuming fixed based conditions, while the model column was subjected to the same record using a compressed time scale of $1/\sqrt{S}$, where S is the scale factor as required by similitude. The same intensity (PGA) earthquake was used in both runs since the time compression applied to the model structure accounts for the scale factor. Results are presented in Figure 3-3 in which the model response is clearly seen to be scaled down by the model scaling factor, viz., 4.0.

3.3 Selection of Displacement Histories

One of the main objectives of this research is the investigation of load paths and its effect on structural damage. However, to enable meaningful comparison of random load response with tests conducted by others using standard cycles with increasing ductility, it was considered important to carry out a few benchmark tests. A few critical parameters were deemed important in establishing such benchmarks. First, it was decided that a lateral load test under monotonically increasing load until failure was essential, since numerous models of damage use the monotonic envelope as a base line for comparing strength deterioration, normalizing energy dissipation and/or peak deformation, etc. Secondly, a standard cyclic test using traditional displacement amplitudes was also considered vital so that differences in load paths could be characterized. Finally, it was considered crucial to conduct a few low-cycle fatigue tests under constant amplitudes to establish a basis for validating cumulative damage theories. The fatigue tests were conducted at slow strain rates since typical earthquakes do not impose high strain rates on bridge structures. These tests were needed to provide fundamental data on the fatigue life of typical flexural columns. The remaining specimens were all tested under random load histories. The complete set of experiments showing the type of imposed displacement is presented in Figure 3-4.

3.3.1 Benchmark Testing

Benchmark tests are typically carried out to calibrate future testing. In this project, the benchmark tests were a critical part of the overall objective of identifying damage parameters. It was necessary to relate dissipated energy, number of inelastic cycles, and peak/average inelastic cyclic strains, to be observed in the random tests, to corresponding estimates in standard testing.

The first specimen designated A1 was tested under a monotonically increasing lateral load until failure. Failure would be defined, in this case, as a significant drop in load carrying capacity and incipient P-delta collapse. The significance of the monotonic envelope cannot be underestimated

since it forms the basis for defining a host of control parameters in many existing damage models. Specimen A2 would be subjected to a normal cyclic load with three full cycles at increasing ductility up to failure. Following each set of cycles at a given ductility, a small cycle at approximately $\delta = 0.5\Delta y$ would be imposed to measure change in system stiffness.

Specimens A3 - A6 were tested under constant amplitude reversed cyclic displacements. Specimen A3 was tested under a constant cyclic displacement amplitude of approximately $\delta = \pm 2\Delta y$. Specimen A4 was cycled under a constant displacement of $\delta = \pm 3\Delta y$. Similarly, Specimens A5 and A6 were cycled at amplitudes of $\delta = \pm 4\Delta y$ and $\delta = \pm 5\Delta y$ until failure. Failure was defined as either the loss of confinement following hoop fracture or significant loss of vertical load carrying capacity following longitudinal bar failure.

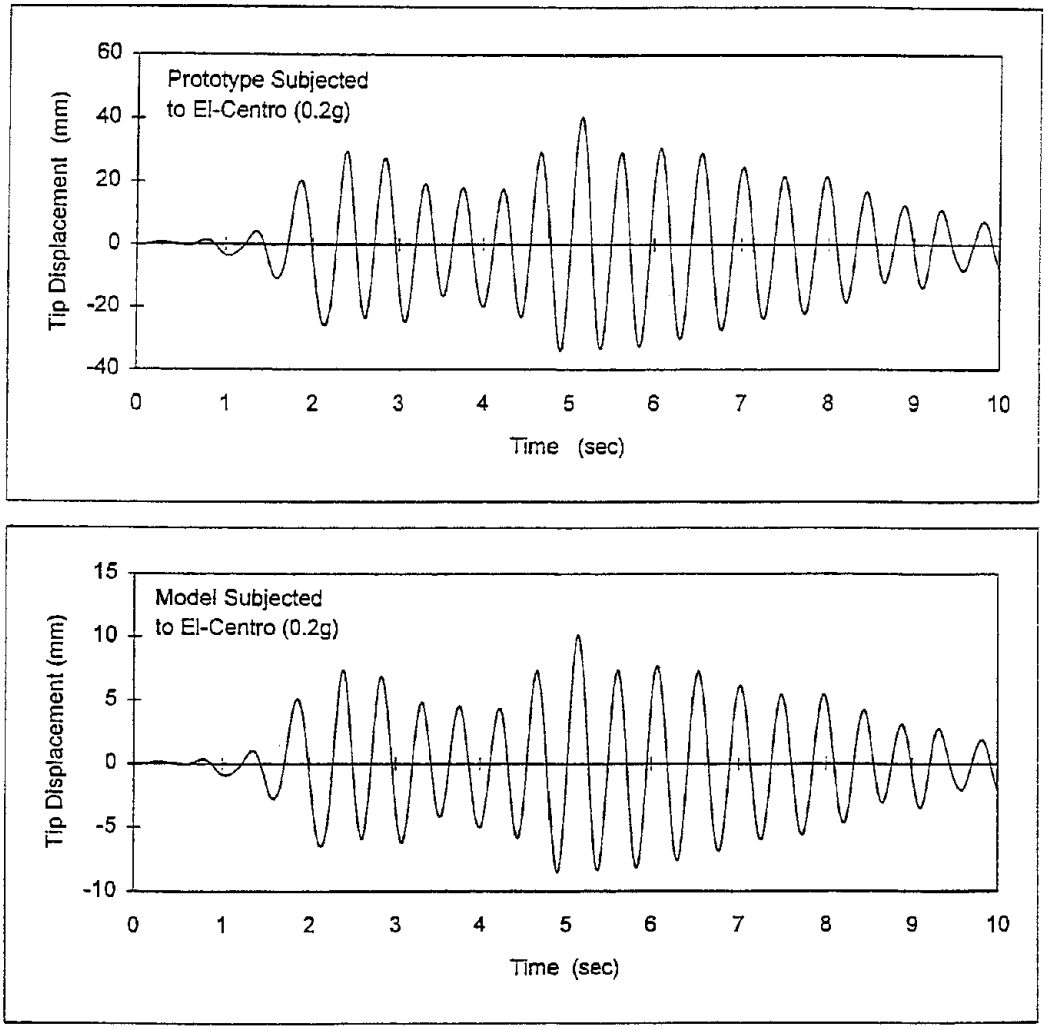

FIGURE 3-3 Comparison of Prototype vs. Model Response

SPECIM. NO.	LOAD ROUTINE	X–DIR. LOAD HISTORY	Y–DIR. LOAD HISTORY	PLAN VIEW OF LOAD
A1	MONOTONIC PUSHOVER TEST	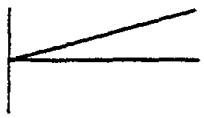		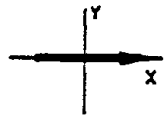
A2	STANDARD DISPLAC. PATTERN			
A3	2 Δy TO FAILURE	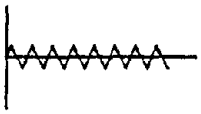		
A4	3 Δy TO FAILURE	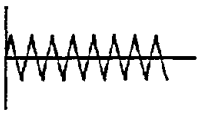	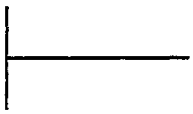	
A5	4 Δy TO FAILURE	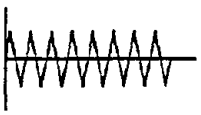	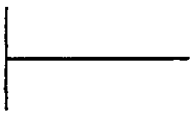	
A6	5 Δy TO FAILURE	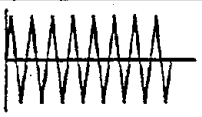	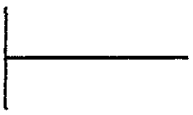	
A7	RANDOM EARTHQUAKE LOADING			
A8	RANDOM EARTHQUAKE LOADING			
A9	RANDOM EARTHQUAKE LOADING			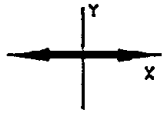
A10	RANDOM EARTHQUAKE LOADING		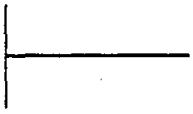	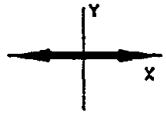
A11	RANDOM EARTHQUAKE LOADING			
A12	RANDOM EARTHQUAKE LOADING			

FIGURE 3-4 Summary of Displacement Histories Used in Testing

3.3.3 Random Loading

Specimens A7 through A12 were designated for random load testing. The choice of the displacement history to be imposed was crucial. Hence, a great deal of time was spent trying to develop a rational basis for identifying and specifying random displacement histories. Two issues were considered more important than others since it addressed directly the research objectives of this study of cumulative damage:

1. The imposed earthquakes had to represent realistic scenarios. And the damage resulting from the sequence of selected events had to induce adequate damage so that calibration of damage through each of the limit states, from undamaged (elastic) to collapse would be viable.
2. The effect of load path on the ultimate response, both in terms of physical damage limit states and in terms of measurable damage parameters, had to be identified.

Item 1 addressed above is shown conceptually in Figure 3-5. The question as to how one might ensure a certain level of damage after each event posed innumerable challenges. This is where the benchmark tests would contribute significantly. It was decided to utilize the damage data from the first series of six tests to calibrate a fundamental fatigue-based damage theory. This would then be utilized to plan the final series of six tests based on a predicted damage scenario. Section 5 of this report will discuss the development of the random histories in greater detail.

The effect of load path would be considered by taking a given random displacement history and altering the sequence of the displacement cycles. Hence, the number and amplitude of the displacement cycles would remain unchanged - the only variable being introduced is the sequence in which the displacements are applied. Again, since the selection of the random histories is dependent on the outcome of the testing of the first six specimens, further discussion on the imposed random histories is deferred until Section 5.

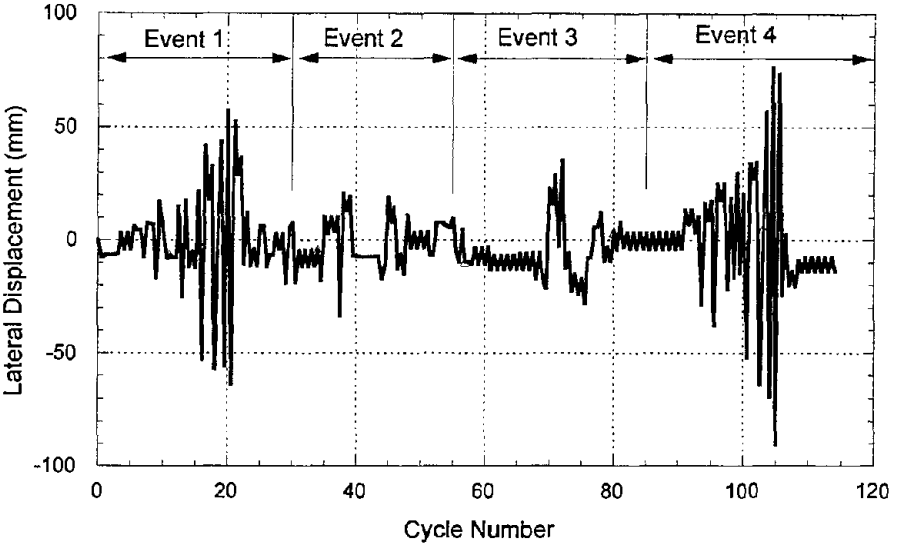

EVENT	DESCRIPTION	PURPOSE
1	Major event	Significant Damage from potential earthquake
2	Minor event	Aftershocks
3	Minor event	Intermediate non-critical events at site
4	Maximum credible event at site	Failure of structure

FIGURE 3-5 Typical Loading Scenario for Random Amplitude Testing

4.0 CUMULATIVE DAMAGE TESTING I: PUSHOVER, BENCHMARK AND FATIGUE LOADING

The mechanics of cumulative seismic damage in reinforced concrete has never been fully understood. It is the premise of this research that one of the primary reasons contributing to this lack of knowledge is the fact that past experimental testing has not focused on the mechanics of damage progression. The present research is directed particularly at the phenomenon of progressive or cumulative damage, hence the only variable introduced in the testing program is the applied load history. Since seismic loads induce fairly random cycles of reversed displacements on structural members, it was important to consider random load paths representative of typical inelastic dynamic response motions. However, in order to evaluate and calibrate the resulting response under random loads, it was necessary to establish certain benchmark parameters. The following tests were conducted to ensure a reasonable database of parameters against which to compare the random load testing:

1) Monotonic loading: The purpose of this test is to develop the backbone or skeleton force-deformation envelope for the specimen. Some damage models use strength and deformation quantities derived from a monotonic test to normalize and/or formulate the damage expressions.
2) Standard cyclic test: This was considered essential since all past laboratory testing has been based on this approach. This would provide a convenient benchmark against which to compare random amplitude testing.
3) Quasi-fatigue testing: Another critical aspect that deserved consideration was the quantification of low-cycle fatigue failure. In an attempt to calibrate a fatigue-based damage model for flexural members, a series of tests was carried out in which the specimen was subjected to reversed cyclic loading at constant amplitudes until failure.

The benchmark tests and the constant amplitude tests were expected to provide a basis for estimating damage so that the displacement histories required for the random testing could be developed. The testing program was consequently divided into two phases: the first phase would comprise benchmark and low-cycle fatigue tests, and the next phase would consider response under random loads. The importance of the first phase of testing will become evident at the end of this section. It was essential to develop an understanding of the mechanics of low-cycle fatigue so that the displacement histories in the second phase could be planned in a way to achieve desired damage states.

Details of the first phase of testing are described in this section. Records kept during testing included information such as crack widths, spalling, exposed reinforcement, etc. that permit calibration of damage to visual observations in post-earthquake reconnaissance. Failure was typically defined by either the rupture of confining spirals or fracture of longitudinal reinforcing bars. Other essential details such as necking of hoops or buckling of longitudinal bars were also monitored. In addition to the overall force-deformation response, recorded information such as cracking, yielding and failure load and displacements will be summarized for each specimen.

The recorded force-deformation data was converted to shear vs. displacement response taking into consideration the additional moments induced due to P-delta effects. Figure 4-1 shows a schematic diagram of the test set-up and the relevant quantities required to derive the necessary forces and moments. With reference to Figure 4-1, the shear force *(V)* in the column is given by:

$$V = P + \frac{Nx}{H} \tag{4-1}$$

where: $x = (L + H)\sin\theta$ (4-2)

and $\theta = \tan^{-1}\left(\frac{\Delta}{L}\right)$ (4-3)

Table 4-1 summarizes the material properties of the specimens used in Phase I testing. Concrete was ordered from a local concrete mixing plant with the stipulation that the strength of the mix be 4000 psi. However, as is evident from the results presented in Table 4-1, despite efforts to keep material properties the same for all tests, the concrete strengths obtained from the two batches were different.

Table 4-1 Average Material Characteristics for Phase I Testing

SPECIMENS A1 - A3	
Concrete Strength:	29 MPa
Steel Yield Strength:	448 MPa
Spiral Yield Strength:	434 MPa
SPECIMENS A4 - A6	
Concrete Strength:	35.5 MPa
Steel Yield Strength:	448 MPa
Spiral Yield Strength:	434 MPa

4.1 Specimen A1: Monotonic Loading

Specimen A1 was tested under a monotonically increasing lateral loading until failure. Compression tests on control cylinders tested on the day of testing indicated an average compressive strength of approximately 29 MPa. The loading was applied in displacement increments of 2.5 mm at the beginning of testing up to yielding of the specimen. As the system stiffness dropped significantly, the displacement increments were increased to 5 mm.

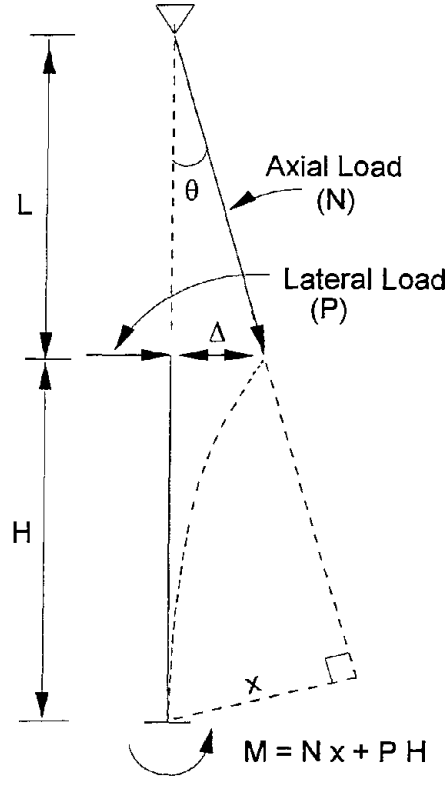

FIGURE 4-1 Computation of Column Moments and Shear Including P-Delta

Very fine hair-line cracks occurred at 2.5 mm lateral displacement. The cracks became significant as the lateral displacement increased to 5.0 mm. Spalling of the concrete cover was initially observed at approximately 33 mm lateral displacement. The spalling became significant when the displacement exceeded 48 mm (3.5% drift). The crack width at this stage was on the order of 1-2 mm. At this stage of spalling, the spiral reinforcement was clearly exposed. The maximum lateral load reached 66 kN before additional displacement caused a gradual softening of the column stiffness. Two longitudinal bars showed signs of buckling. No necking of hoops took place, which indicated that neither the spirals nor the longitudinal bars were likely to rupture under monotonic loading. The specimen lateral load capacity started dropping significantly after a lateral drift of 4.0%.

The definition of failure in a monotonic test is difficult to establish. While it is conceivable that large lateral displacements (without reversals) can strain the longitudinal bars to fracture, such a level of displacement was not possible in the present test given the limitation of stroke capacity of the hydraulic actuator. Additionally, at these large displacements, P-delta effects are significant and the resulting secondary moments can result in collapse of the structure. Again, the test setup, consisting of hydraulic actuators mounted directly onto the specimen, will prevent this from happening. Given these circumstances, it was decided to stop testing after the load

capacity decreased significantly, on the order of 20-30%. In the present test, this was achieved at about 11 % drift.

The results of testing on specimen A1 produced the backbone force-deformation envelope that was used in the initial analytical simulations. A trilinear representation, in which cracking and yielding are distinguished, was considered in the analytical study. The analytical model was eventually modified at the end of phase I testing to reflect average response values rather than the results of specimen A1 alone. Table 4-2 provides a summary of test observations. Figure 4-2 and 4-3 show the state of the specimen at the onset of yielding and at the end of the test, respectively. Figure 4-4 presents the resulting force-displacement response.

TABLE 4-2 Summary of Test Observations for Specimen A1

LOADING TYPE: Monotonic pushover to failure.

LOAD AND DISPLACEMENT VALUES OF INTEREST:

Axial Load :	200 kN
Maximum Lateral Load:	66 kN
Cracking Load:	17.8 kN
Cracking Displacement:	5 mm
Yield Load:	64 kN
Yield displacement:	19 mm
Maximum Lateral Displacement:	152 mm
Failure Mode:	Potential P-delta failure

DAMAGE OBSERVATIONS:

Displacement (Drift%)	Notes
2.5 - 5 mm (0.2-0.4%)	First Cracking
19 mm (1.4%)	Yielding
33 mm (2.4%)	Spalling
60 mm (4.4%)	Significant Spalling
150 mm (11%)	Failure

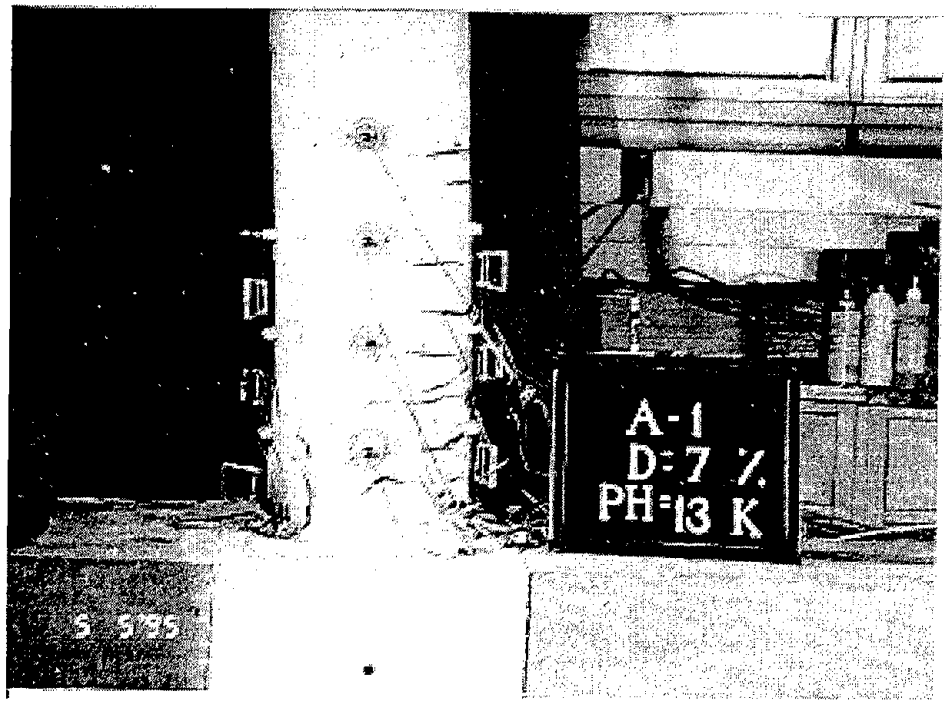

FIGURE 4-2 Damage to Specimen A1 at 3.5% Drift

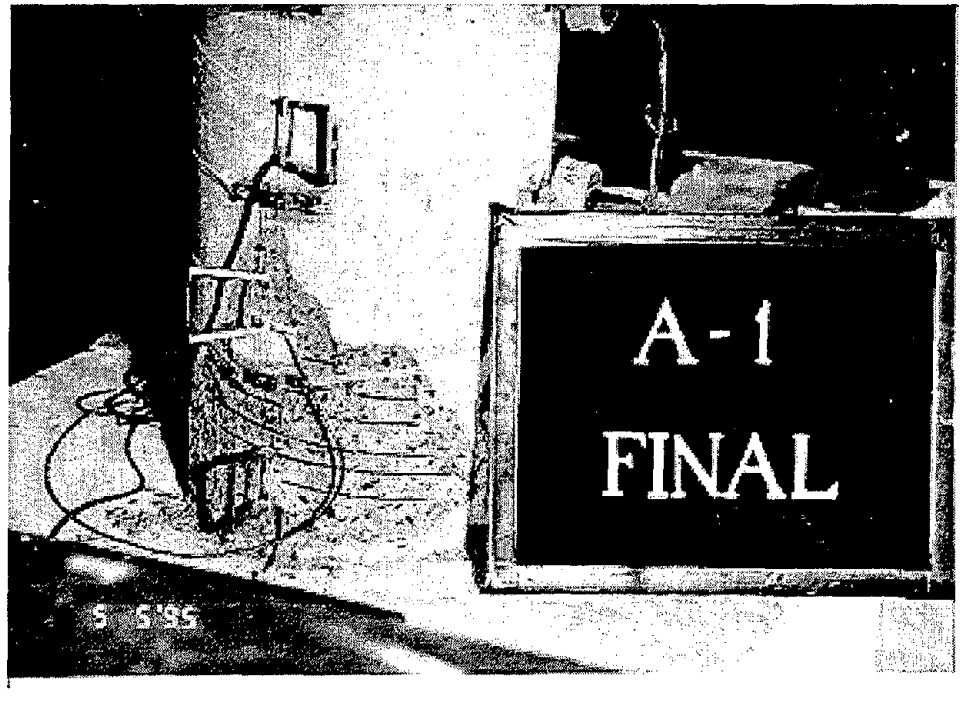

FIGURE 4-3 Specimen A1 at End of Test

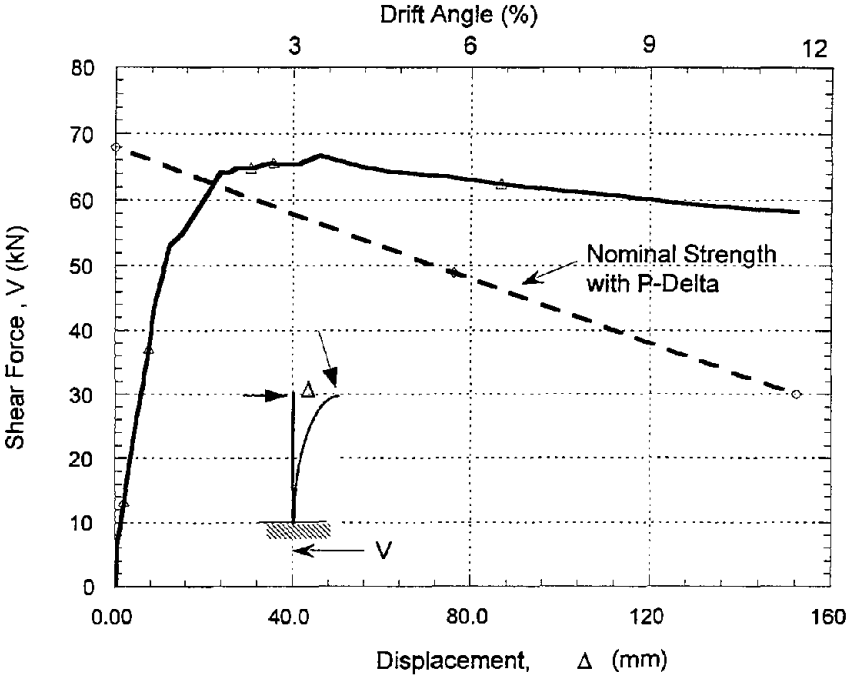

FIGURE 4-4 Base Shear vs. Displacement Response of Column A1

4.2 Specimen A2: Standard Cyclic Loading

The established procedure for seismic testing of specimens consists of applying a series of reversed displacement cycles with increasing amplitude. Typically, either two or three full cycles are applied at a specified amplitude (either as a function of drift or ductility) with a smaller cycle in between each increase in amplitude to characterize the system stiffness at the end of each amplitude. A major focus of this research is to investigate if this is an appropriate load history to characterize random loads resulting from earthquake response. In order to study the differences in response using random loads, it was necessary to test one of the specimens using the established standard cyclic procedure.

Specimen A2 was subjected to three cycles at each displacement amplitude as a function of lateral drift. Displacement amplitudes used in the testing consisted of three cycles each at 1.0%, 1.5%, 2.0%, 2.5% 3.0%, 4.0%, 5.0% and 6.0% drift until failure. The smaller amplitude between each increase in amplitude was 0.5% drift.

The specimen strength was estimated at 29 MPa based on cylinder tests. Cracking and yielding occurred in the very first cycle. Hair-line cracks began to appear at a lateral displacement in the range of 2.5 – 5.0 mm. Crack widths were measured at 0.2 mm at the end of the second cycle. Crack widths grew to almost 0.7 mm by the end of cycle 10, to 1.0 mm at cycle 13, and up to 1.5 mm at cycle 19 when the drift was about 3%.

Yielding was estimated at 20 mm lateral displacement when the lateral load reached approximately 65 kN. Spalling of the concrete cover was observed at cycle 15 at a drift of approximately 3%. Significant cracking propagated up to 225 mm beyond the base of the column at this stage. Minor bar buckling and significant spalling was evident by the end of cycle 22.

At cycle 30, the specimen was considered to have failed when spiral rupture occurred. Testing was stopped after the cycle was completed. The spiral fracture was clearly noticeable in the load-displacement plot. The plastic hinge length was estimated as 180 mm though cracking propagated beyond this region. The peak lateral displacement at failure was recorded at 76.2 mm which corresponds to a drift of about 5.5%.

Figure 4-5 shows the damaged state of the specimen near the plastic hinge zone close to the failure load. Figure 4-6 shows a closer view of the specimen at the end of testing in which the ruptured spiral is visible. Figure 4-7 shows the imposed displacement history on specimen A2 while Figure 4-8 presents the resulting force-displacement response. Table 4-3 is a summary of observed data on the results of the testing.

TABLE 4-3 Summary of Test Observations for Specimen A2

LOADING TYPE: Standard Cyclic Loading

LOADING AND DISPLACEMENT VALUES OF INTEREST:

Axial Load :	200 kN
Maximum Lateral Load:	75 kN
Cracking Load:	18 kN
Cracking Displacement:	5 mm
Yield Load:	65 kN
Yield displacement:	19 mm
Maximum Lateral Displacement:	76 mm
Failure Mode:	Rupture of Spiral on the Right Side

DAMAGE OBSERVATIONS:

Cycle No.(Drift)	Notes
1 (1%)	First Cracking, Yielding
15 (3%)	Spalling of cover
22 (5%)	Significant Spalling, some buckling of longitudinal bars
30 (6%)	Failure of Spiral on Right Side

FIGURE 4-5 Damaged State of Specimen A2 at Cycle No. 30

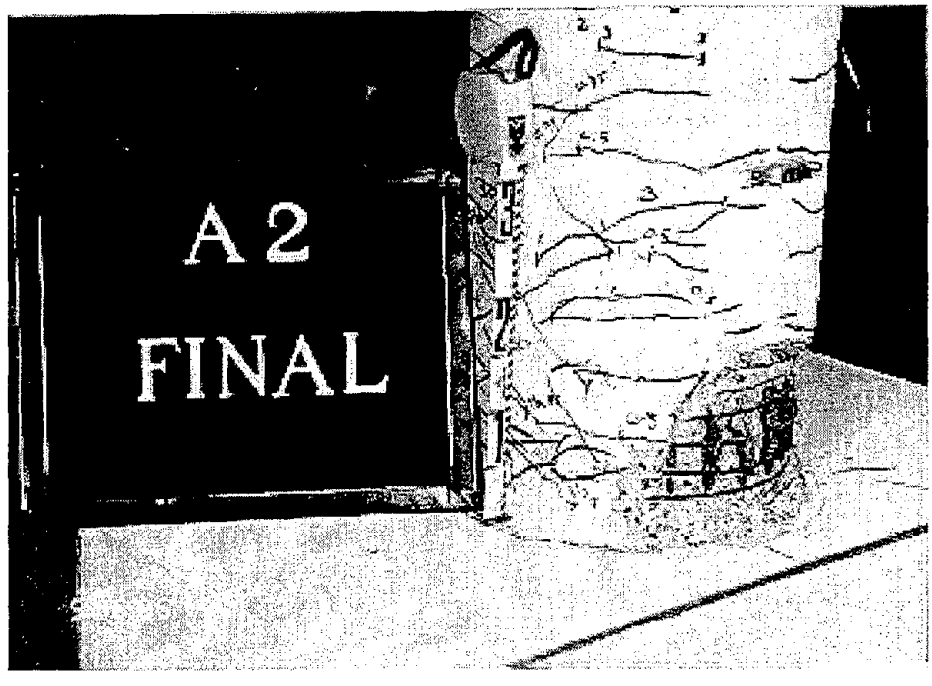

FIGURE 4-6 Final Damaged State of Specimen A2

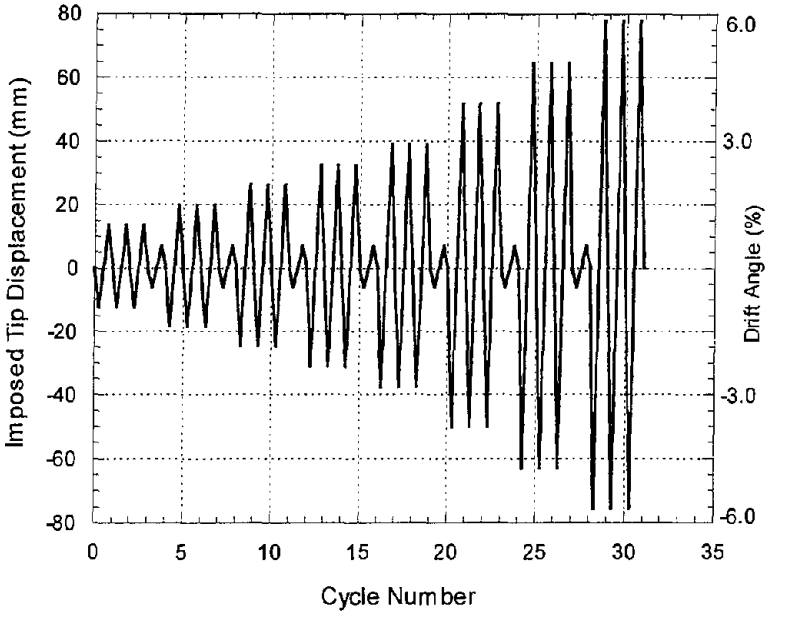

FIGURE 4-7 Displacement History Applied to Column A2

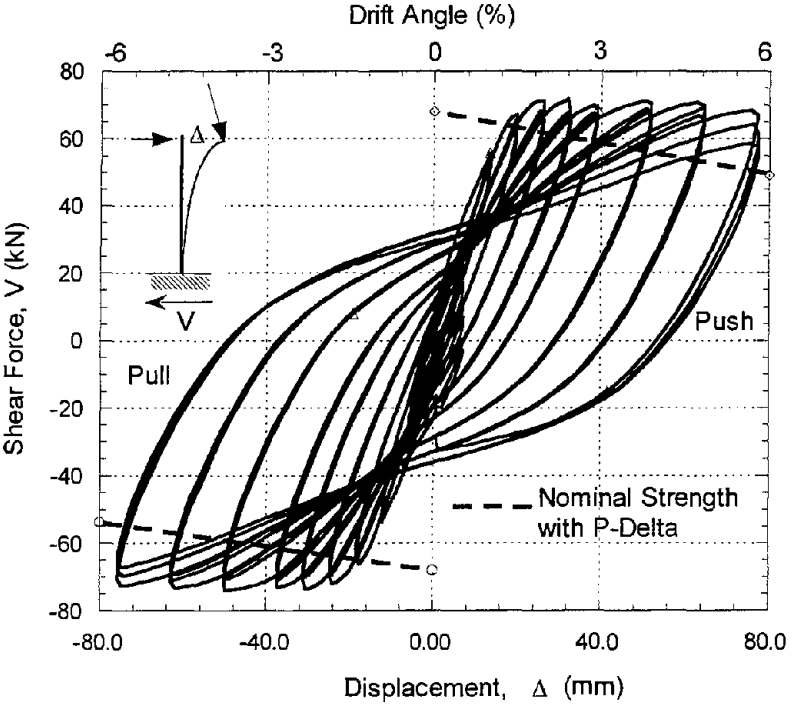

FIGURE 4-8 Shear vs. Displacement Response of Column A2

4.3 Quasi-Fatigue Loading

There is very limited information on the low-cycle fatigue behavior of reinforced concrete. The only work to be found in the literature is a series of low-cycle fatigue tests conducted by Mander and Cheng (1995) to validate the applicability of using specially detailed fuse bars in the plastic hinge regions in bridge columns. Any effort to develop a cumulative damage model for concrete will be incomplete without an understanding of this important phenomena. Therefore, a significant portion of the present test program (specimens A3, A4, A5 and A6) was directed towards studying the failure of bridge columns under constant amplitude loading.

4.3.1 Specimen A3: Constant Amplitude Cycles at 2% Lateral Drift

Specimen A3 was subjected to constant amplitude cycles at a displacement amplitude corresponding to 2% lateral drift. Initial cracking occurred in the very first cycle at this drift limit and minor spalling was observed on the compression side. The specimen was then reversed in the opposite direction to the same amplitude. Cracking on the opposite side was observed accompanied by similar spalling. The maximum crack width at this point was 0.5 mm. On returning to the zero position, the cracks closed and were almost invisible. At cycle 3, the crack widths increased to 0.8 mm. The column was cycled an additional 19 times with no additional cracking or spalling. Maximum crack widths on either side were about 0.8 - 1.0 mm. The test was stopped at the end of the day after 40 cycles of reversed cyclic loading at a constant displacement amplitude of about 26 mm without any further deterioration to the specimen.

The following day, testing of column A3 continued at cycle 41. The rate of loading was increased to the full capacity of the actuator. At cycle 95 some loose concrete was picked off. Loading of specimen A3 continued until cycle 150 without any further damage. Later, it was analytically estimated that this specimen would have sustained over 300 cycles. Since one of the objectives of the test program was to study different damage models, it was decided that the cyclic loading could be discontinued and a monotonic load applied until failure. This would provide information on reserve capacity that is crucial to many damage modeling theories. The specimen sustained a final drift amplitude of over 10% after experiencing 150 cycles at 2% drift which suggests that the damage from the initial 150 cycles was negligible.

Table 4-4 provides a detailed summary of observed results related to testing of specimen A3. Figure 4-9 shows the state of specimen A3 after 100 cycles of loading. The column condition at the end of testing is shown in Figure 4-10. Figure 4-11 shows the imposed displacement history on specimen A3 and Figure 4-12 displays the resulting lateral force vs. displacement response history.

TABLE 4-4 Summary of Test Observations for Specimen A3

LOADING TYPE: Constant Amplitude Cycles at 2% Lateral Drift

LOADING AND DISPLACEMENT:

Axial Load :	200 kN
Maximum Lateral Load:	72 kN
Yield Load:	65 kN
Yield displacement:	19 mm
Lateral Load at failure:	64 kN
Failure Mode:	No failure due to cyclic load, Final failure under monotonic load at 10.5% drift

DAMAGE OBSERVATIONS

Cycle No.	Notes
1	First Cracking
1	Minor Spalling
0.5	Yielding
100	Significant Spalling
150.5	Failure (due to monotonic load)

FIGURE 4-9 Specimen A3 at Cycle 100

FIGURE 4-10 Specimen A3 at End of Fatigue Testing

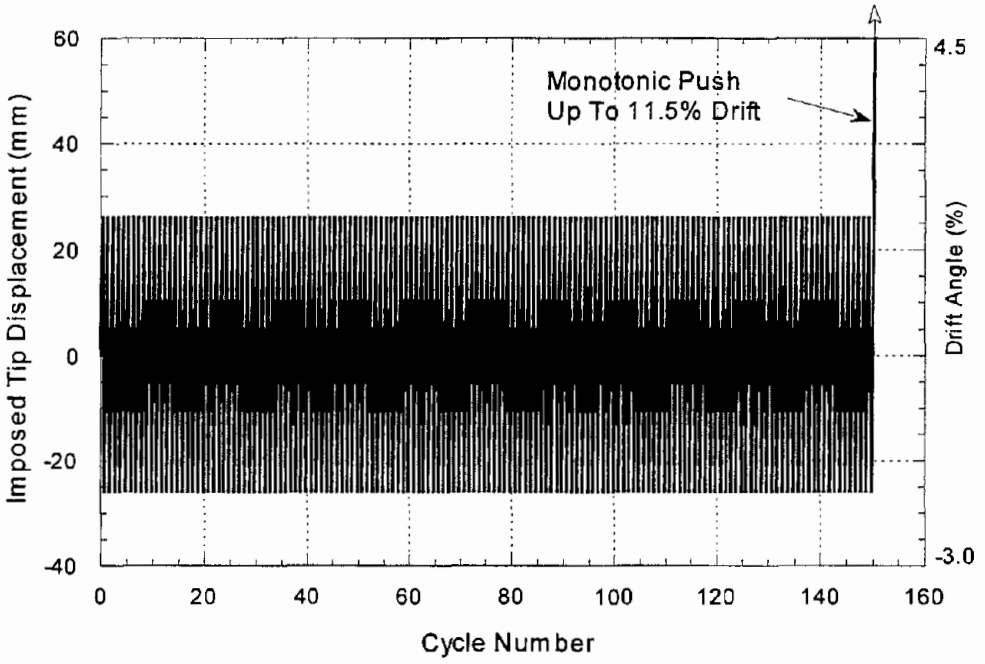

FIGURE 4-11 Displacement History Applied to Column A3

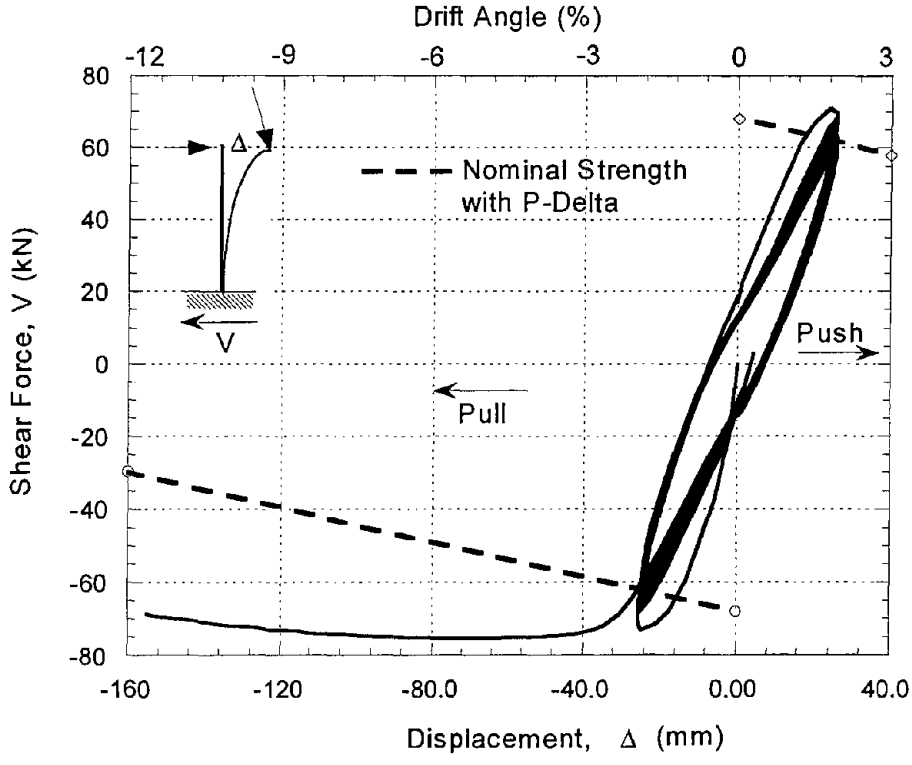

FIGURE 4-12 Shear vs. Displacement Response of Column A3

4.3.2 Specimen A4: Constant Amplitude Cycles at 4% Lateral Drift

Specimen A4 was tested under repeated cyclic loading at a constant displacement amplitude of ± 57 mm until failure. This displacement was equal to a drift of approximately 4.0%. The applied axial load was 222 kN which corresponds to the desired axial stress based on $0.1 f_c' A_g$. On the very first cycle, deterioration (spalling) was observed on the compression side of the specimen. In the second cycle, cracks propagated along the length from the base of the specimen. In the third cycle, spalling had progressed to approximately 150 mm on both sides of the specimen. At the end of the fifth cycle, the crack width was approximately 1.5mm which increased to about 2 mm in the next cycle. At cycle 8, the plastic hinge was fully developed was estimated to be about 150-160 mm.

On continuing to load the specimen, cracks propagation and spalling of concrete on both sides increased significantly. Buckling of longitudinal bars was observed on both sides of the specimen. This led to necking of the confining spiral reinforcement. It was clear at this point that the load capacity of the specimen was beginning to decrease and failure of the specimen was eminent. It was also observed that a certain threshold demand on the column was being surpassed beyond which stiffness and strength of well-confined columns begin to degrade

rapidly. This may also be considered as an irreparable damage limit state. Following cycle 25 and heading toward the peak displacement at cycle 26 a spiral approximately in the middle of the plastic hinge zone ruptured on the tension side. Table 4-5 gives a detailed summary of test observations for column A4. Figure 4-13 shows the condition of specimen A4 after 18 cycles of loading. Spalling of the cover and exposed reinforcement is visible at this stage. The state of the column at the end of testing is shown in Figure 4-14. Figure 4-15 shows the imposed constant-amplitude displacement history applied to specimen A4. The resulting force vs. displacement response history is displayed in Figure 4-16.

TABLE 4-5 Summary of Test Observations for Specimen A4

LOADING TYPE: Constant Amplitude Cycles at 4% Lateral Drift

LOADING AND DISPLACEMENT VALUES OF INTEREST:

Axial Load :	222 kN
Maximum Lateral Load:	72 kN
Cracking Load:	20 kN
Yield Load:	64 kN
Yield displacement:	16 mm
Failure Mode:	Spiral Rupture on the Left Side.

DAMAGE OBSERVARTIONS:

Cycle No.	Notes
1	First Cracking
1	Spalling of cover concrete
1	Yielding
3	Significant Spalling
18	Necking of spirals, some bar buckling
25-26	Hoop Failure

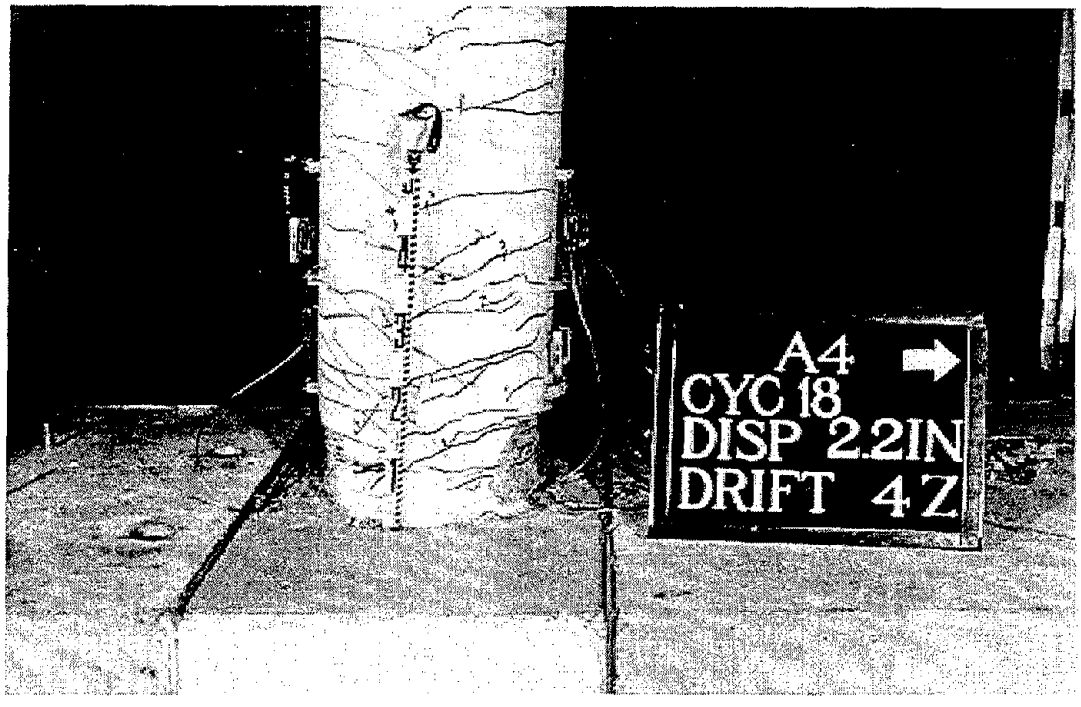

FIGURE 4-13 Condition of Specimen A4 at Cycle No. 18

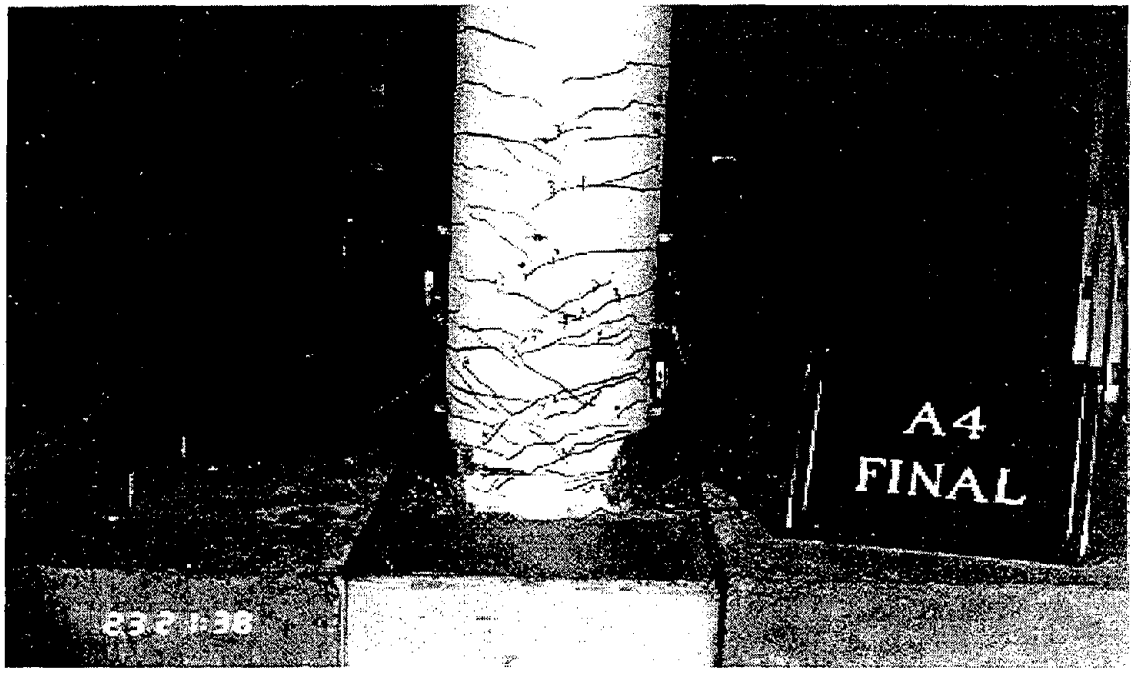

FIGURE 4-14 Specimen A4 at End of Testing

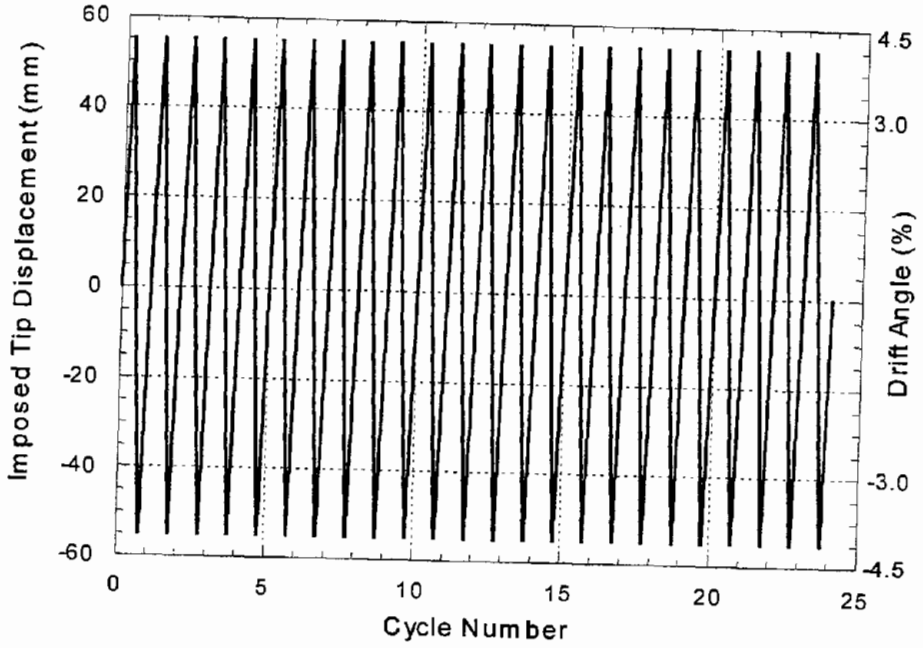

FIGURE 4-15 Displacement History Applied to Column A4

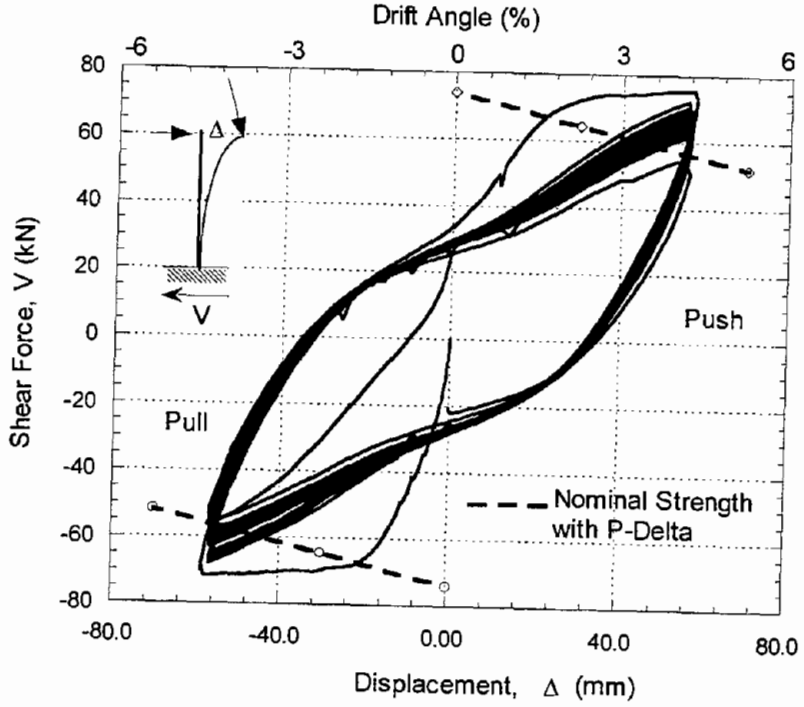

FIGURE 4-16 Shear vs. Displacement Response of Column A4

4.3.3 Specimen A5: Constant Amplitude Cycles at 5.5% Lateral Drift

Specimen A5 was tested under repeated cyclic loading at a constant amplitude of ± 75 mm corresponding to a drift of approximately 5.5%. The axial load applied was kept constant at 222 kN throughout the testing. Since the maximum displacement in the very cycle was slightly in excess of 5.5%, cracking, yielding and spalling of the concrete cover were all observed in the very first push to the peak displacement. Testing continued at a steady rate with reversed cyclic loads being applied to the same peak amplitudes in both directions. Crack widths exceeded 2.5 mm by the end of the sixth cycle and spalling had progressed beyond 150 mm. The plastic hinge length was recorded at an average value of 175 mm. Significant buckling of longitudinal bars was observed on both sides of the specimen at cycle 9. This led to necking of the confining reinforcement. The specimen failed through rupture of a longitudinal bar before cycle 10 was completed.

Table 4-6 presents a summary of test observations for specimen A5. Figure 4-17 shows the condition of specimen A5 after 3 cycles of loading. The state of the column at the end of testing is shown in Figure 4-18. Figure 4-19 shows the constant-amplitude displacement history applied to specimen A5. The resulting lateral force vs. displacement response history is displayed in Figure 4-20.

TABLE 4-6 Summary of Test Observations for Specimen A5

LOADING TYPE: Constant Amplitude Cycles at 5.5% Lateral Drift

LOADING AND DISPLACEMENT VALUES OF INTEREST:

Axial Load :	222 kN
Cracking Load and Displacement:	18 kN and 5 mm
Yield Load:	64 kN
Yield displacement:	20 mm
Maximum Lateral Load:	93 kN
Failure Mode:	Bar Rupture on the Left Side.

DAMAGE OBSERVATIONS:

Cycle No.	Notes
1	Cracking, spalling and yielding
3	Significant Spalling
8	Some buckling, necking of spirals
9	Failure

FIGURE 4-17 Specimen A5 at Cycle No. 3

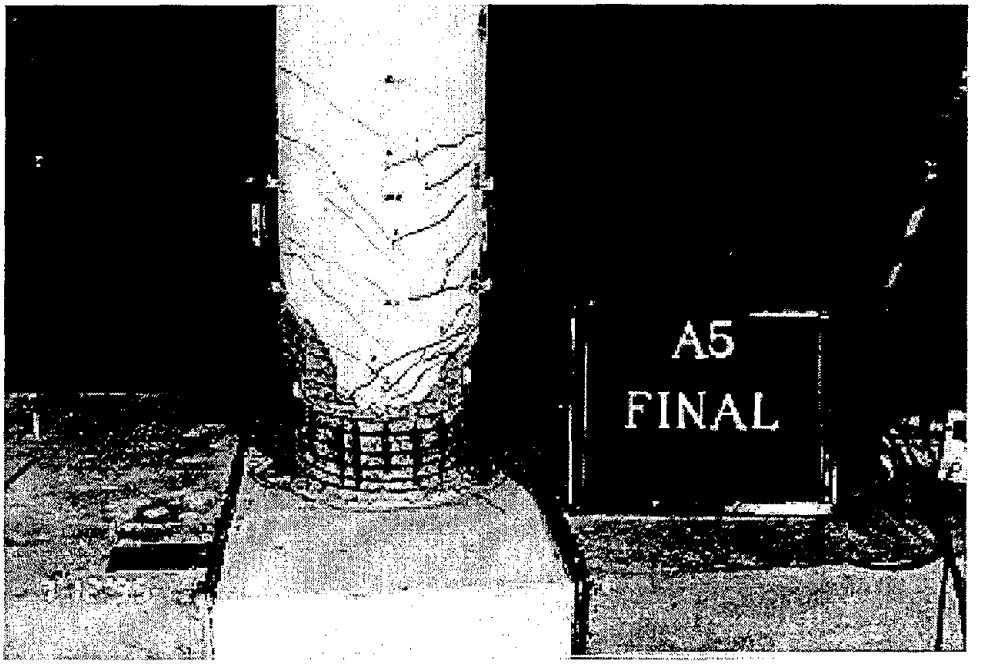

FIGURE 4-18 Condition of Specimen A5 at End of Testing

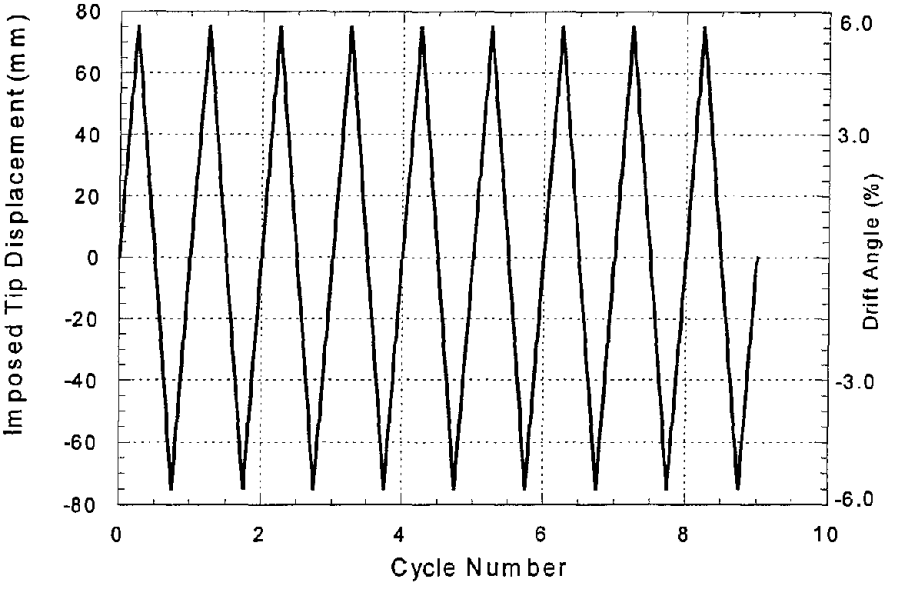

FIGURE 4-19 Displacement History Applied to Column A5

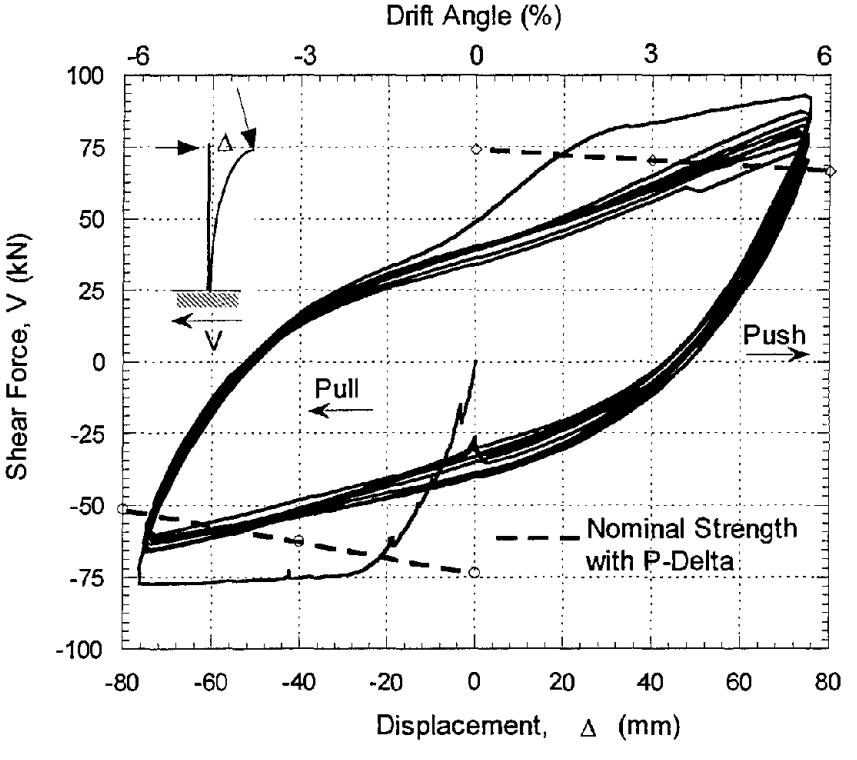

FIGURE 4-20 Shear vs. Displacement Response of Column A5

4.3.4 Specimen A6: Constant Amplitude Cycles at 7% Lateral Drift

This was the fourth and final specimen to be tested under constant amplitude loading. Specimen A6 was tested under repeated cyclic displacement of ± 95 mm (corresponding to approximately 7% drift) to failure. The compressive strength of the specimen on the day of testing was 36 MPa. The applied axial load was 222 kN which remained constant throughout the testing.

Again, the relatively high amplitude produced cracking, yielding, and spalling of concrete in the very first cycle. Cracks propagated rapidly and the spalling extended beyond 175 mm on both sides of the specimen. Within two cycles, severe buckling of most of longitudinal bars occurred on both side of the specimen. The visible bulging of the spirals caused by necking of the confining reinforcement was a sure sign of distress. A significant drop in strength capacity and system stiffness was noted. The plastic hinge length was recorded to be 250 mm. At cycle 3, a spiral ruptured on the tension side of specimen.

Table 4-7 presents a summary of recorded test observations for specimen A6. Figure 4-21 shows the condition of specimen A6 just prior to failure. A closer view of the state of the column at the end of testing is shown in Figure 4-22. Figure 4-23 shows the displacement history applied to specimen A6. The resulting lateral force vs. displacement response is displayed in Figure 4-24.

TABLE 4-7 Summary of Test Observations for Specimen A6

LOADING TYPE: Constant Amplitude Cycles at 7% Lateral Drift

LOADING AND DISPLACEMENT:

Axial Load :	222 kN
Maximum Lateral Load:	76 kN
Cracking Load:	20 kN
Cracking Displacement:	5 mm
Yield Load:	66 kN
Yield displacement:	18 mm
Failure Mode:	Spiral Rupture on the Left Side.

DAMAGE OBSERVATIONS:

Cycle No.	Notes
1	Spalling commenced at quarter cycle
1	Yielding (well before end of cycle)
2	Significant Spalling, necking of spirals, buckling of longitudinal bars
3	Failure

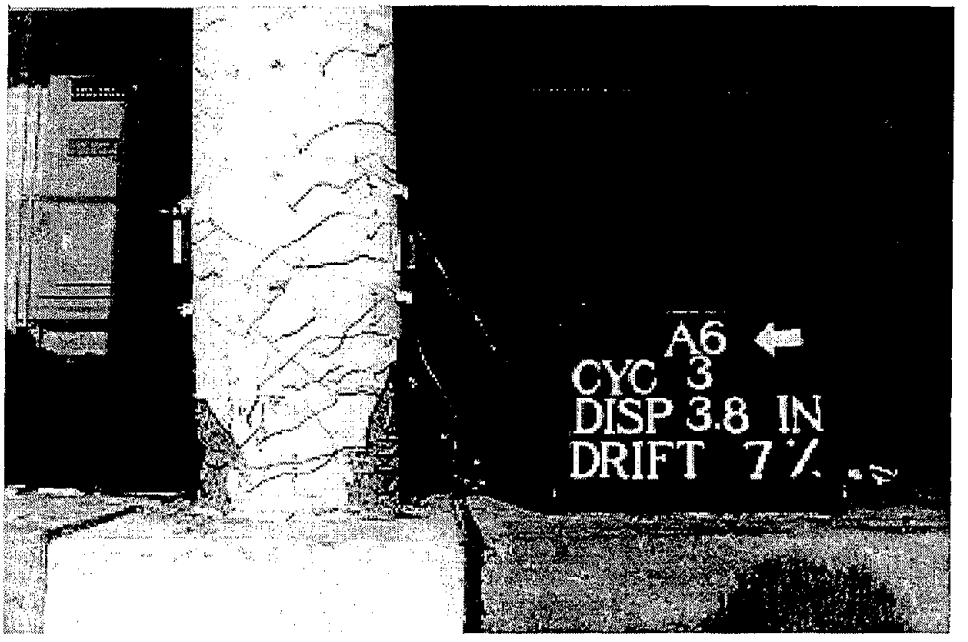

FIGURE 4-21 Specimen A6 at Cycle No. 3

FIGURE 4-22 Specimen A6 at End of Testing

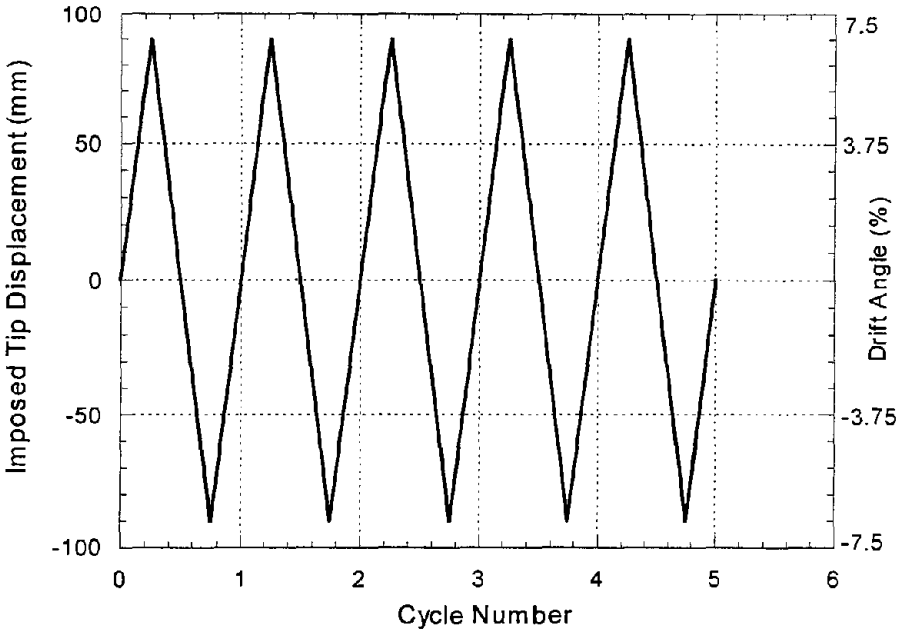

FIGURE 4-23 Displacement History Applied to Column A6

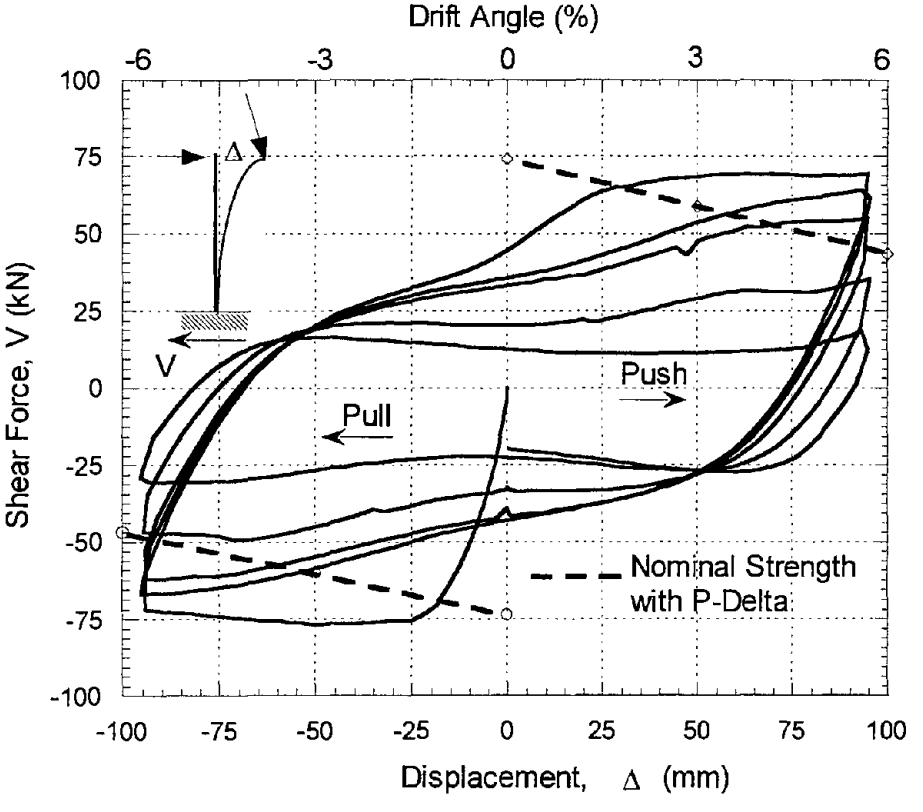

FIGURE 4-24 Shear vs. Displacement Response of Column A6

5.0 CUMULATIVE DAMAGE TESTING II: RANDOM CYCLIC LOADING

The benchmark tests and low-cycle fatigue loading completed in the first phase of testing provided the necessary information to validate the analytical model and develop the random displacement histories required for the second phase of testing. This section will cover aspects dealing with the choice of ground motion, the generation and selection of displacement histories, and results and observations during testing.

5.1 Background and Selection of Random Histories

The main objective of the test program was to verify the behavior of bridge piers responding in flexure to a random displacement input such as those typically experienced under earthquake loading. The testing was divided into two phases: the first phase was meant primarily to develop certain benchmark parameters against which to compare the random response. The second phase was directed at examining the effects of load path on cumulative damage and energy-dissipation capacity. It was essential, from a practical and damage calibration point of view, to choose an appropriate set of displacement histories so that the number of imposed cycles was reasonable (not so excessive as to require testing to continue beyond one day) and that the damage incurred would lead to potential failure at the end of each test.

A suite of over fifty earthquakes, mostly recorded activity in the west coast of the United States, was selected for a preliminary study. The analytical model of the bridge pier, calibrated using the force-deformation response from Specimen A2, was utilized in a extensive simulation study to obtain the final sequence of displacements. Prior to carrying out the simulation study, a desired sequence of events was chosen. For example, the first specimen was to be subjected to the following sequence of loads:

1. A major earthquake causing significant but repairable damage
2. A minor earthquake representing a possible aftershock
3. Another minor event signifying additional earthquakes prior to another major earthquake
4. A final severe event sufficiently large enough to cause failure of the column

In order to achieve such a desired sequence of events and the corresponding damage states, it was necessary to calibrate some measure of damage. A fatigue-based approach was used in which the number of cycles to failure, based on results of the experimental testing in the first phase, formed the basis of defining a certain degree of damage. The elastic cycles were generally ignored in the damage quantification. To illustrate how the procedure was applied in developing the final displacement amplitudes, consider the following situation. An earthquake induces about 30 response cycles of which only four exceed the yield displacement as follows: 2 cycles at 3% drift, 1 cycles at 4% drift and 1 cycle at 5%drift. Based on the results of Phase I testing, the model columns sustained 26 cycles at 3% drift, 9 cycles at 4% drift and 4 cycles at 5% drift. Hence the cumulative damage under the imposed earthquakes was estimated, using Miner's linear damage accumulation rule, as follows:

$$(2/26 + 1/9\ 1/4) = 0.44$$

which is likely to inflict significant damage on the specimen but is perhaps repairable. A second similar event would certainly damage the specimen beyond repair.

In order to achieve a desired damage scenario, it was necessary to try innumerable combinations. An additional problem in the numerical simulations was the fact that the records were concatenated so as to retain the damaged state and stiffness characteristics at the end of each event. Hence, an earthquake that may have been damaging in the initial state of the structure may not have any significant effect when applied a second time. After many trials, however, including the need to scale some records, it was possible to develop three separate damage scenarios, the details of which are summarized in the next section.

5.2 Selected Ground Motions

A total of 10 earthquakes were used in the final simulations for the three separate damage scenarios considered in this study. Each of the three sets of displacements were utilized twice: during the second usage the sequence of the applied displacements were altered so as to force the system to follow a different load path. Hence, there were truly only three sets of displacement histories used, and each was repeated a second time but applied in a different sequence. Table 5-1 presents a complete summary of the earthquake records that were applied.

The accelerograms and the corresponding spectra used as input motion for simulating the displacement histories for specimens A7 - A12 are shown in Figures 5-1 through 5-3. Note that the accelerations shown include all the earthquakes selected for a given damage scenario. The analysis was not repeated for the next specimen to develop a new time history by rearranging the input motions, rather the displacements from the first simulation were rearranged to simply alter displacement paths on the assumption that some random combination of ground motions could produce such a displacement path. It is important to remember that one of the primary purposes of the testing is to investigate effects of load paths. Hence it was essential to use the same "total" displacement history without introducing additional cycles or altering amplitudes.

Analysis of the model column subjected to the earthquakes shown in Figures 5-1 through 5-3 was carried out using IDARC. Model properties were identified from results of Phase I testing and have been presented in Section 3 of this report. Results of Phase II testing using the analytically simulated displacements are presented in the next section.

5.3 Random Loading: Testing and Observations

As indicated previously, the random displacement histories were composed of three independent sets of time histories generated through analysis of the model specimen using IDARC. Details of the testing and relevant damage observations are described in subsequent sections.

TABLE 5-1a Ground Motions Selected for Generating Random Displacement Histories for Specimens A7 - A9.

Specimen	Event	Description	Purpose	Record	Scale*	PGA,g
A7	1	Damaging earthquake	First major event	Loma Prieta 1989 Presidio	12.0	1.20
	2	Minor earthquake	Aftershock	Imperial Valley 1979 Superstition Mt.	1.8	0.34
	3	Minor earthquake	2 nd aftershock	San Fernando 1971 2011 Zonal Ave.	1.2	0.10
	4	Severe earthquake	Failure of bridge	San Fernando 1971 455 S Figueroa St	3.6	0.54
A8	1	Minor earthquake	Minor damage	Imperial Valley 1979 Superstition Mt.	1.8	0.34
	2	Minor earthquake	Additional damage	San Fernando 1971 2011 Zonal Ave.	1.2	0.10
	3	Damaging earthquake	First major event	Loma Prieta 1989 Presidio	12.0	1.20
	4	Severe earthquake	Failure of bridge	San Fernando 1971 455 S Figueroa St	3.6	0.54
A9	1	Major earthquake	First major event	San Fernando 1971 Orion Blvd.	3.25	1.43
	2	Minor earthquake	Aftershock damage	San Fernando 1971 2011 Zonal Ave.	1.2	0.10
	3	Moderate earthquake	Additional damage	El Centro 1940	1.0	0.35
	4	Minor earthquake	Aftershock	San Fernando 1971 455 S Figueroa St	1.0	0.15
	5	Severe earthquake	Failure of structure	San Fernando 1971 Orion Blvd	3.25	1.43

* Multiplying factor on acceleration amplitude

TABLE 5-1b (continued) Ground Motions Selected for Generating Random Displacement Histories for Specimens A10 - A12.

Specimen	Event	Description	Purpose	Record	Scale*	PGA,g
A10	1	Minor earthquake	Minor damage	San Fernando 1971 2011 Zonal Ave.	1.2	0.10
	2	Moderate earthquake	Additional damage	El Centro 1940	1.0	0.35
	3	Minor earthquake	Aftershock	San Fernando 1971 455 S Figueroa St	1.0	0.15
	4	Major earthquake	First major event	San Fernando 1971 Orion Blvd.	3.25	1.43
	5	Severe earthquake	Failure of structure	San Fernando 1971 Orion Blvd	3.25	1.43
A11	1	Major event	First damaging earthquake	Northridge 1994 VA Hospital	1.0	0.42
	2	Minor earthquake	Aftershock	Northridge 1994 Griffith observatory	1.0	0.26
	3	Minor earthquake	Additional damage	Taft 1952	1.0	0.36
	4	Severe earthquake	Failure of column SCT	Mexico City 1985	1.0	0.17
A12	1	Minor earthquake	Minor damage	Northridge 1994 Griffith observatory	1.0	0.26
	2	Minor earthquake	Additional damage	Taft 1952	1.0	0.36
	3	Major event	First damaging earthquake	Northridge 1994 VA Hospital	1.0	0.42
	4	Severe earthquake	Failure of column SCT	Mexico City 1985	1.0	0.17

* Multiplying factor on acceleration amplitude

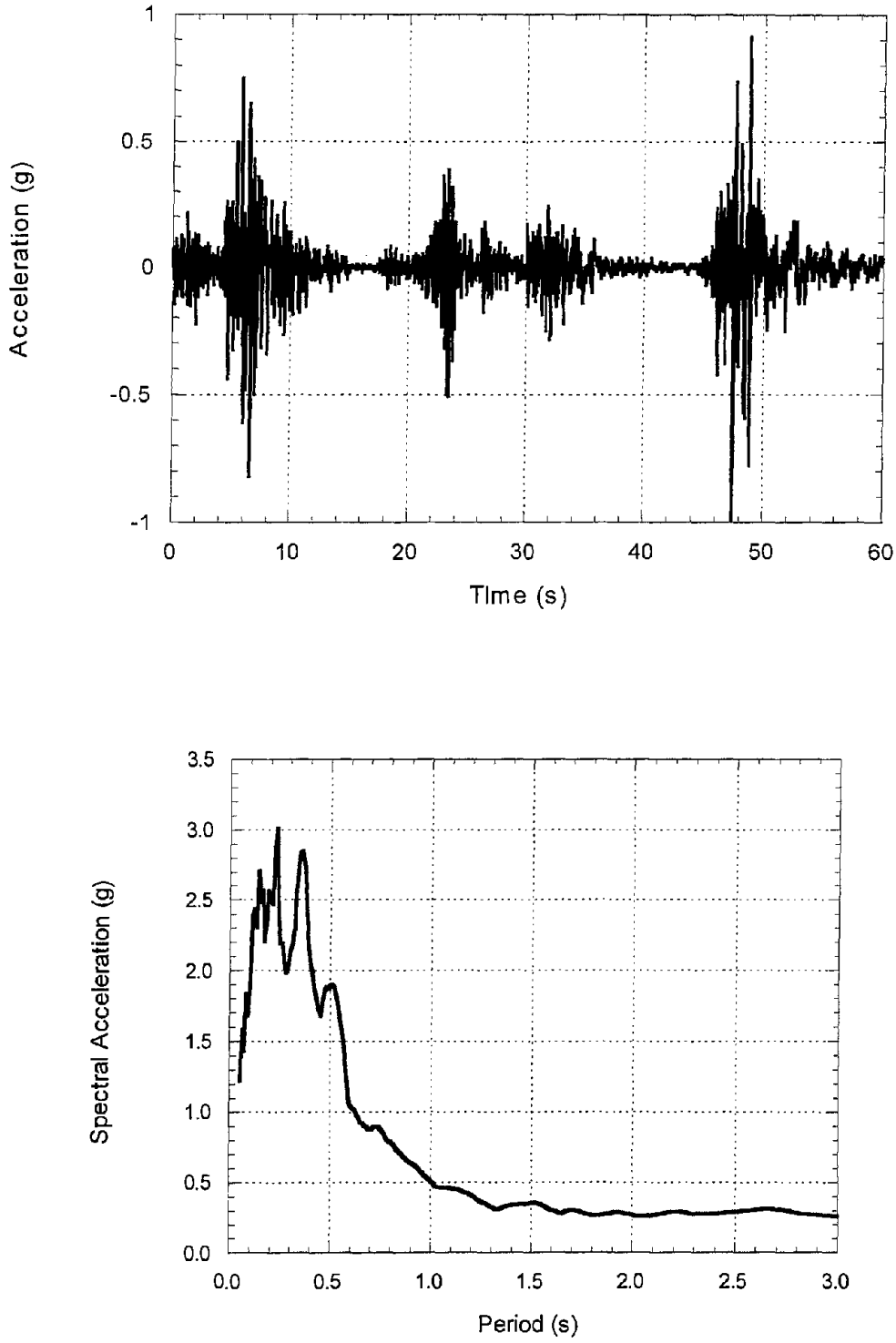

FIGURE 5-1 Acceleration History and Corresponding 5% Damped Spectra for Input Motions Used to Generate Displacement History for Specimens A7 and A8

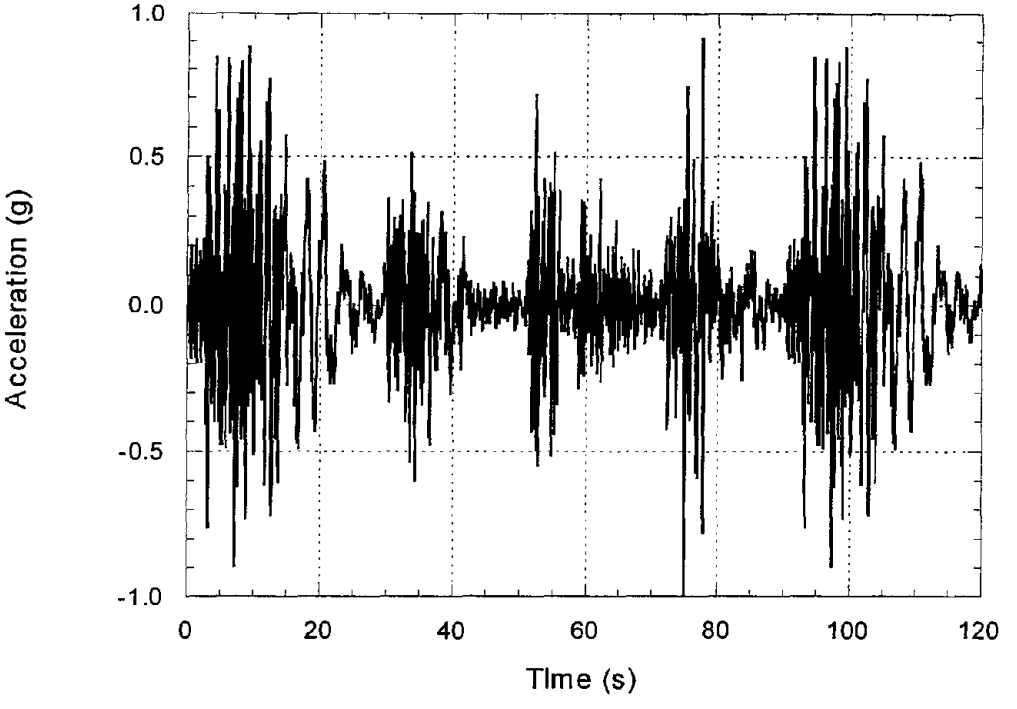

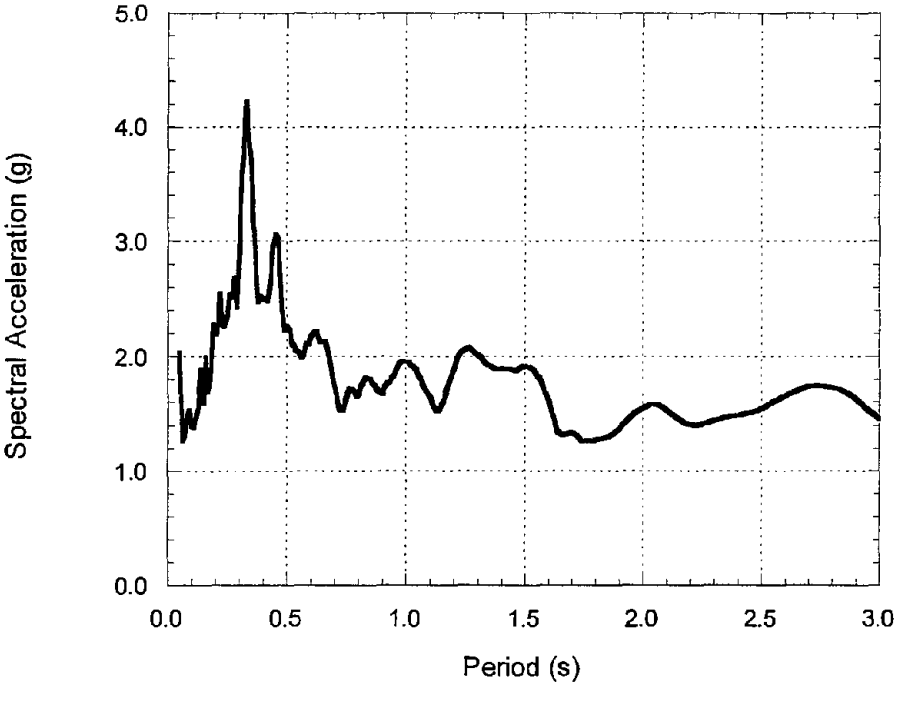

FIGURE 5-2 Acceleration History and Corresponding 5% Damped Spectra for Input Motions Used to Generate Displacement History for Specimens A9 and A10

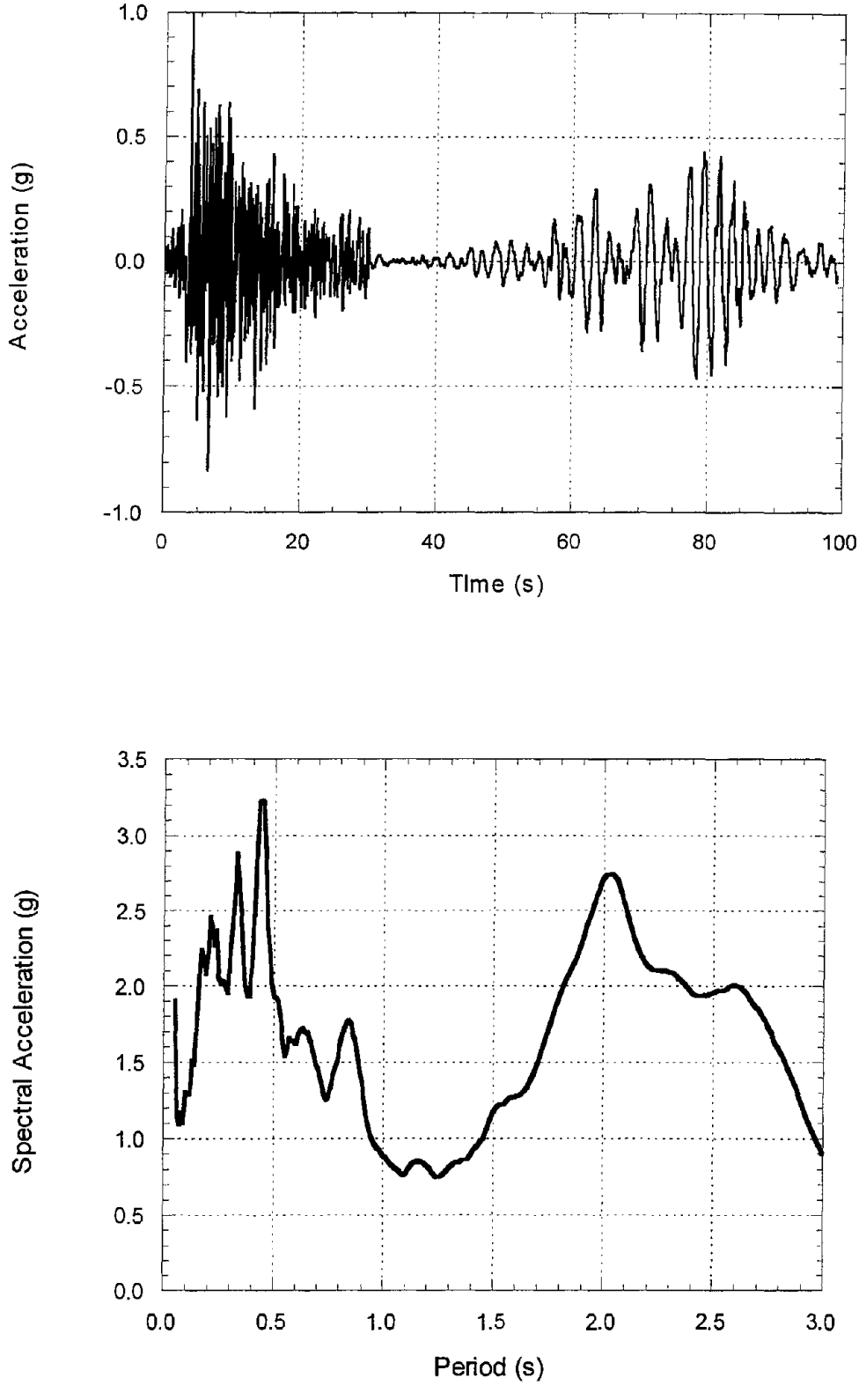

FIGURE 5-3 Acceleration History and Corresponding 5% Damped Spectra for Input Motions Used to Generate Displacement History for Specimens A11 and A12

5.3.1 Specimen A7

Specimen A7 was subjected to random displacement cycles generated from four different earthquakes. The actual acceleration records and associated PGA's used and the intended damage scenario were shown in Table 5-1. The first record produced significant displacements which was considered sufficient to induce moderate damage to the specimen. The next two earthquakes were meant to represent aftershocks and/or other minor events which do not result in any further significant damage. The final ground motion was so selected to produce severe damage and probable failure of the system.

First cracking occurred after 22 cycles (or 45 half-cycles) of loading at a lateral drift of about 1%. On the reverse cycle, at a drift exceeding 1.5%, cracking started in the opposite face of the column accompanied by considerable spalling which extended up to 100 mm from the base of the pier. At the end of the 26th cycle, spalling of the cover had taken place on both sides of the column and cracks had propagated even further along the length. Before cycle 32 was completed, the specimen had undergone one complete cycle at a drift amplitude of approximately 5%. At this point, some buckling of the longitudinal bars was observed on one side of the specimen. The next forty cycles were uneventful since it was composed of elastic cycles with drifts under 0.5%. At the half cycle corresponding to #145, which was part of the second earthquake, the spalling had stabilized and the slightly buckled longitudinal bars were clearly visible. The loading had progressed into the third minor earthquake and 94 cycles of displacement had already been applied and no significant damage progression was observed. The third earthquake did induce up to one and a half cycles of 2.5% drift by the end of the 110 th cycle. Buckling was observed in 4 bars on each side by this point. No further extension of the plastic hinge length took place, and crack widths were measured between 2.5 - 4 mm. Finally, at half cycle #269, and a drift of almost 6%, failure of the specimen was recorded following the rupture of the spiral in the plastic hinge zone. This occurred during the peak displacement demand of the fourth earthquake. In all, the specimen had undergone about 8 inelastic cycles of displacement at an average drift of about 3.6%. Table 5-2 provides a detailed summary of the test observations.

Figures 5-4 and 5-5 present visually observed damage towards the end of testing. The applied displacement history and the resulting force-deformation hysteresis are shown in Figures 5-6 and 5-7, respectively.

TABLE 5-2 Summary of Observations During Testing of Specimen A7

LOADING TYPE:	Simulated Seismic (Random) Loading
Concrete Strength:	32.8 MPa

LOADING AND DISPLACEMENT VALUES OF INTEREST:

Axial Load :	222 kN
Yield Load:	60 kN
Yield Displacement:	16 mm
Maximum Lateral Load:	78 kN
Maximum Lateral Displacement:	82.5 mm
Failure Mode:	Spiral Ruptured on the Left Side

DAMAGE OBSERVATIONS:

Half Cycle No.	Notes
45	First Cracking
49-52	Spalling
64	Significant Spalling
220	Visible buckling of longitudinal bars
269-270	Spiral Failure

FIGURE 5-4 Damage to Specimen A7 at Half Cycle No. 145 During Earthquake #2

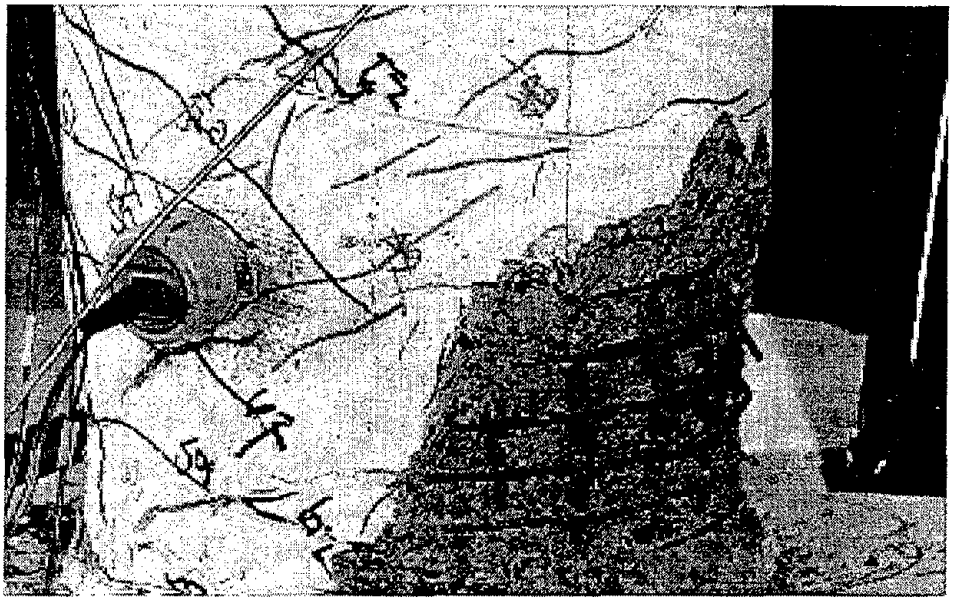

FIGURE 5-5 Final Damaged State of Specimen A7

5.3.2 Specimen A8

The displacement history imposed on Specimen A8 was essentially the same as that used in specimen A7, but the sequence of events were changed (see Table 5-1). The two minor events were applied first followed by the two major earthquakes. In order to investigate effects of load path, it was necessary to use the same number of cycles and amplitudes with the exception that they be applied in a different sequence.

First cracking occurred at half-cycle #33 of earthquake 1 on the left side of the specimen. By the end of cycle 23 or half-cycle #46 of the earthquake 1, spalling on the same side of the specimen was noticed. Cracking and spalling continued and became fairly significant around the end of cycle #57 at which time the specimen experienced one full inelastic cycle at a drift of nearly 3%. The third earthquake commenced at about cycle #90. Significant spalling on both sides of the column was observed by the end of half-cycle #209. The spirals and longitudinal rebars were exposed along the plastic hinge zone. Some buckling of the longitudinal bars was noticed towards the end of cycle 110 following a few inelastic cycles at drifts exceeding 2.5%. At half cycle # 267, during the peak displacement demand of earthquake #4, necking of one of the spiral bands was observed. In the next cycle, at approximately the same cycle at which failure occurred in specimen A7, rupture of the spiral reinforcement took place.

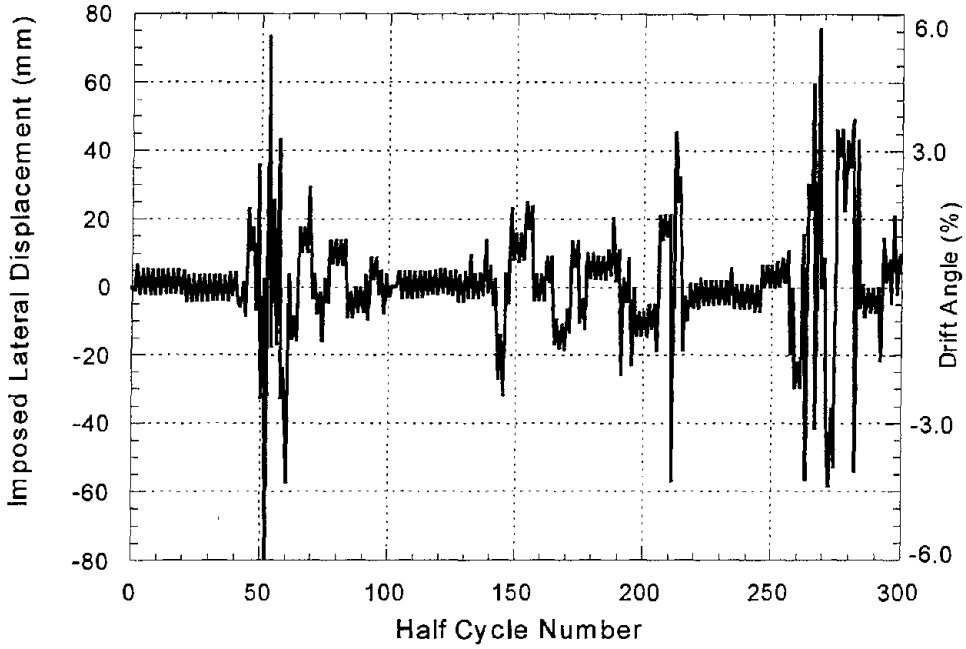

FIGURE 5-6 Displacement History Applied to Column A7

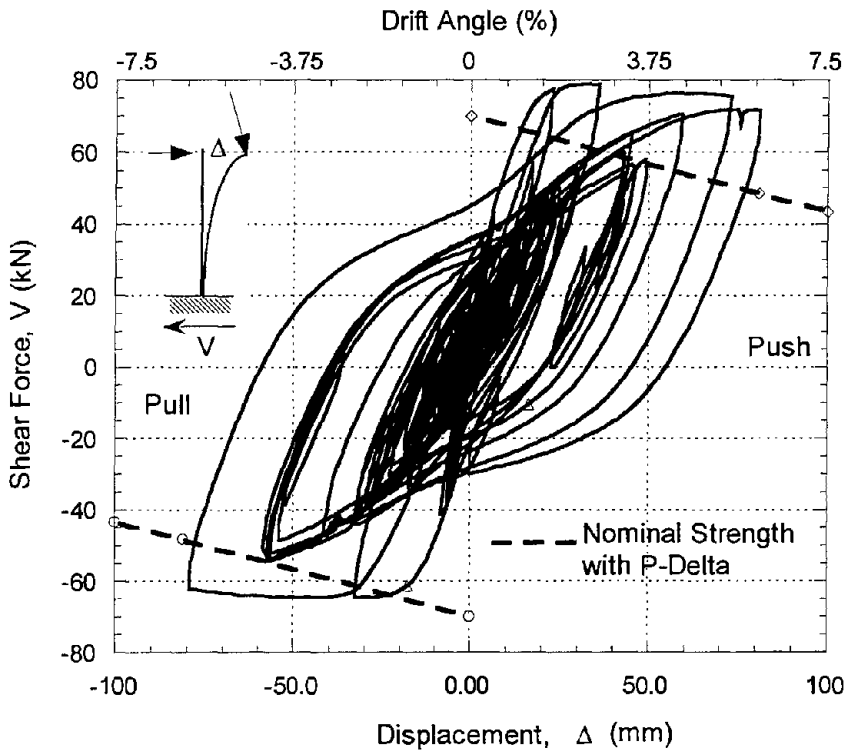

FIGURE 5-7 Force vs. Displacement Response of Column A7

The specimen continued to be loaded to observe loss of strength capacity. A second spiral, next to the previously ruptured spiral, failed in the following half cycle. The plastic hinge length at this stage was about 150 mm. The specimen continued to be loaded until the end of earthquake #4, but no further rebar or spiral fracture occurred. It must be remembered that the total displacement history was identical to specimen A7, hence the failure of specimen A8 at about the same stage of loading indicated that the load path did not influence the cumulative damage of this specimen. Table 5-3 summarizes all observations during testing of this specimen.

Figure 5-8 displays the accumulated damage to the specimen towards the end of the loading when significant spalling, necking of spiral reinforcement and some visible buckling of the longitudinal bars had already taken place. Figure 5-9 shows the failure of the two spirals. The sequence of the imposed displacements is shown in Figure 5-10 while the resulting force-deformation response is shown in Figure 5-11.

TABLE 5-3 Summary of Observations During Testing of Specimen A8

LOADING TYPE:	Simulated Seismic (Random) Loading
Concrete Strength:	32.8 MPa

LOADING AND DISPLACEMENT VALUES OF INTEREST:

Axial Load :	222 kN
Cracking Load:	20 kN
Cracking Displacement:	3 mm
Yield Load:	64 kN
Yield Displacement:	15.5 mm
Maximum Lateral Load:	72 kN
Maximum Lateral Displacement:	81.5 mm
Failure Mode:	Two Spirals Ruptured on the Left Side.

DAMAGE OBSERVATIONS:

Half Cycle No.	Notes
33	First Cracking
46-47	Spalling
114	Significant Spalling
220	Buckling of longitudinal bar
267	Necking of spiral reinforcement
270	Two Spirals Failed on the Left Side

FIGURE 5-8 Specimen A8 at Half-Cycle # 267 During Earthquake 4

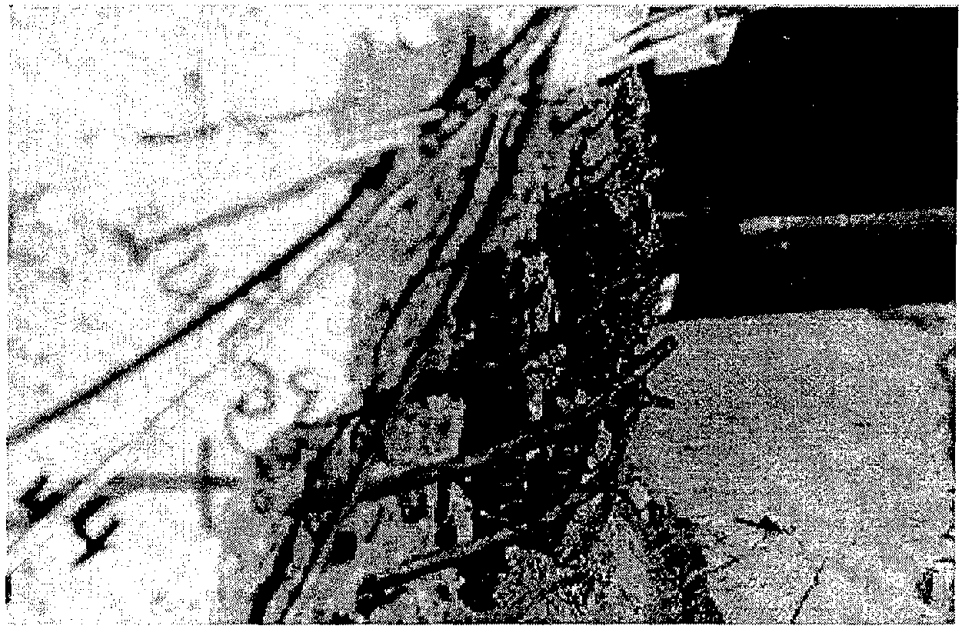

FIGURE 5-9 Specimen A8 at Final Damaged State

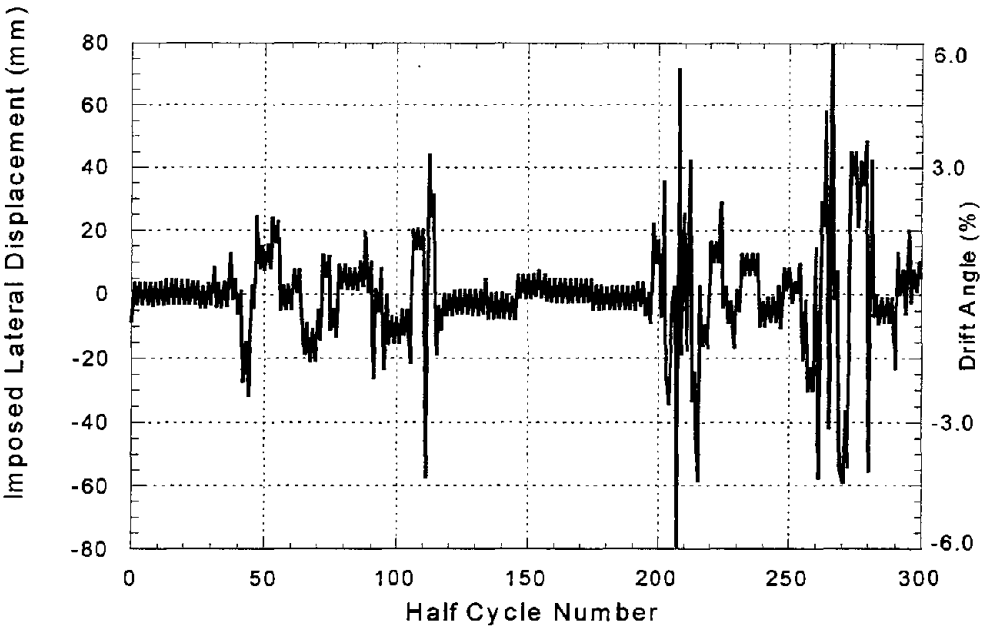

FIGURE 5-10 Displacement History Applied to Column A8

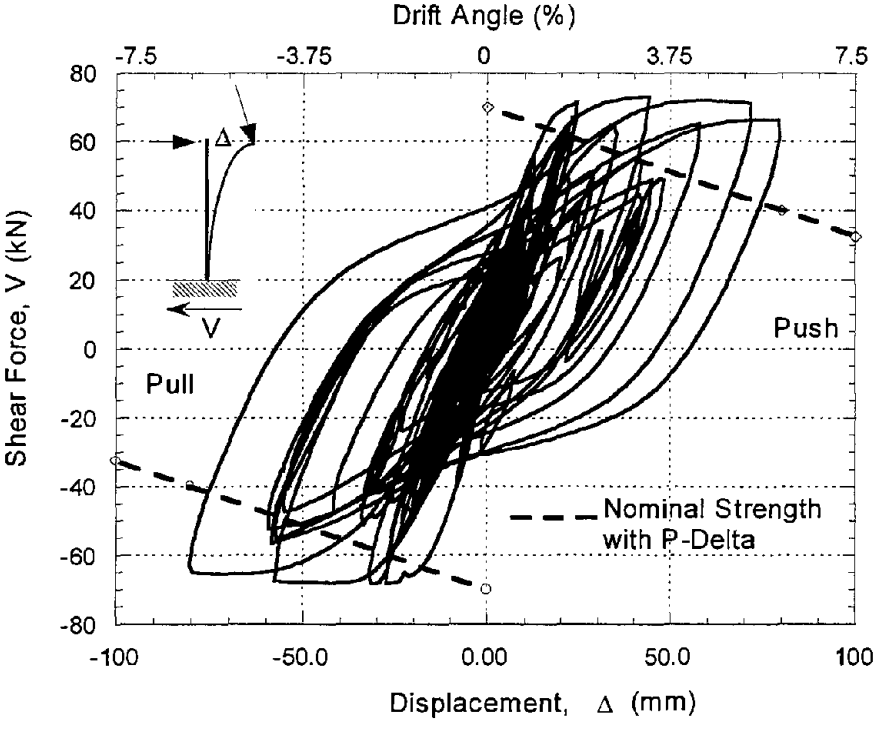

FIGURE 5-11 Shear Force vs. Displacement Response of Column A8

5.3.3 Specimen A9

Column A9 was tested under simulated random displacements resulting from a series of five different earthquakes (see Table 5-1). A fifth earthquake was used in this specimen to introduce additional small amplitude cycles between two large events.

Hair-line cracks were first observed at half-cycle # 22 of earthquake #1 at a lateral displacement of 8 mm (about 0.5% lateral drift) on the left side of the specimen. The first significant crack was observed on the right side of the specimen at half cycle # 29 (about 14 full cycles) when the lateral drift reached 2% in one cycle. First spalling occurred at half-cycle # 49 of the first earthquake on the left side of the specimen accompanied by major crack propagation. Spalling took place on the opposite side of the specimen in the very next cycle at a drift exceeding 3%. After nearly five inelastic cycles at an average drift of 3.0% , the crack widths had reached about 2.0 mm.

The next two earthquakes did not produce any significant damage since all of the imposed drifts remained less than 1.5%. Earthquake #4 was of moderate intensity and was composed of about 2 inelastic cycles at a drift of about 2.5%. By the end of this event, at half-cycle #190, minor buckling was noticed in the longitudinal bars. However, it appeared that the specimen was still repairable. The buckling of longitudinal bars increased and became more prominent during cycle #120 (or half-cycle #240) of the fifth and final earthquake. At half-cycle #260, at an imposed drift exceeding 5.5%, failure of one of the spirals occurred on the left side of the specimen.

Figure 5-12 displays the state of damage at the end of cycle # 94, following which the initial buckling of the longitudinal bars was observed. Figure 5-13 shows the failure of the hoop reinforcement at the center of the plastic hinge. The plastic hinge length stabilized at approximately 200 mm towards the end of testing.

The entire displacement history generated by IDARC and applied to specimen A9 is displayed in Figure 5-14. The base shear vs. lateral displacement hysteresis of the bridge column is plotted in Figure 5-15. A summary of observations during testing is reported in Table 5-4.

5.3.4 Specimen A10

Specimen A10 was subjected to essentially the same displacement history as Specimen A9, however, the sequence of applied displacements was different. The objective of altering only the sequence of loading was to monitor the effect of load path on the capacity of the specimen. A similar test conducted on Specimen A8 did not reveal any significant influence of load path, however, in this test a larger number of low-amplitude cycles were introduced between cycles of larger amplitudes.

TABLE 5-4 Summary of Observations During Testing of Specimen A9

LOADING TYPE:	Simulated Seismic (Random) Loading
Concrete Strength:	32.5 MPa
LOADING AND DISPLACEMENT VALUES OF INTEREST:	
Axial Load :	222 kN
Cracking Load:	20.5 kN
Cracking Displacement:	5 mm
Yield Load:	65 kN
Yield Displacement:	16.5 mm
Maximum Lateral Load:	75 kN
Maximum Lateral Displacement:	91.6 mm
Failure Mode:	Two Spirals Ruptured on the Left Side.

DAMAGE OBSERVATIONS:

Half-Cycle No.	Notes
22	First Cracking
49	Spalling
122	Significant Spalling
190	Initial buckling of longitudinal bar
260	Spiral Failed on the Left Side of Column A9

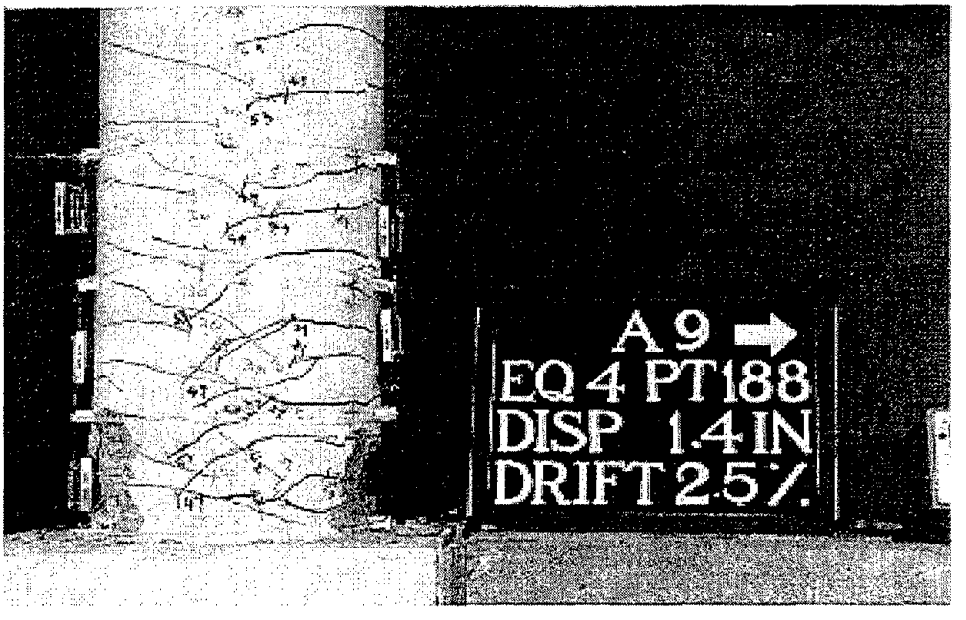

FIGURE 5-12 Damage to Specimen A9 at end of Half-Cycle 188

FIGURE 5-13 Final Damaged State of Specimen A9

The axial load on this specimen had to be reduced because the concrete strength obtained from cylinder testing was lower than the previous three specimens which were cast from a different batch. All tests were conducted at an axial stress of $0.1f_c'$.

The first sign of damage in the form of hair-line cracks was observed at cycle #6 on the right side of the specimen. Cracking of the left side was noticed in the very next cycle in the reverse direction of loading. Crack widths at this stage of loading was about 1 mm. and were distributed from the base up to a distance of 450 mm. At half-cycle #30, some signs of spalling were observed on the left side. Earthquake #1 did not cause any further damage. The second earthquake, like the first, induced only one significant cycle of displacement which resulted in a lateral drift of about 2%. At half-cycle # 121, which was part of the third earthquake, spalling was observed on the right side of the specimen. This was a moderate earthquake with only a few cycles beyond 2% drift. At the end of this earthquake, at approximately half-cycle # 194, the column did not sustain any irreparable damage.

Significant buckling of the central longitudinal bar was recorded at half-cycle # 258. This was part of the peak displacement amplitude of earthquake #5. Accompanying this was some necking of the spirals - a normal tendency following the initiation of longitudinal bar buckling. The very next cycle resulted in failure of one of the spirals. The plastic hinge length was estimated between 190 – 200 mm.

Figure 5-16 displays the state of damage at the end of half-cycle # 122 at which point significant spalling of the cover concrete in the plastic zone was observed. Figure 5-17 shows the failure of the hoop reinforcement at the center of the plastic hinge.

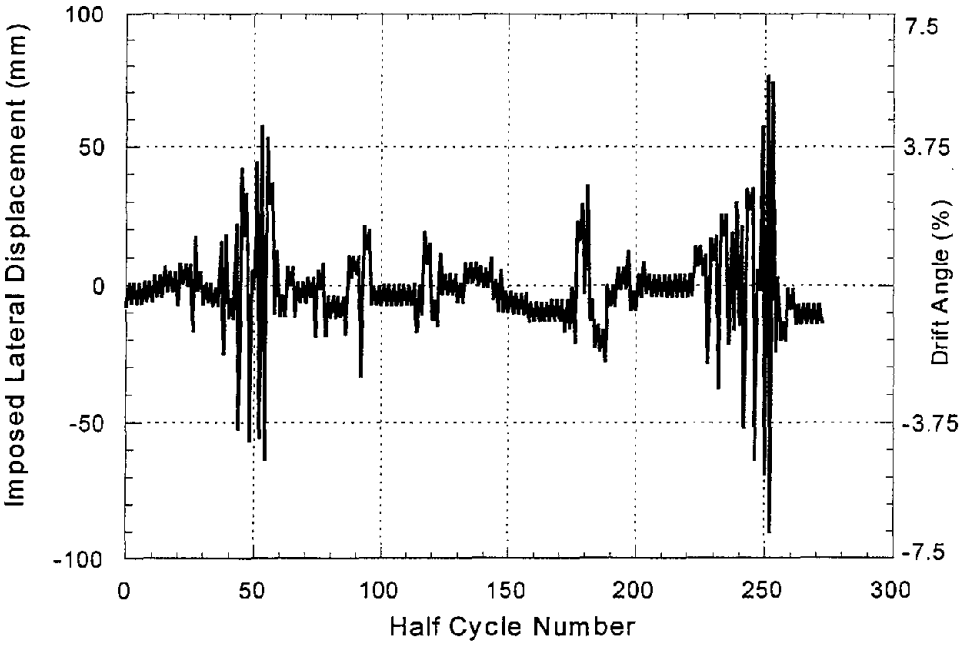

FIGURE 5-14 Displacement History Applied to Column A9

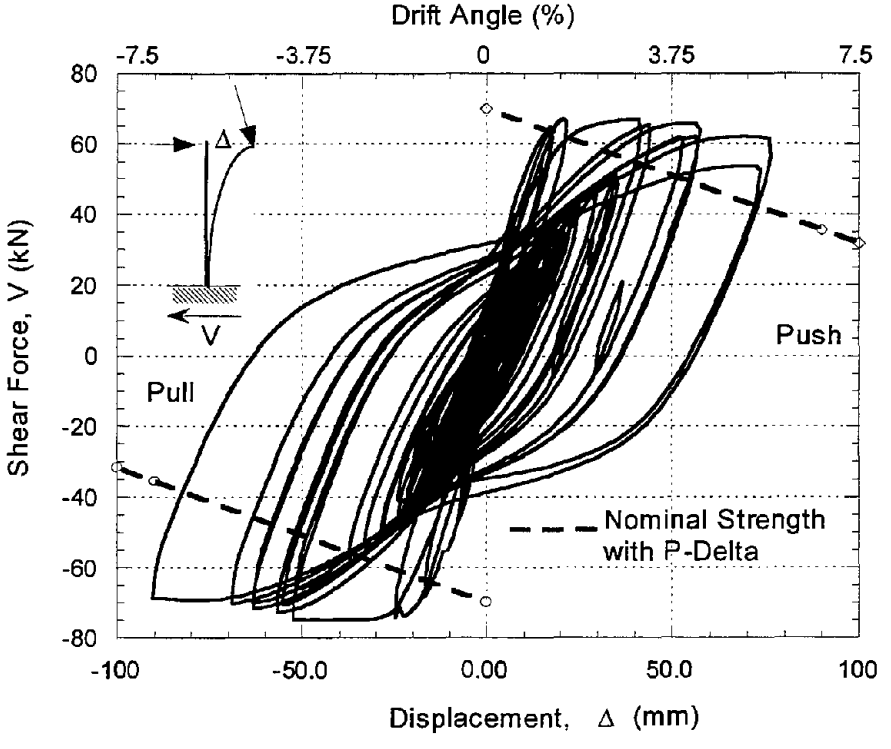

FIGURE 5-15 Base Shear vs. Displacement Response of Column A9

The entire displacement history applied to specimen A10 is displayed in Figure 5-18. The hysteresis loops showing base shear vs. lateral displacement response of the bridge column is plotted in Figure 5-19. A summary of test observations and general damage behavior during testing of specimen A10 is presented in Table 5-5.

TABLE 5-5 Summary of Observations During Testing of Specimen A10

LOADING TYPE:	Simulated Seismic (Random) Loading.
Concrete Strength:	27 MPa
LOADING AND DISPLACEMENT VALUES OF INTEREST:	
Axial Load :	200 kN
Cracking Load:	18 kN
Cracking Displacement:	5.5 mm
Yield Load:	58 kN
Yield Displacement:	17 mm
Maximum Lateral Load:	74 kN
Maximum Lateral Displacement:	91.2 mm
Failure Mode:	Spiral Ruptured on the Left Side

DAMAGE OBSERVATIONS:

Half-Cycle No.	Notes
12	First Cracking
30	Spalling
194	Significant Spalling
260	Spiral Failed on the Left Side of Column

5.3.5 Specimen A11

A relatively recent set of unscaled earthquakes were used to simulate the displacement history for specimens A11 and A12. The only exception to the set was the 1952 Kern County (Taft) record. Two recorded accelerograms from the 1994 Northridge earthquake and the SCT record from the 1985 Mexico City earthquake composed the remainder of the input motions. The combined accelerogram record and the corresponding spectra of the unique multiple motion was shown previously in Figure 5-3.

First cracking was observed on the right side of the specimen at half-cycle 27 of the first earthquake. Minor spalling was also observed. First cracking on the opposite side occurred in the very next half-cycle. The drift at this point was over 2.5%. By half-cycle #38, concrete spalling had extended to indicate extension of the plastic hinge zone and cracks had propagated 75 – 100 mm above the hinge zone. The maximum crack width was about 2 mm which increased to almost 4 mm following the 21st complete cycle.

FIGURE 5-16 State of Specimen A10 at Half-Cycle # 121

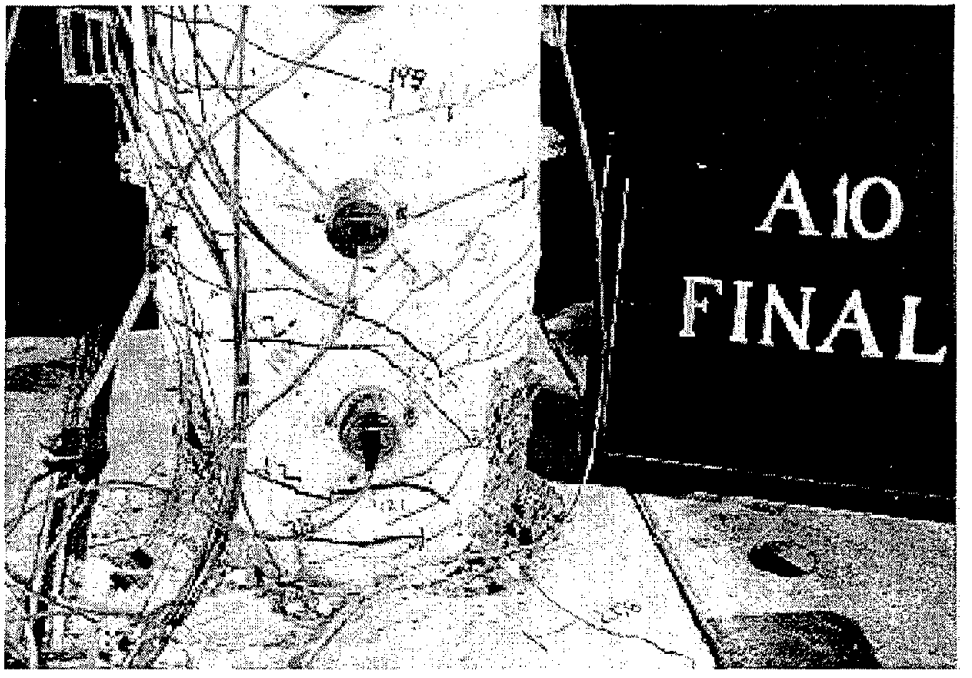

FIGURE 5-17 Final Damaged State of Specimen A10

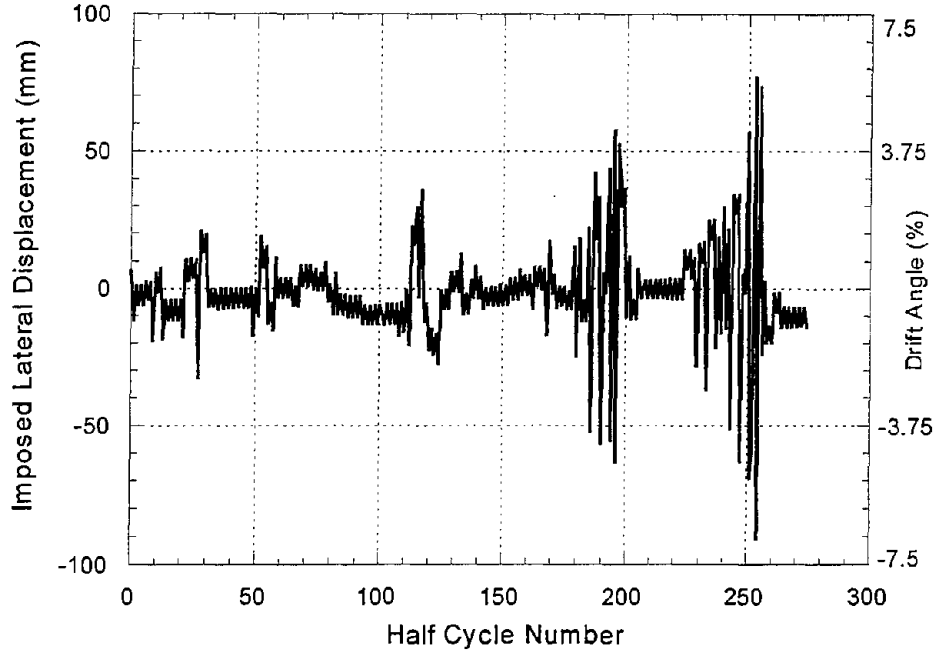

FIGURE 5-18 Displacement History Applied to Column A10

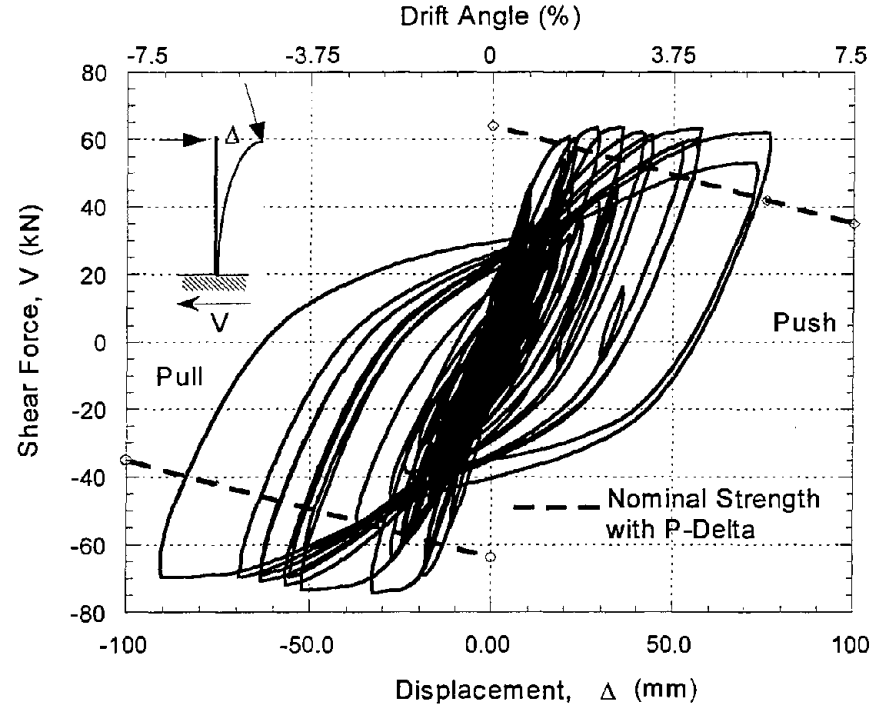

FIGURE 5-19 Shear vs. Displacement Response of Column A10

The next two earthquakes which represented potential aftershocks did not cause any further damage to the column. The final earthquake imposed several large displacement cycles in excess of 3.5% combined with a single cycle with a maximum drift of almost 7%. Buckling of the longitudinal bars was observed at half cycle # 252 on both sides of the specimen which forced spiral to start necking in the center of the plastic hinge zone. Two spirals failed in consecutive half cycles (#270 and 271).

The plastic hinge length was about 200 mm in length at the instant of failure. The specimen was further loaded for the remainder of the earthquake induced displacement until fracture of a longitudinal bar was recorded at half-cycle # 275.

Figure 5-20 displays the state of damage at the end of half-cycle # 139 at which point significant spalling of the concrete cover in the plastic zone had occurred and the spiral reinforcement was exposed. Figure 5-21 shows the final damaged state of the specimen.

The entire displacement history applied to specimen A11 is shown in Figure 5-22. The recorded shear force vs. lateral displacement behavior of the bridge column is plotted in Figure 5-23. A summary of the observations during testing and general damage of specimen A11 is presented in Table 5-6.

TABLE 5-6 Summary of Observations During Testing of Specimen A11

LOADING TYPE:	Simulated Seismic (Random) Loading.
Concrete Strength:	27 MPa
LOADING AND DISPLACEMENT VALUES OF INTEREST:	
Axial Load :	200 kN
Cracking Load:	18 kN
Cracking Displacement:	6 mm
Yield Load:	65 kN
Yield displacement:	18 mm
Maximum Lateral Load:	69 kN
Maximum Lateral Displacement:	103 mm
Failure Mode:	Spiral Rupture

DAMAGE OBSERVATIONS:

Cycle No.	Notes
27	First Cracking
38	Spalling
252	Significant Spalling, Some bar buckling, and necking of spirals
270-271	Two Spiral Failed on the Right Side
275	Fracture of longitudinal bar

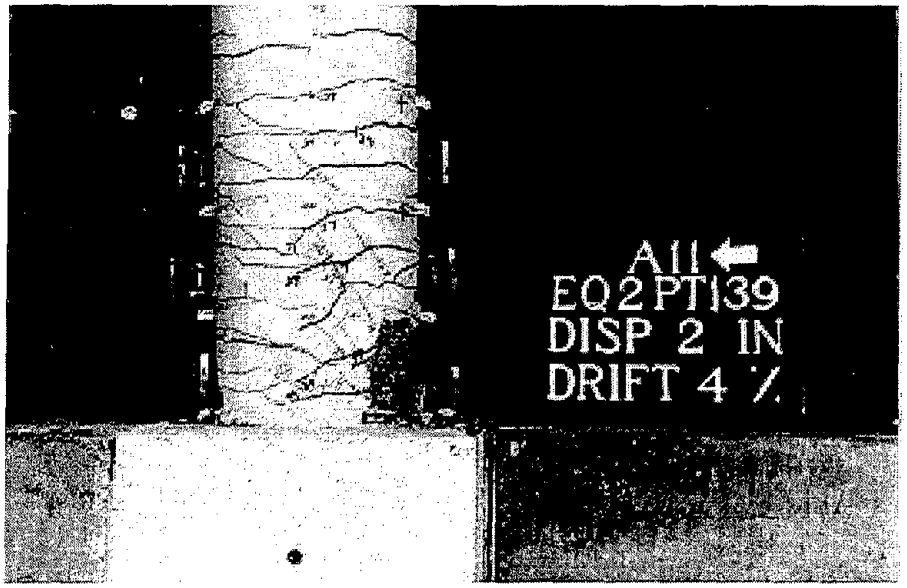

FIGURE 5-20 Specimen A11 at Half-Cycle # 139

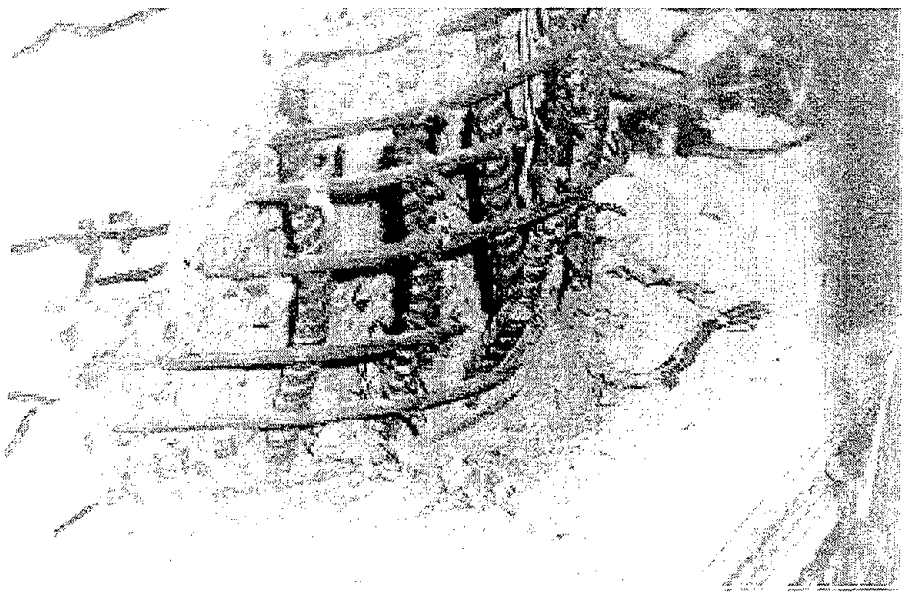

FIGURE 5-21 Final Damaged State of Specimen A11

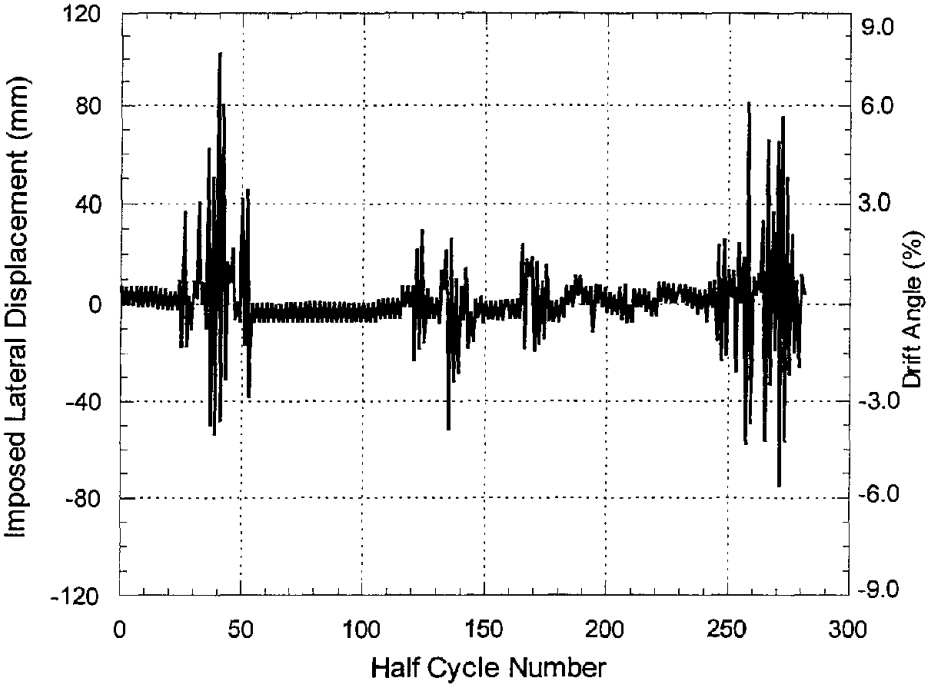

FIGURE 5-22 Displacement History Applied to Column A11

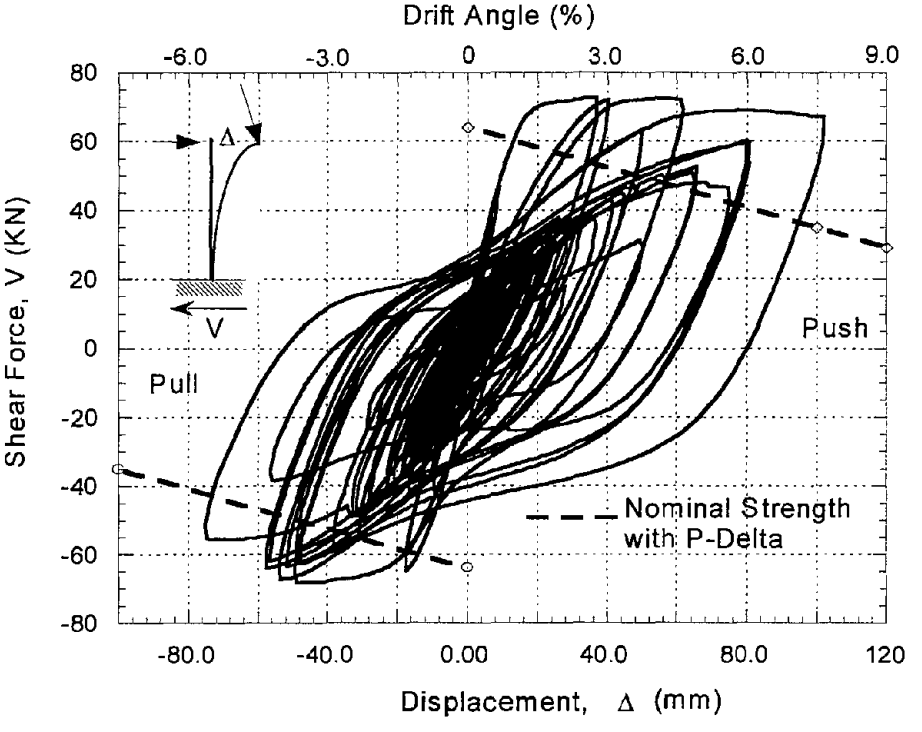

FIGURE 5-23 Shear vs. Displacement Response of Column A11

5.3.6 Specimen A12

Specimen A11 failed mid-way through earthquake 4. However, the largest amplitudes were imposed by earthquake #1. For specimen A12, the displacement cycles corresponding to earthquake #4 up to failure of the column were first applied, followed by the two minor earthquakes, followed by the original earthquake #1, and then followed by the remainder of earthquake #4. Hence the largest amplitudes were reserved for the final cycles. Since all the previous specimens failed in confinement, it was of interest to see if longitudinal bar fracture could be induced through an alternate sequence of cycling.

First crack occurred on the right side of the specimen at half-cycle #72 accompanied by minor spalling. The specimen had experienced a couple of cycles at 2% lateral drift at this stage. Cracking on the opposite face of the column did not occur until half-cycle #83 when the drift in one cycle exceeded 3.5%. By the end of the first minor earthquake, the crack widths were no larger than 2 mm.

The second earthquake, which did not contain any large amplitude cycles, did no further damage to the column. At the onset of the large amplitudes due to earthquake 3, corresponding to half-cycles 205 and 206, significant spalling (Figure 5-24) was observed on both sides of the specimen. At this time, the column had undergone one large inelastic excursion with a lateral drift of almost 6%. The average crack width was 2-3 mm. Buckling of the longitudinal bars was first noticed at half-cycle # 254 leading to a kink (or necking) in the spirals.

FIGURE 5-24 Specimen A12 at Half-Cycle 206

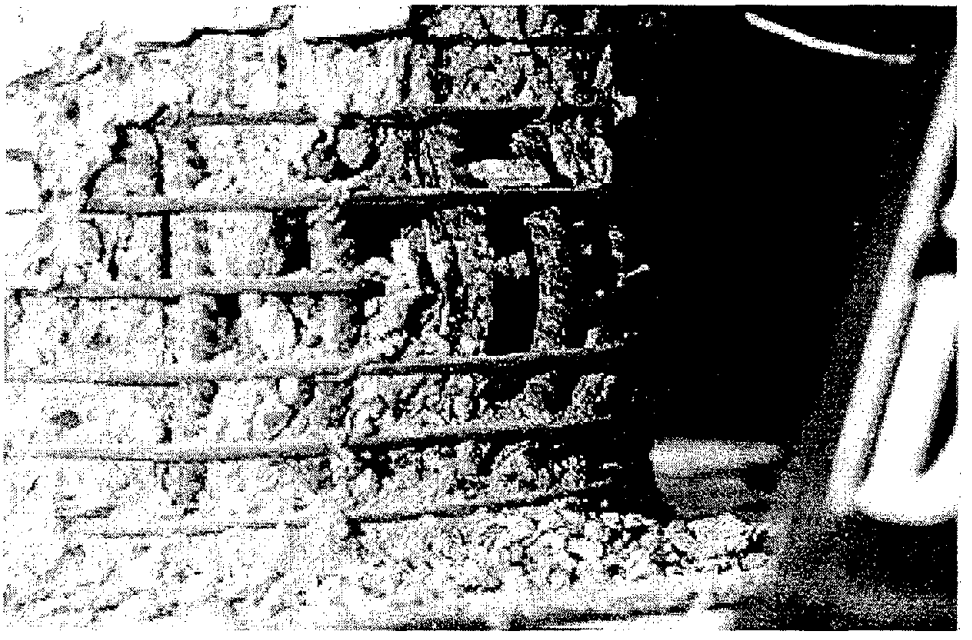

FIGURE 5-25 Final Damaged State of Specimen A12

First signs of failure were recorded during the fourth earthquake at half-cycle # 255 when one of the spirals on the right side ruptured. The maximum lateral drift at this cycle exceeded 7% lateral drift. It was decided to continue loading column A12 with the rest of the displacement history. At half-cycle # 276, one of the longitudinal bars fractured on the east (left) side of the specimen. The final damaged state of the specimen is shown in Figure 5-25.

The displacement history imposed on the specimen is shown in Figure 5-26. The corresponding force vs. lateral displacement response of the column is presented in Figure 5-27. Table 5-7 summarizes observations during testing.

TABLE 5-7 Summary of Observations During Testing of Specimen A12

LOADING TYPE:	Simulated Seismic (Random) Loading.
Concrete Strength:	27 MPa

LOADING AND DISPLACEMENT VALUES OF INTEREST:

Axial Load :	200 kN
Cracking Load:	18.5 kN
Cracking Displacement:	6 mm
Yield Load:	64 kN
Yield displacement:	13 mm
Maximum Lateral Load:	72 kN
Maximum Lateral Displacement:	103 mm
Failure Mode:	Spiral Rupture

DAMAGE OBSERVATIONS:

Half-Cycle No.	Notes
22	First Cracking
83	Spalling
205-206	Significant Spalling; Buckling of long. Bars and initiation of spiral necking
255	Spiral Failed on the Right Side of Column

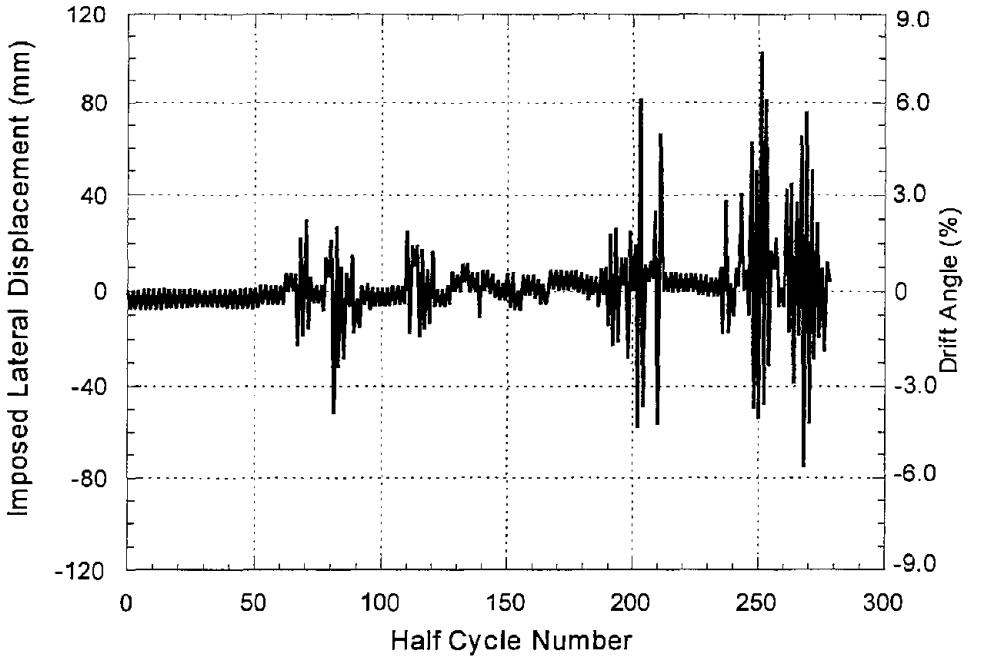

FIGURE 5-26 Displacement History Applied to Column A12

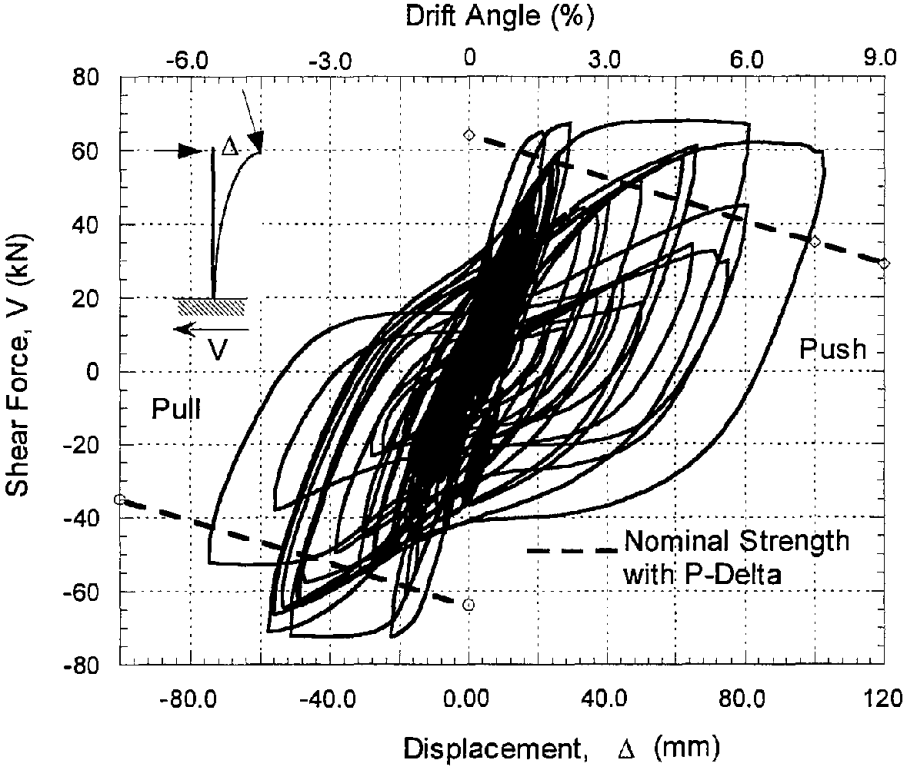

FIGURE 5-27 Base Shear vs. Lateral Displacement Response of Column A12

6.0 CUMULATIVE DAMAGE MODELING: EVALUATION OF EXPERIMENTAL RESULTS

The bridge column specimens tested in the experimental program, and presented in Sections 4 and 5 of this report, will be examined in this section from the perspective of damage modeling. Since a number of damage models have been proposed by other researchers in the past, it was considered beneficial to compare the relative performance of selected models by applying them to the observed response and damage of specimens tested in this research.

The next sub-section will provide a brief overview of typical fatigue-based damage models proposed for use in seismic structural analysis. The models selected for systematic evaluation will then be discussed. Finally, the performance of each of the selected models against data generated from the present experimental testing will be presented.

6.1 Fatigue-Based Damage Models

A review of the literature reveals that there are essentially five approaches to damage modeling: estimates based on measures of deformation and/or ductility; models based on the degradation of a selected structural parameter (typically stiffness); models developed from considerations of energy-dissipation demand and capacity; hybrid formulations combining some aspects of the aforementioned parameters; and more complex theories based on concepts derived from fatigue models. Comprehensive reviews of damage modeling techniques can be found in Powell and Allahabadi (1988) and Williams and Sexsmith (1994).

Since seismic loads induce several inelastic cycles at relatively large ductilities, the concept of using low-cycle fatigue theories to model damage is logical. Though high-cycle fatigue of metals and concrete have been evaluated in the past, few have attempted to extend these concepts to evaluating seismically induced fatigue damage. The formulation of Chung et al. (1987) combines Miner's rule (Miner, 1945) with a failure criteria:

$$D = \sum_i \left[w_i^+ \frac{n_i^+}{n_{f,i}^+} + w_i^- \frac{n_i^-}{n_{f,i}^-} \right] \qquad (6\text{-}1)$$

In the above expression, where both positive and negative cycles are treated separately, w_i is a weighting factor, n_i is the number of cycles at a given amplitude, and $n_{f,i}$ is the number of cycles to failure at the same amplitude. The similarity of this approach to the well-known Miner's hypothesis is evident.

Jeong and Iwan (1988) use a more straight-forward extension of Miner's rule by combining it with another well-known law postulated by Coffin-Manson:

$$D = \sum_i \frac{n_i \mu_i}{c} \qquad (6\text{-}2)$$

where $c = n_f \mu$ and n_f is the number of cycles to failure at a specified ductility μ.

Other approaches to modeling fatigue failure have also been developed. The most practical of these is a mechanics-based derivation by Mander and Cheng (1995). They express local section curvature at the plastic hinge region directly in terms of strain in the rebar:

$$\phi_p D = \frac{0.113}{1-2d/D} N_f^{-0.5} \tag{6-3}$$

The above expression is derived from the plastic strain vs. fatigue life relationship obtained from actual testing of steel reinforcing bars (Mander et al., 1994) and the relationship between curvature and strain in a reinforced concrete circular cross-section assuming a linear strain profile. In Equation (6-3), ϕ_p is the plastic curvature, D is the overall column diameter, d is the depth from the outermost concrete fiber to the center of reinforcement, and N_f is the number of cycles to the appearance of the first fatigue crack in steel. A variation of this representation is utilized in this study.

It must be remembered though that using fatigue theories presupposes a flexural fatigue failure mode. Other potential failure modes resulting from the combined effects of axial force, shear and confinement are not incorporated in these models.

6.2 Damage vs. Performance

The ability to predict damage in a structural member does not necessarily reflect the success of a damage model. It is the ability to calibrate a model such that it can be used by a practicing engineer to assess structural integrity following a seismic event that ultimately determines the effectiveness of damage modeling.

Structural engineers in zones of high seismic risk have been faced with the constant challenge of having to associate serviceability limit states with observed visual damage to structures following an earthquake. The Applied Technology Council (ATC) report (ATC, 1985) on *Earthquake Damage Evaluation* provided engineers with damage categories for estimating loss assessment. A more recent ATC effort following the Northridge earthquake introduces the notion of damage states that engineers can use more readily in assessing structural damage from essentially visual observations. The proposed classification is shown in Table 6-1. This classification provides an important guideline that can be used in damage calibration studies. The present study will attempt to correlate observed damage during testing to computed damage values using different models using the above guidelines.

6.3 Models Evaluated in this Study

Four independent models characterizing different damage measures were selected for detailed evaluation in this study. The purpose of this evaluation is to identify the merits and drawbacks of different models so that future work on damage model development may utilize these findings.

TABLE 6-1 Damage Categories Proposed in ATC-38

Damage State	Descriptor	Description
None	N	No visible damage, either cosmetic or structural.
Insignificant	I	Damage requires no more than cosmetic repair. No structural repairs necessary.
Moderate	M	Repairable structural damage has occurred. The existing elements can be repaired essentially in place, without substantial demolition or replacement of elements.
Heavy	H	Damage is so extensive that repair of elements is either not feasible or requires major demolition or replacement.

The first model selected for evaluation is a modified form of the system softening index. The change in structural stiffness is associated with system degradation which translates into a lengthening of the fundamental period. An additional advantage of this model is the fact that it can be monitored in actual structures without much difficulty. In the present study, the following normalized expression is used to quantify damage:

$$D = \frac{k_m - k_o}{k_f - k_o} \tag{6-4}$$

With reference to Figure 6-1, k_m is the stiffness of the structure at the maximum induced displacement, k_f is the pre-established stiffness at failure of the system (typically under monotonic loads), and k_o is the initial stiffness prior to loading.

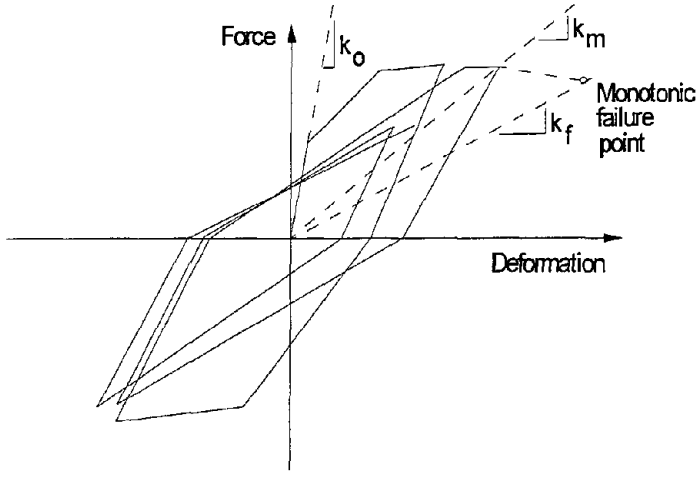

FIGURE 6-1 Parameters Used in Softening Index

The second model investigated is the Kratzig model (Kratzig and Meskouris, 1987), since it incorporates only energy terms in its formulation. The terminology used to define this model is illustrated in Figure 6-2. A primary half cycle (PHC) is the energy contained in the half cycle at the maximum deformation point. Additional cycles with displacement amplitudes less than the peak deformation are accumulated as follower half cycles (FHC). Positive and negative deformations are treated separately. Accumulated damage for the positive portions of the response is defined as:

$$D^{+} = \frac{\sum E_{p,i}^{+} + \sum E_{i}^{+}}{E_{f}^{i} + \sum E_{i}^{+}} \tag{6-5}$$

where E_{pi} is the energy in a PHC, E_i is the energy in an FHC and E_f is the energy absorbed in a monotonic test to failure (area enclosed by OABCF in Figure 6-2). A similar expression is computed for negative deformations, and the two quantities are normalized as follows:

$$D = D^{+} + D^{-} - D^{+}D^{-} \tag{6-6}$$

The inclusion of the follower cycles in the numerator and denominator suggest that their contribution to damage is small, or less significant than deformations that extend the response envelope.

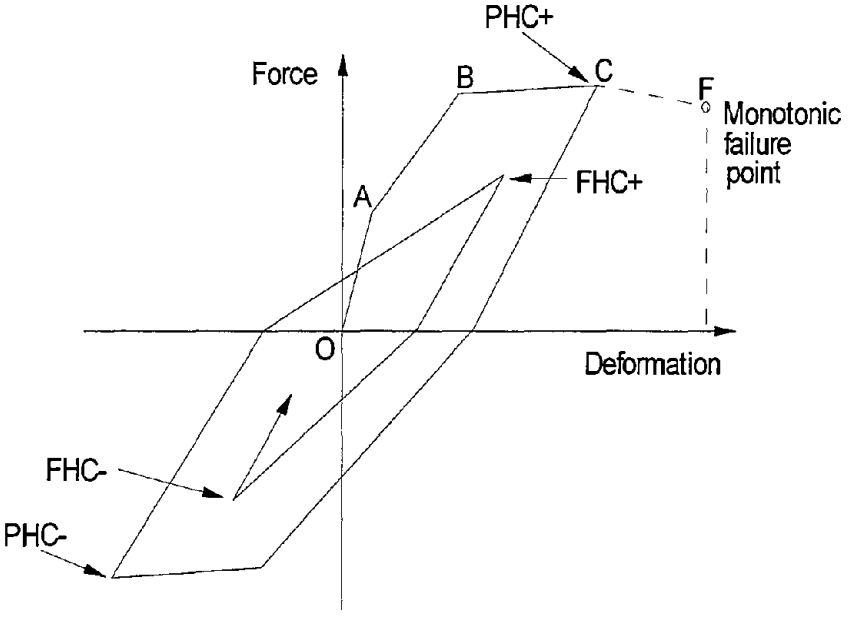

FIGURE 6-2 Parameters Used in Kratzig Damage Model

The next model considered in this study is the Park-Ang model (park and Ang, 1985). This model represents a hybrid model, and was included in the evaluation partly because of its ease in implementation and partly because it is one of the most widely used damage models today. The model is used in its original form as follows:

$$D = \frac{\delta_m}{\delta_f} + \beta \frac{E_T}{F_y \delta_f} \tag{6-7}$$

The constant β was identified directly from the standard cyclic test conducted on Specimen A-2.

The fourth and final model considered for evaluation was derived from principles of low-cycle fatigue. As pointed out earlier, the identification of the failure mode is critical prior to using a fatigue model. Since the bridge columns tested in this study were essentially flexural columns with well detailed plastic hinge zones, only two important failure modes had to be considered: confinement failure or longitudinal rebar fracture from low-cycle fatigue. Modeling confinement failure is somewhat more complex. Hence only the fatigue behavior of the longitudinal steel was monitored, as described below.

The derivation shown below is a variation of the procedure developed by Mander and Cheng (1995). The fatigue behavior of the longitudinal steel under reversed cyclic loading is formulated in terms of the Coffin (1954) - Manson (1953) equation:

$$\varepsilon_p = \varepsilon_f' (2N_f)^c \tag{6-8}$$

where: ε_p = plastic strain amplitude

ε_f' = a material constant to be determined from fatigue testing

$2N_f$ = Number of complete cycles to failure

An experimental fit to this expression was obtained by Mander et al. (1994):

$$\varepsilon_p = 0.08 (2N_f)^{-0.5} \tag{6-9}$$

A similar expression using total strain instead of plastic strain was also developed:

$$\varepsilon_t = 0.08 (2N_f)^{-0.33} \tag{6-10}$$

A relationship between strain and curvature is possible, assuming the plane-section theory, as displayed in Figure 6-3.

$$\varepsilon_p = \Phi_p \bar{d} / 2 \tag{6-11}$$

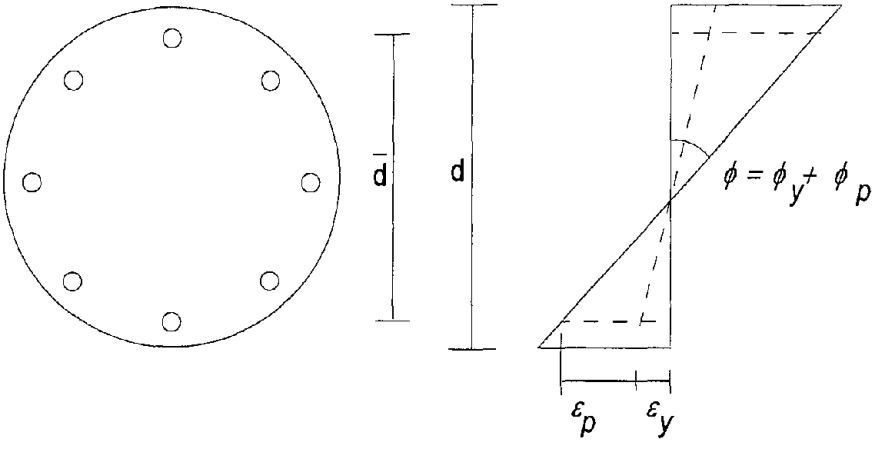

FIGURE 6-3 Curvature-Strain Relationship for Plane Sections

If the plastic hinge length is defined as l_p, an expression for the plastic strain in terms of plastic curvature (or rotation) can be established (Priestley and Paulay, 1992) assuming that the plastic rotation takes place about the center of the plastic hinge:

$$\Phi_p = \frac{\theta_p}{l_p} = \frac{\Delta_p / (L - 0.5 l_p)}{l_p} \tag{6-12}$$

which upon substitution into Equation (6-11) can be used directly in Equation (6-9) to define the number of cycles to failure for a given plastic strain or a given plastic deformation. Cumulative damage is then defined as:

$$D = \sum \frac{1}{2N_f} \tag{6-13}$$

The following additional notations were used in the above expressions:

l_p = plastic hinge length
$\bar{d}$ = distance between centers of longitudinal bars
θ_p = plastic rotation
Φ_p = plastic curvature (difference between total and yield curvature)
L = specimen (member) length

In the present study, the fatigue-based damage index was derived in terms of plastic strain. Since random displacement cycles were used in the second phase of testing, the model was re-written

in terms of half cycles since the positive and negative peaks in a given cycle were not of the same amplitude.

6.4 Damage Analysis of Tested Specimens

The control parameters required in the application of the different damage models selected for evaluation were initially identified from the monotonic test specimen and then adjusted to match the average response of specimens A2 through A6. The variation from the mean values for any of the specimens did not exceed 10%.

The following fixed parameters were used throughout the evaluation:

Yield force:	65 kN
Yield displacement:	18 mm
Ultimate displacement:	155 mm
Initial Stiffness of column:	10.5 kN/mm

The computed damage to specimen A2 using the different models described in Section 6.2 is shown in Figure 6-4. Of all the models, the Softening Index and the Kratzig model show severe damage fairly early in the response. The fatigue model shows little or no damage through the first ten cycles where displacement ductilities are below two. The Park-Ang model shows a gradual progression of damage throughout the load history with increasing accumulation of damage at each increase in displacement level. The fatigue model suggests rapid deterioration of the specimen towards the end of the loading while the damage appears to be in the repairable range after 24 cycles. The actual observed damage state was probably between the predictions of the fatigue model and the Park-Ang model. In summary, for this specimen, the Park-Ang model provided a very good measure of damage at different limit states.

Specimen A3 was subjected to 150 cycles at a lateral drift of about 2%. As described earlier in Section 4, these 150 cycles produced only reparable damage to the column. The application of the damage models to this specimen is displayed in Figure 6-5. All non-fatigue based models, including the Park-Ang model fail to predict accurately the damaged state of the component at the end of the testing. The Kratzig model and the Softening index, as before, show significant damage accumulations early in the response which is inconsistent with observed behavior. The fatigue model performed the best with predicted damage states correlating to observed damage.

The next specimen, A4, was subjected to a much larger drift amplitude. Failure of the specimen was recorded in less than 30 cycles. The Park-Ang model seems to perform better when the displacement amplitudes are significantly larger than the yield displacement. The Kratzig model and the damage represented by the Softening Index do not span a reasonable range of limit states due to the fact that severe damage is predicted very early in the response.

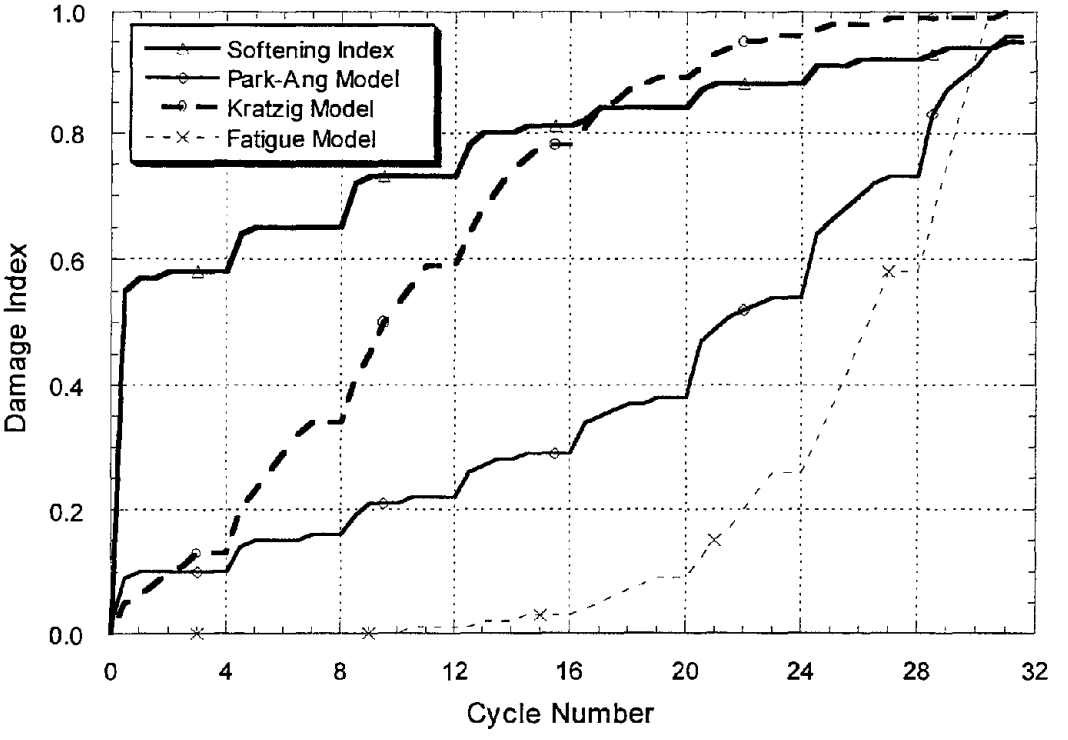

FIGURE 6-4 Comparative Evaluation of Progressive Damage for Specimen A2

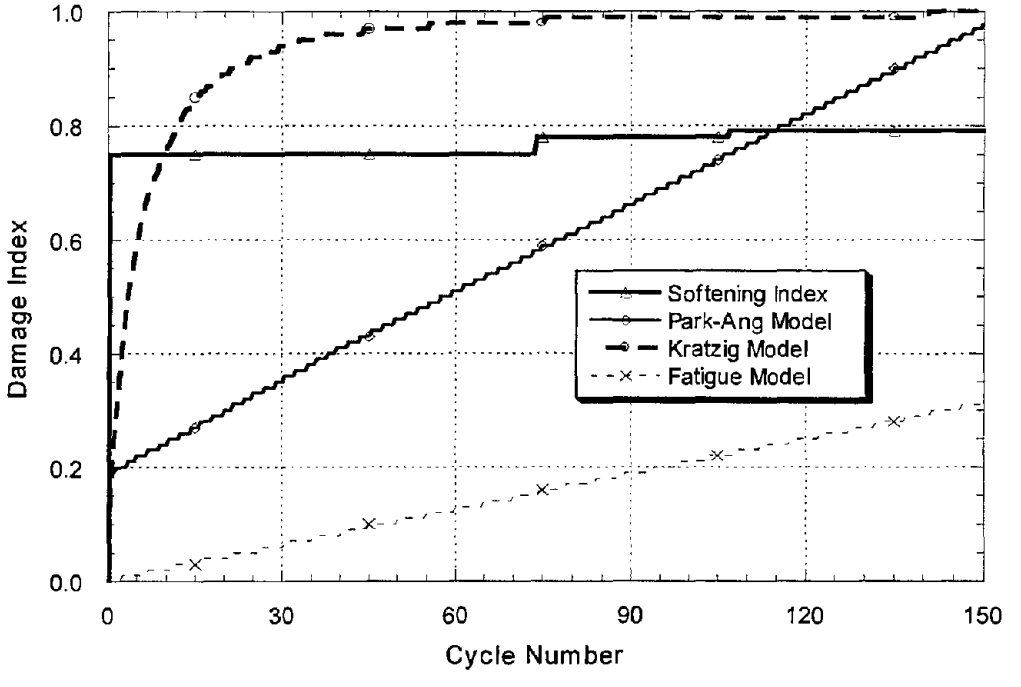

FIGURE 6-5 Comparative Evaluation of Progressive Damage for Specimen A3

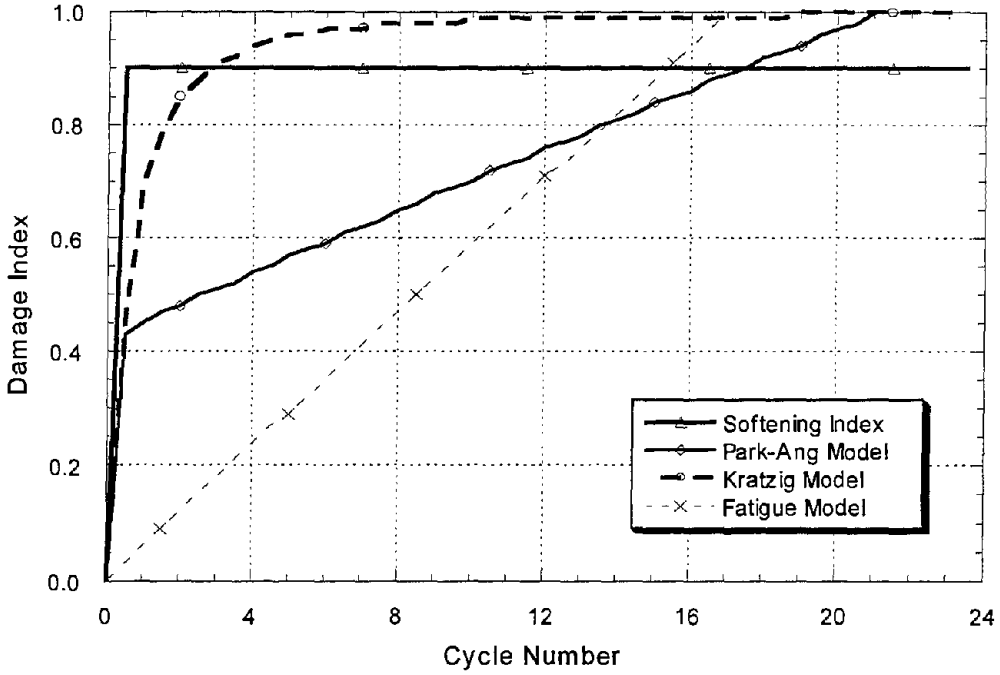

FIGURE 6-6 Comparative Evaluation of Progressive Damage for Specimen A4

The fatigue model over predicts damage with failure reported at the end of the 17th cycle. Figure 6-6 displays the computed damage history for each model.

Figure 6-7 presents the cumulative damage for specimen A-5. The Park-Ang damage model reaches an index of 0.5 with the first cycle representing primarily the deformation damage at a drift of 5.5%. Since the fatigue model is based on cycles to failure using Miner's rule, and is evaluated at the end of each cycle, the damage progression is essentially linear.

The last specimen subjected to constant amplitude loading failed at the end of the 4th cycle. The imposed drift was slightly larger than 7.0%. The severe damage predicted by the non-fatigue models in the very first cycle indicate their inability to deal with low-cycle fatigue damage. The fatigue model, on the other hand, has been fairly consistent in their prediction levels. Failure in this specimen was indeed by longitudinal bar fracture. Results of the evaluation are shown in Figure 6-8.

Specimens A7 through A12 were subjected to random cyclic reversals. Figure 6-9 shows the progression of damage for Specimen A-7 which was subjected to a major earthquake followed by two smaller events (aftershocks or minor tremors) and finally another severe event which resulted in failure by rupture of the confining spirals. All of the damage models show a significant increase in damage at each of the imposed large amplitude reversals. The Softening Index, the energy-based Kratzig model and the Park model indicate severe damage following the single peak cycle at 6% drift during the 1st earthquake. The fatigue model shows little evidence of such damage. While it may be stated that visual observations support the non-fatigue models, only the Park model picks up additional damage in the fourth and final earthquake.

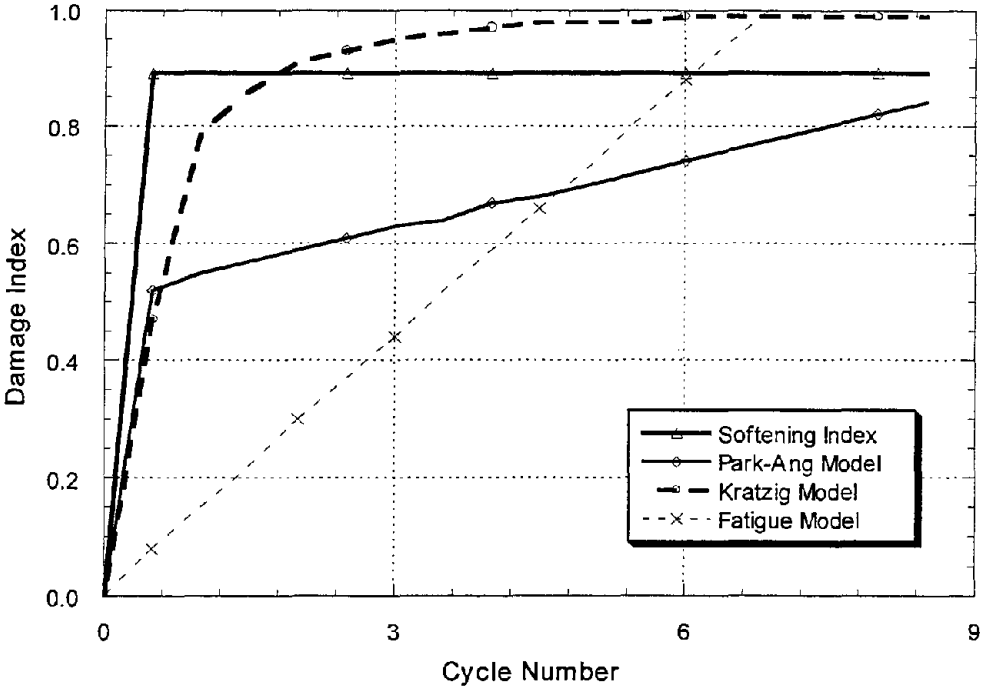

FIGURE 6-7 Comparative Evaluation of Progressive Damage for Specimen A5

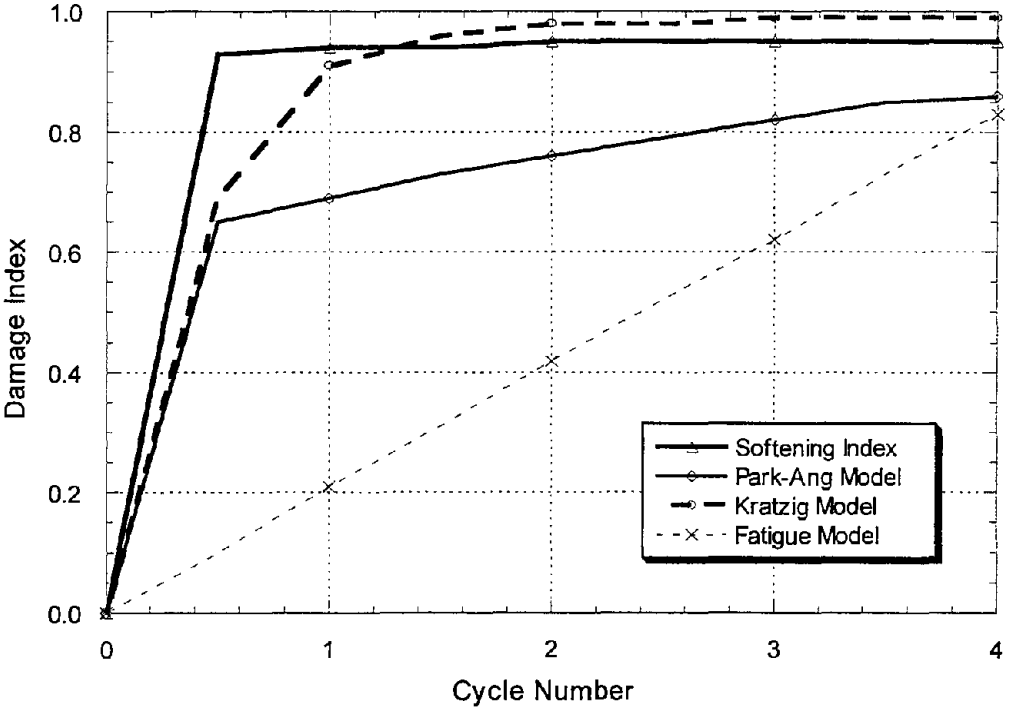

FIGURE 6-8 Comparative Evaluation of Progressive Damage for Specimen A6

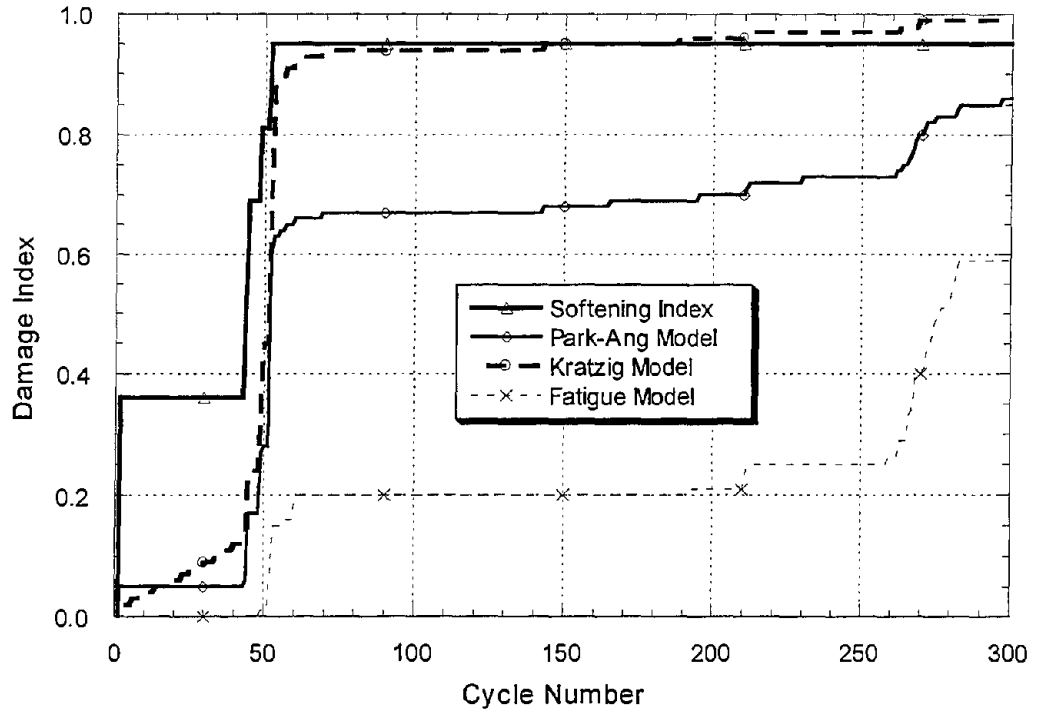

FIGURE 6-9 Comparative Evaluation of Progressive Damage for Specimen A7

Specimen A-8 was subjected to essentially the same total history but the sequence of events was changed. Here two severe events followed two minor ones. The results of the damage model application to the recorded response is presented in Figure 6-10. Interestingly, this specimen failed at approximately the same cycle of displacement indicating no effect of load path.

All the damage models, which do not take into account the effect of load path, show the same final damage state, as expected. But an interesting observation must be noted: the degree of damage from the minor earthquakes is fairly significant for the non-fatigue models which is inconsistent with observed behavior. There seems to be a tendency for such models to accumulate damage at unreasonable rates during low amplitude cycling - this was also observed in the constant amplitude tests where all of the non-fatigue models predicted failure after 150 cycles at 2 % drift.

Specimens A9 and A10 were subjected to a different set of load reversals resulting from a different sequence of events. A9 experienced strong ground shaking representing a severe event followed by two minor earthquakes, a moderate earthquake, and another major event. In the case of Specimen A10, the final event was retained as before but the first four earthquakes were interchanged to produce an entirely different path leading up to the final earthquake. The predicted damage using the different damage models are shown in Figures 6-11 and 6-12.

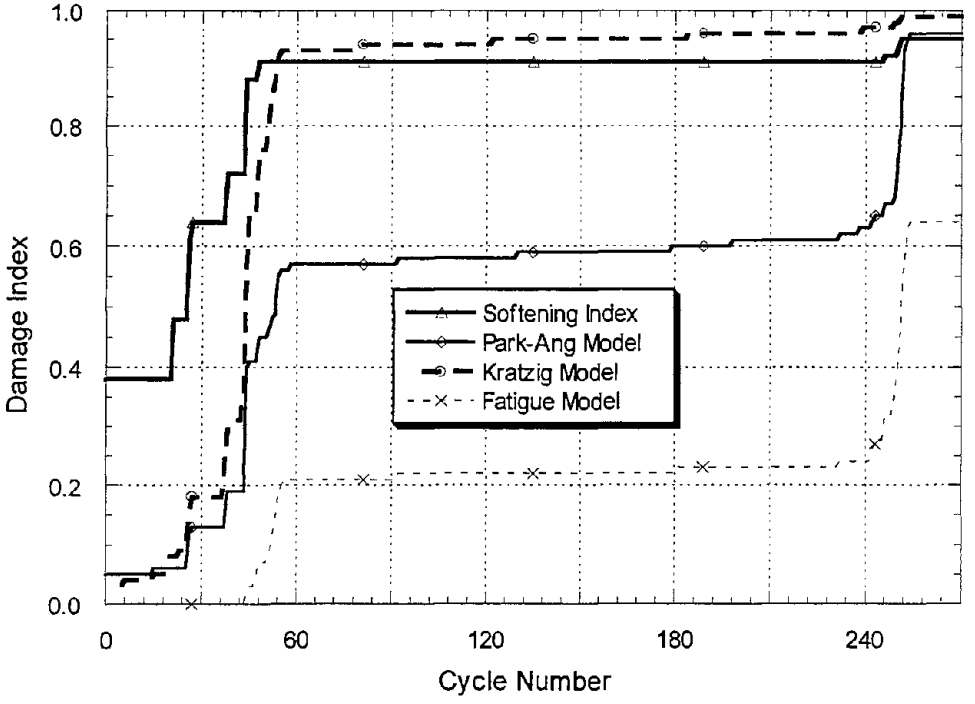

FIGURE 6-10 Comparative Evaluation of Progressive Damage for Specimen A8

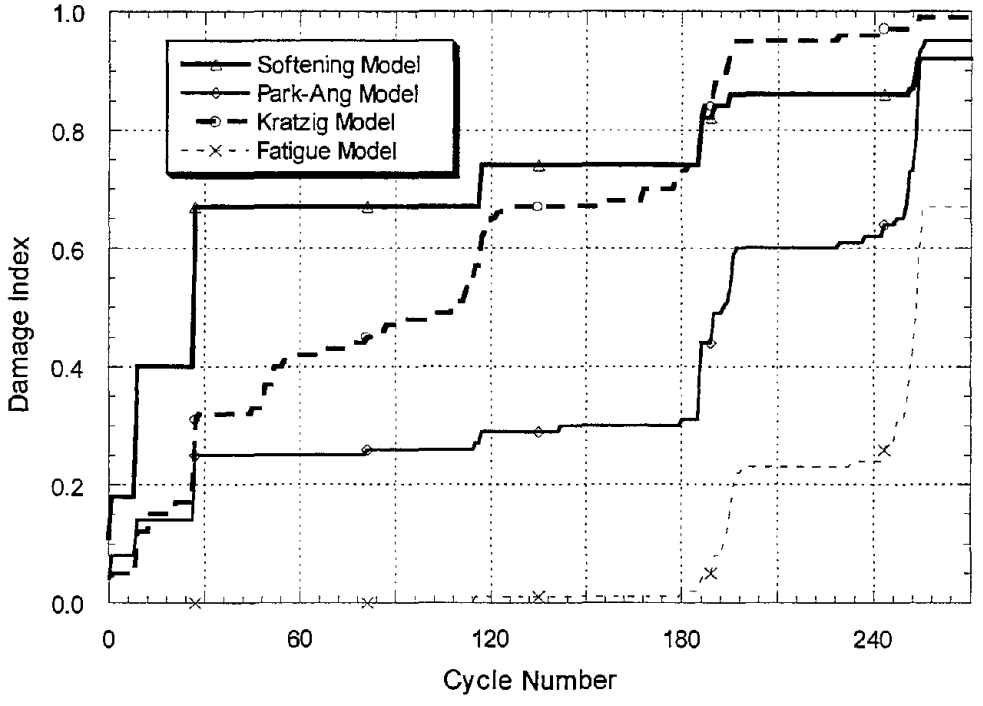

FIGURE 6-11 Comparative Evaluation of Progressive Damage for Specimen A9

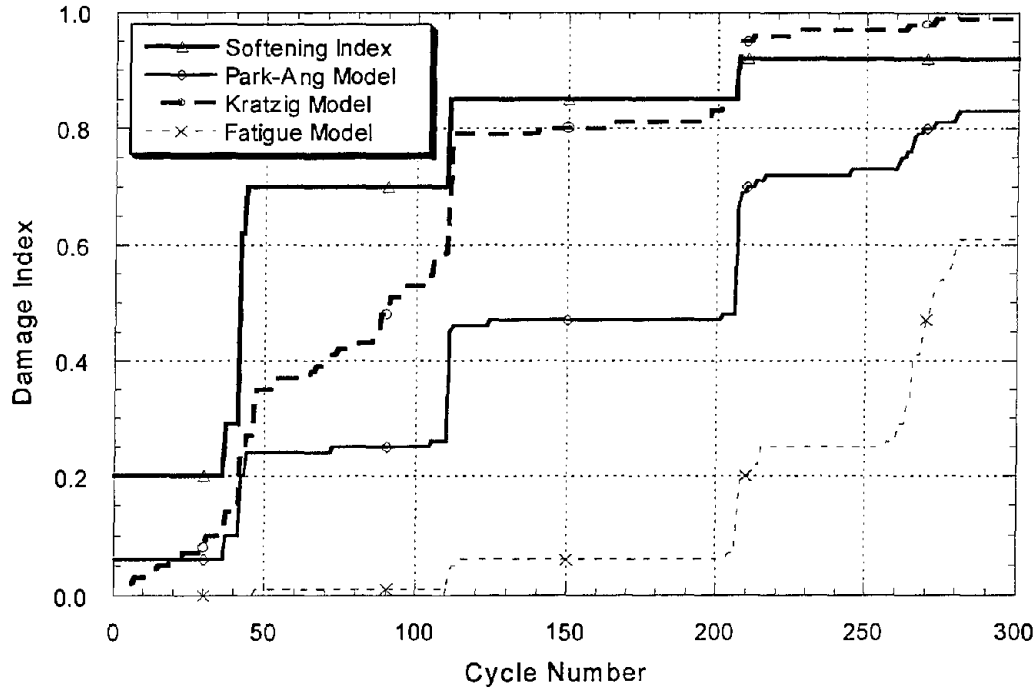

FIGURE 6-12 Comparative Evaluation of Progressive Damage for Specimen A10

As in the case of the previous two specimens, the damage models respond primarily to large displacements. And, as was the case with the constant amplitude cycles, the Kratzig model and the Softening Index predict significant damage very early in the response. Since both specimens failed in confinement, the present fatigue damage model, which essentially monitors fatigue in the longitudinal rebars, did not predict failure.

The final two specimens were subjected to four earthquakes. Two minor events were placed between two significant events. The objective in this series of testing was to induce fatigue failure of the longitudinal bars, hence the events were so selected to produce significantly larger displacement amplitudes. The predicted accumulation of damage is presented in Figures 6-13 and 6-14 for specimens A-11 and A-12, respectively. Failure in the two specimens did not take place at exactly the same cycle, instead the second specimen which sustained relatively smaller amplitudes early in the history survived a few additional inelastic cycles before failure.

6.5 Proposed Fatigue-Based Cumulative Damage Model

In general, it was observed that the fatigue-based damage model under-predicted the final damage state of all column specimens. Since the model used in the study is capable of evaluating damage due to low-cycle fatigue of the main longitudinal reinforcing bars only, and all tested specimens experienced confinement failure prior to low-cycle fatigue failure, this observation is not unexpected.

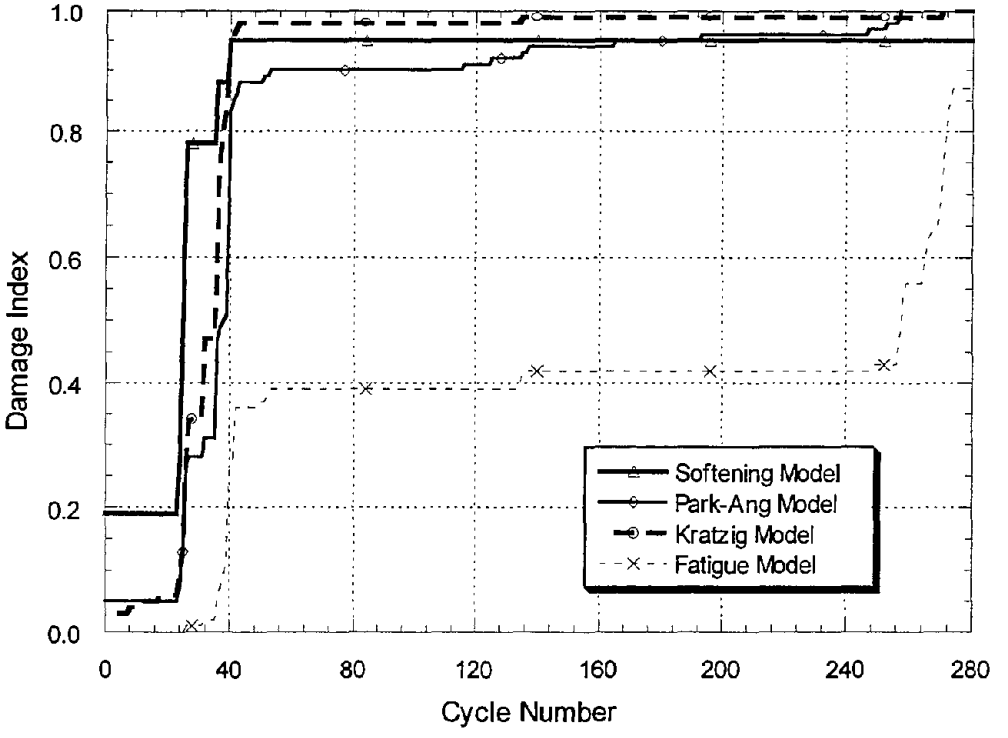

FIGURE 6-13 Comparative Evaluation of Progressive Damage for Specimen A11

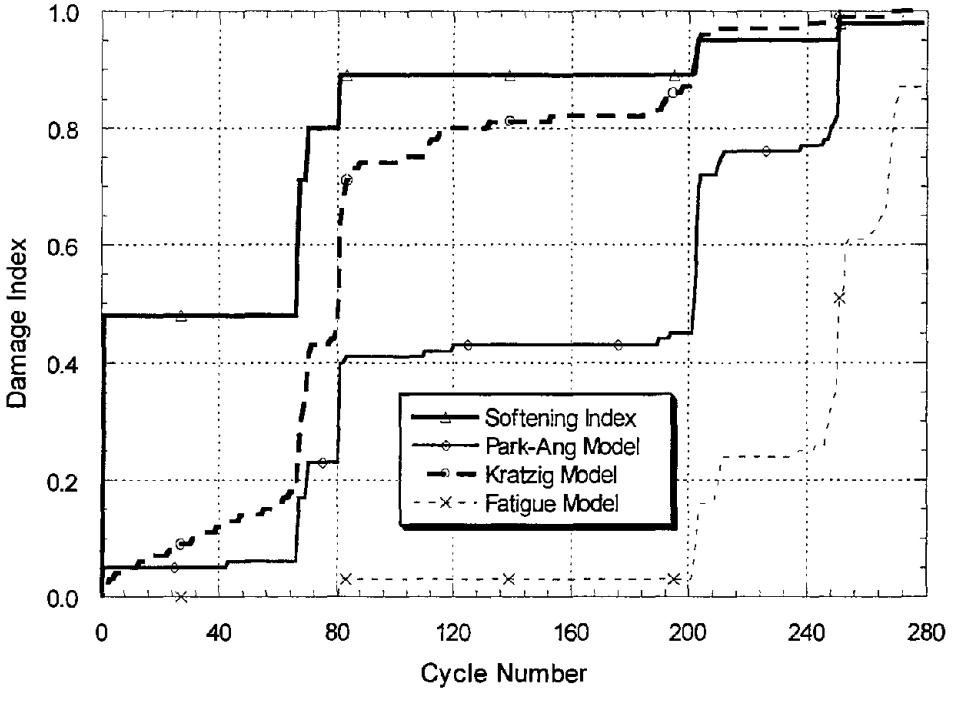

FIGURE 6-14 Comparative Evaluation of Progressive Damage for Specimen A12

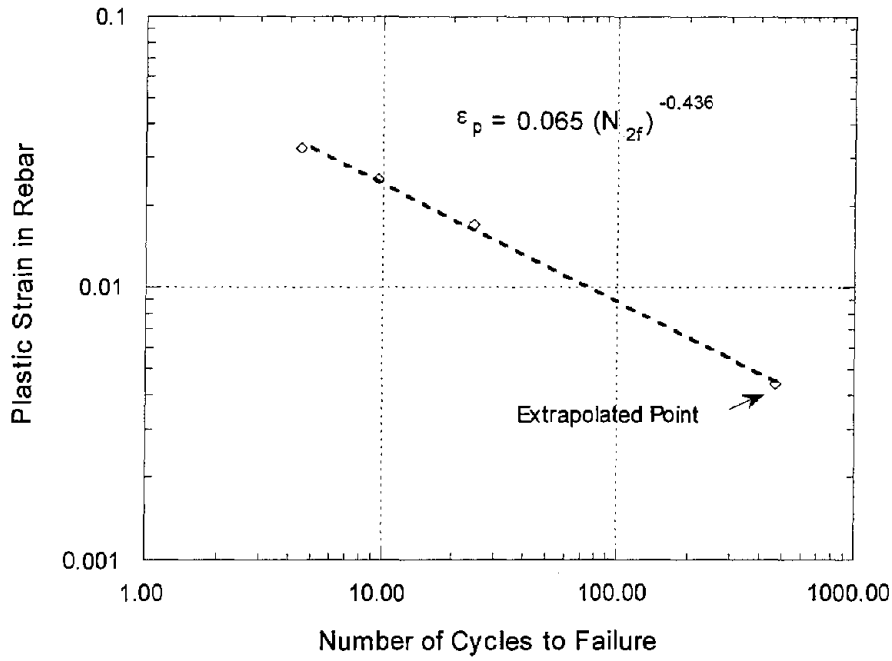

FIGURE 6-15 Coffin-Manson Fatigue Model for Plastic Strain

A modified cumulative fatigue model is now proposed based on experimental fitting of the Coffin-Manson fatigue expression using results from the constant-amplitude testing of columns A3, A4, A5 and A6. The plastic and total strains in the longitudinal rebars were calculated from expressions previously listed in Equations (6-11 and 6-12). Results of the curve-fitting exercise are shown in Figures 6-15 and 6-16. On evaluating the model coefficients of both plastic and total strains vs. the number of cycles to failure, the following expressions are obtained :

$$\varepsilon_p = 0.065(N_{2f})^{-0.436} \tag{6-14}$$

$$\varepsilon_t = 0.060(N_{2f})^{-0.360} \tag{6-15}$$

Note that the number of cycles to failure for specimen A3 was not based on experimental observation since the specimen did not fail after 150 cycles and was eventually subjected to a monotonic load to induce failure. This point on the graph corresponding to this specimen was computed analytically from the above equations. The difference in the constants of the above equations to those obtained by Mander et al. (1994) is the fact that these expressions were derived for the concrete column as a composite section and indirectly accounts for the accumulated damage due to shear, axial stress and loss of confinement.

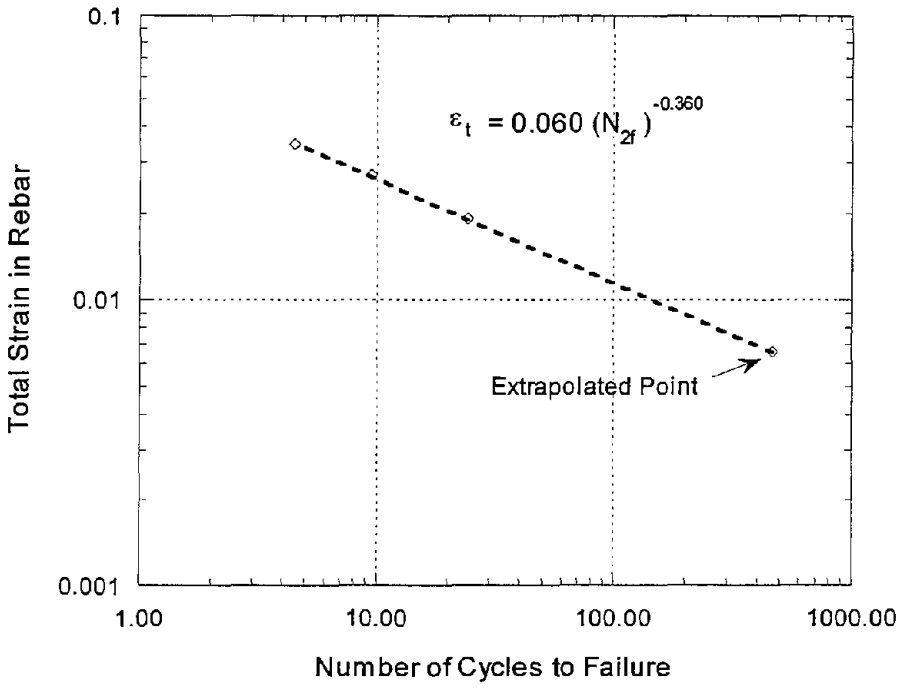

FIGURE 6-16 Coffin-Manson Fatigue Model for Total Strain

Equations (6-14) and (6-15) can be considered as fatigue life expressions for seismically detailed AASHTO (or CALTRANS) flexural columns and may be used to predict damage and reserve capacity. Similar expressions can be derived using lateral drift as a variable. To convert the above equations to a relationship involving lateral drift, Equations (6-11) and (6-12) are used. Values of the plastic hinge length and yield deformation were taken directly from experimental records or observations. The resulting expression for fatigue life of flexural columns as a function of total lateral drift is:

$$Drift\ (\%) = 10.6\ (N_{2f})^{-0.285} \qquad (6\text{-}16)$$

The curve-fit for Equation (6-16) is shown in Figure 6-17. A simple procedure to estimate earthquake damage for a known ground motion is summarized in Section 7.

Finally, Equations (6-14) and (6-15) were used to estimate damage to Specimens A-7 through A-12. Essentially, the damage model formulation is identical to the derivation presented in Equations (6-9) through (6-13) with the fatigue life equations of Equations (6-9) and (6-10) replaced by Equations (6-14) and (6-15). The results of the evaluation are presented in Figures 6-18 and 6-19. A significant improvement in damage prediction is evident. Final damage estimates have increased and appear much closer to observed performance. However, only specimens A11 and A12 reach a final index of 1.0. The other four specimens show a damage index of approximately 0.8, which is typically representative of irreparable damage.

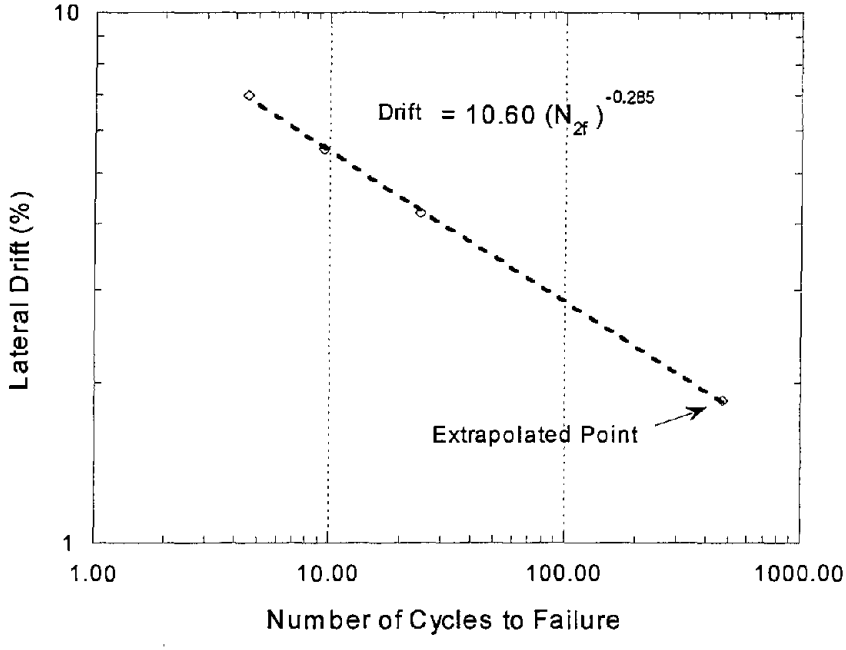

FIGURE 6-17 Fatigue Life Model for Total Lateral Drift of Well-Detailed Flexural Columns

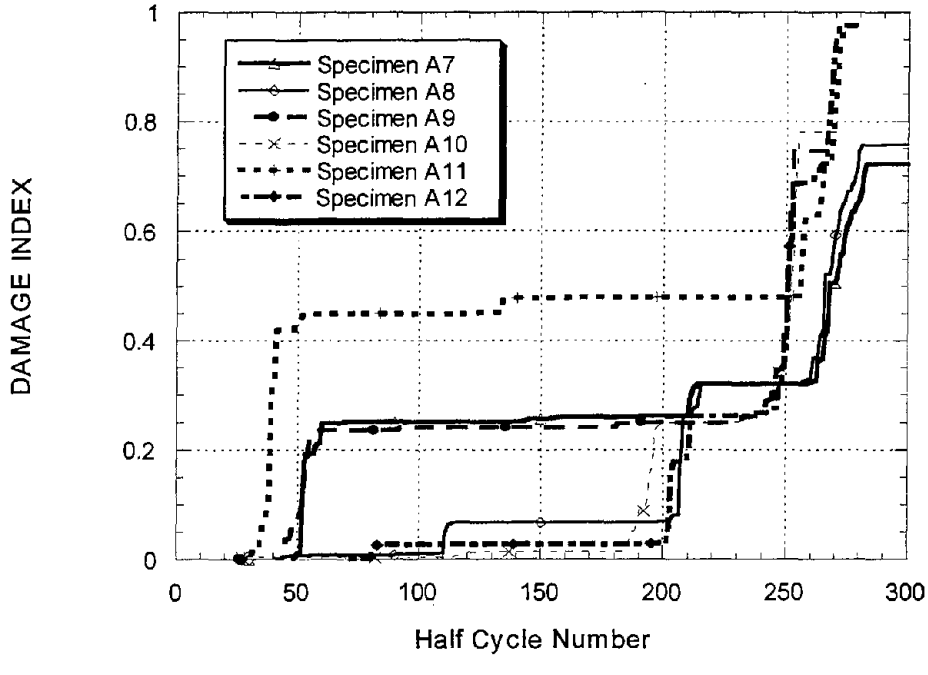

FIGURE 6-18 Performance of Proposed Plastic Strain Fatigue Damage Model Applied to Specimens A7-A12

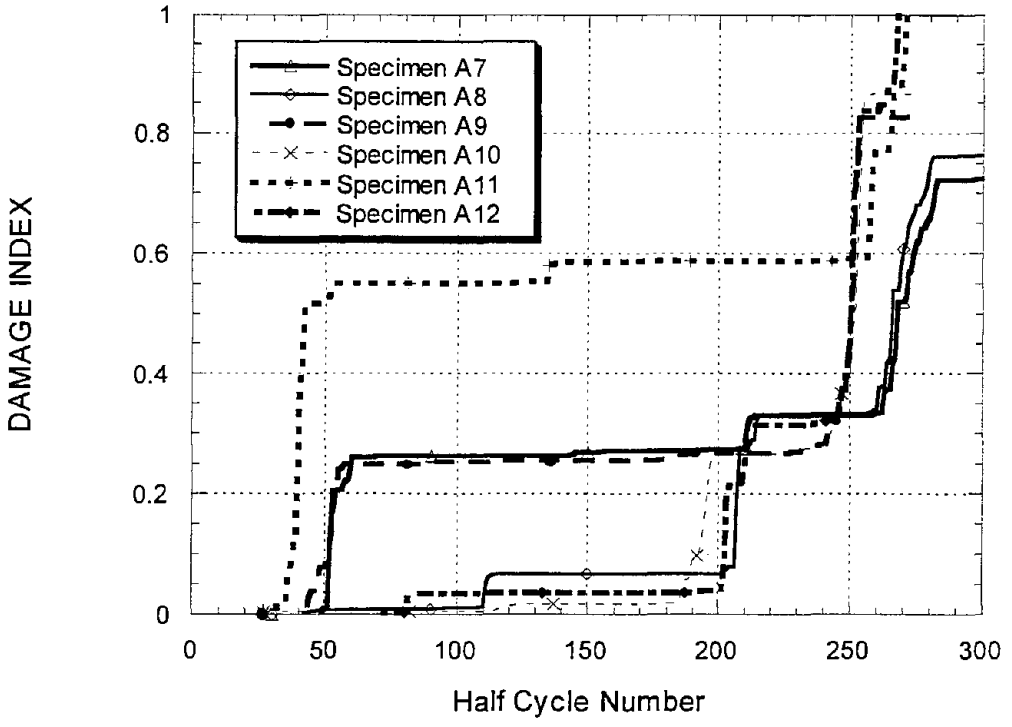

FIGURE 6-19 Performance of Proposed Total Strain Fatigue Damage Model Applied to Specimens A7-A12

7.0 RESEARCH FINDINGS AND CONCLUSIONS

This study was directed primarily towards the experimental and analytical investigation of cumulative damage. A major departure from past practice of laboratory testing that was pursued in this research effort was the development and use of random displacement histories rather than "standard" displacement cycles with increasing amplitudes. Related topics such as the effects of load path on damage and energy dissipation capacity, low-cycle fatigue failure of longitudinal reinforcing bars, and the influence of random cyclic loading on failure modes, were also studied. Given the complexity of the cumulative damage process and the innumerable parameters affecting the response, every effort was made to keep system variables to a minimum. Consequently, the imposed displacement history was the only variable introduced in the experimental testing.

This research investigation was limited to the study of circular columns with a predominantly flexural response. Circular sections have the advantage of possessing fairly uniform properties in any direction and are commonly used in bridge construction, particularly in seismic zones. The observations, findings and conclusions, therefore, are limited to seismically detailed flexural circular columns only. Additionally, the influence of soil-structure interaction and foundation flexibility were not considered. Failure, as defined in this study, is restricted to damage to the bridge pier only. Other potential damage sources such as foundation failure and deck-abutment connection failures are beyond the scope of this investigation.

7.1 Research Findings

Essential findings of this research study, given the limitations set forth in the previous paragraph, are summarized in this section. The inferences are subdivided into different categories, based on the nature of the finding. Most of the primary findings are damage related. Findings that shed further light on the concept of energy dissipation capacity are discussed separately. Likewise, contributions to inelastic modeling are summarized as a separate category.

7.1.1 Findings Related to Cumulative Damage

1. There exists a "threshold" ductility level for well-confined flexural circular columns designed by current CALTRANS (or AASHTO) specifications beyond which severe degradation of stiffness and strength takes place. For the bridge columns tested in this study, this threshold ductility level occurs between $3\Delta y$ and $4\Delta y$, which corresponds to a lateral drift between 4% and 5%. Specimen A3 which was cycled 150 times at a ductility of about 2% drift showed no significant signs of damage or deterioration. Specimen A5 which was cycled at a lateral drift of 5.5% failed in less than 10 cycles. It may, therefore, be stated that earthquakes which impose ductility demands less than 2.0 can survive a series of similar events without undergoing any significant structural damage. When the ductility demand approaches 4.0, the likelihood of moderate to severe damage is high and depends on the number of such inelastic cycles experienced by the structure.

2. Damage models evaluated in this study indicate that most non-fatigue based theories are

incapable of consistently reproducing observed damage. Models based on the degradation of a single structural parameter, such as the softening index evaluated in this study, are sensitive in the early stage of damage progression and show little variation beyond this point to failure, making them difficult to calibrate. Energy-based models, such as the Kratzig model, which do not account for the level of ductility at which energy is dissipated, consistently over-predict damage. The Park-Ang model is essentially a ductility-based model since the energy term is not adequately represented: energy damage is sometimes overestimated at small inelastic amplitudes and underestimated at large inelastic cycles. The Park-Ang model predicted failure of specimen A3 after 150 cycles which was contrary to observation. On the other hand, damage models based on fatigue-life expressions, using a Coffin-Manson rule in combination with Miner's hypothesis, account only for low-cycle fatigue of steel. It appears that a model which combines low-cycle fatigue failure in combination with confinement deterioration will yield excellent results. A simple fatigue life relationship was proposed, derived from the original work of Mander and Cheng (1995), based on the experimental data generated from constant-amplitude testing of specimens A3-A6, and was shown to produce improved damage prediction characteristics.

3. Under a sequence of predominantly low amplitude cycles, it is more probable that the confining spiral will fail prior to low-cycle fatigue failure of the longitudinal reinforcing bars. Conversely, if the bridge column is subjected to predominantly high amplitude inelastic cycles, it is more likely that the longitudinal bars will rupture before confinement failure occurs. In the present study of flexural columns, it was found that the threshold "low-amplitude" cycle is approximately 2% - 4% drift, while high-amplitude cycles are those in excess of 4% drift.

4. The use of random cycles provides a better means of understanding the phenomenon of cumulative damage. It is also a more reliable way of testing performance of structures subjected to low-cycle fatigue damage. Typical earthquakes impose few inelastic cycles and the energy demand is significantly different from the demand imposed by standard cyclic testing.

5. A large database of displacement histories were produced for the bridge column specimen using dozens of recorded ground motions at different soil profiles. A significant finding of this research study, based on these numerous analytical simulations, is the fact that typical earthquakes produce few large amplitude cycles, hence failure is generally governed by confinement rather than low-cycle fatigue of the longitudinal bars. However, damage from low-cycle fatigue of the longitudinal bars does contribute to overall damage though estimates of failure must include other failure modes. Damage models that attempt to predict flexural failure need to target failure modes resulting from confinement in greater detail.

6. In an attempt to correlate visually observed damage during testing with damage limit states, all recorded test data were evaluated carefully to develop a correlation chart. This chart provides a convenient aid in post-earthquake reconnaissance evaluation of structural safety. This summary is presented in Table 7-1.

TABLE 7-1 Correlation of Damage Limit States with Visual Observations

Damage Indicator	Damage State	Description	Visual Observation Based on current Testing
N	None	No visible damage, either cosmetic or structural	No visible cracks
I	Insignificant	Damage requires no more than cosmetic repair. No structural repairs necessary	Hair-line cracks Minor spalling No exposed reinforcement
M	Moderate	Repairable structural damage has occurred. The existing elements can be repaired essentially in place, without substantial demolition or replacement of elements	Excessive spalling Exposed reinforcement No buckling of longitudinal bars No necking of spirals
H	Heavy	Damage is so extensive that repair of elements is either not feasible or requires major demolition or replacement.	Buckling/fracture of longitudinal bars Necking/rupture of spirals

7.1.2 Findings Related to Energy-Dissipation Capacity

The constant amplitude and random cyclic testing clearly indicate that the energy capacity of a member at failure is strongly path (history) dependent. Proof of this observation is clearly evident in Figures 7-1 and 7-2 which show plots of cumulative energy dissipated for all specimens tested in both phases of the study. Figure 7-1 is a summary of specimens tested under standard and constant-amplitude cycles in Phase I while Figure 7-2 shows the history of dissipated energy for specimens tested under random loads in Phase II. If specimen A2, tested under standard cyclic displacement amplitudes, is referred to as the benchmark energy capacity, it is evident that the energy capacity of the columns vary considerably depending on the displacement amplitude and path.

Standard cyclic testing may provide information on the behavior of members and the potential effects of certain material and geometric parameters on seismic response, but must not and can not be used as a measure of energy-capacity of members.

7.1.3 Findings Related to Inelastic Modeling

Another contribution from the results of this study is the identification of inelastic behavior at small amplitudes. This information is useful in the development of hysteresis models used in nonlinear programs for dynamic response analysis. To date, most hysteresis models make fairly arbitrary assumptions on the hysteretic loop behavior for small amplitude cycles which are enveloped by larger amplitude cycles. The experimental findings in this study provide direct input into this modeling process.

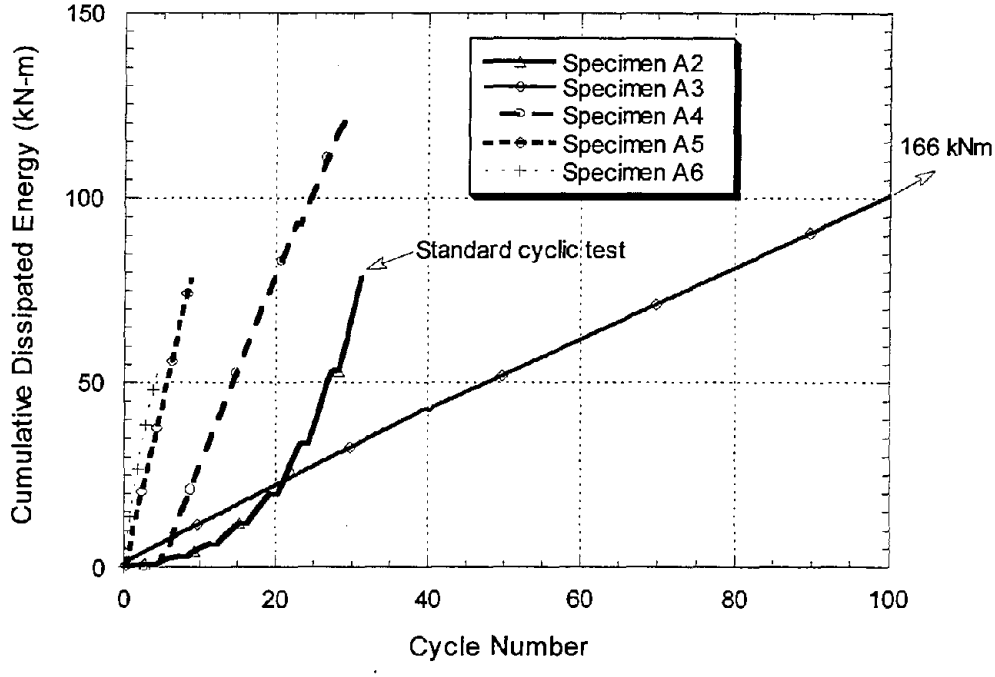

FIGURE 7-1 Cumulative Energy to Failure of Bridge Columns Subjected to Constant Amplitude Loading

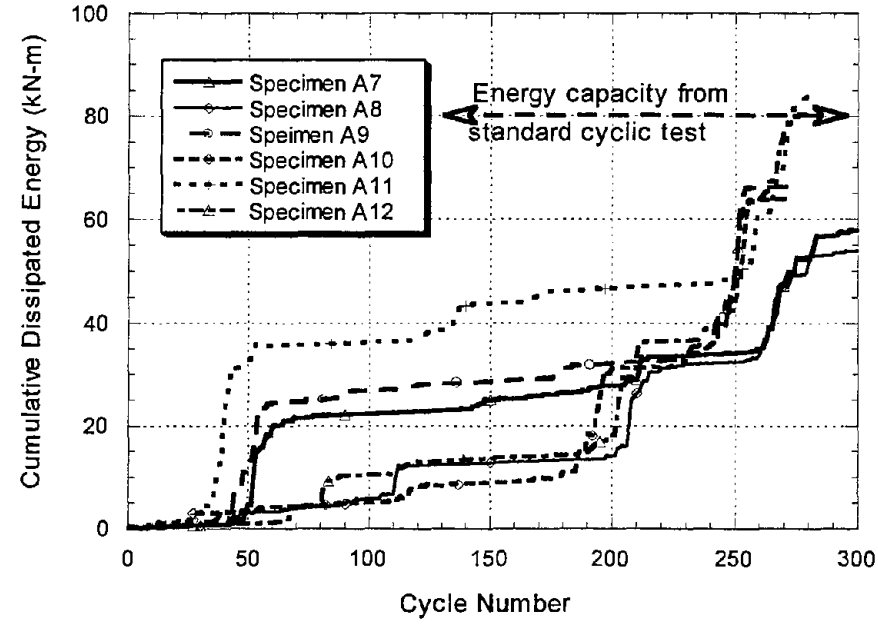

FIGURE 7-2 Cumulative Energy to Failure of Bridge Columns Subjected to Random Loading

Figure 7-3 shows segments of the experimental response for two of the specimens in which a few relevant cycles are separated from the rest of the force-deformation loops. A well-known aspect of loop behavior is clearly evident: that unloading paths generally attempt to return to the location of displacement and/or force at the end of the previous half cycle. The path taken to return to this previous amplitude location may vary depending on the current location of unloading. The purpose of displaying intermediate force-displacement hysteresis in Figure 7-3 is to facilitate the development of a model that can be used for earthquake analysis of concrete structures. Figure 7-4 is a proposed model of expected loop behavior under random amplitudes wherein the path of small-amplitude cycles are given proper consideration.

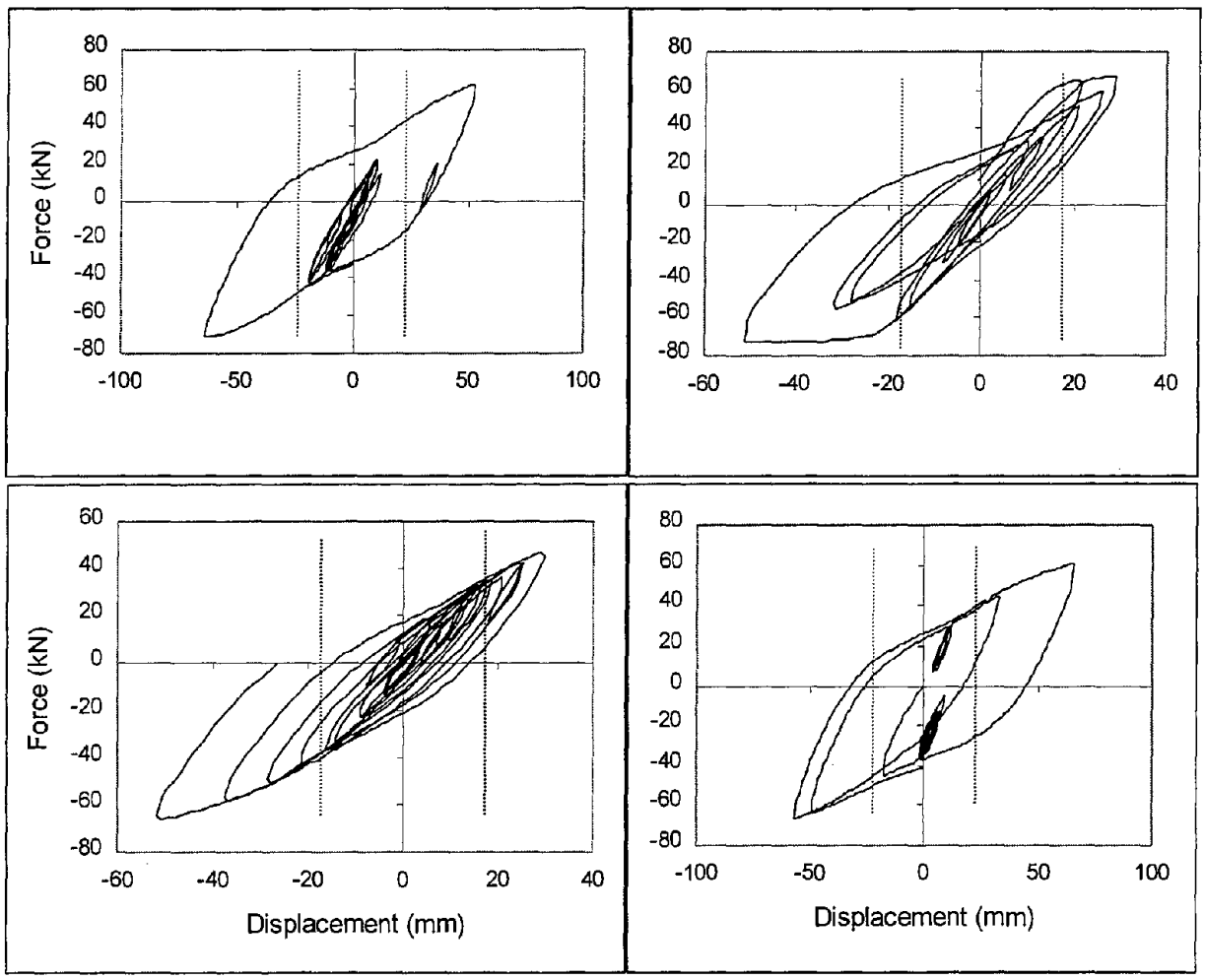

FIGURE 7-3 Local Loop Behavior Under Random Cyclic Response

If unloading occurs within a displacement amplitude less than the yield displacement, unloading paths seem to directly target the previous maximum point (shown by paths 'd' and 'e' in Figure 7-4) as opposed to unloading paths beyond the yield displacement which show the ability to dissipate more energy (paths 'c1' and 'c2' in Figure 7-4). (c) If reloading occurs along an unloading path before the zero force axis is crossed, it is reasonable to reload along the same line without energy dissipation (paths aa' and bb').

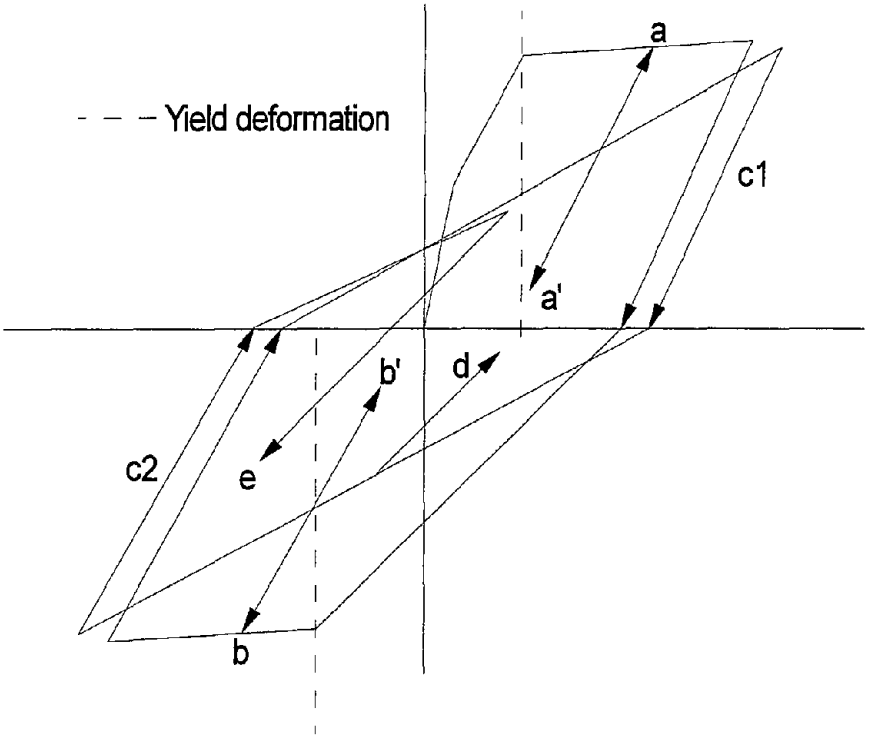

FIGURE 7-4 Proposed Modeling of Local Hysteresis Loops

7.2 Development of Performance-Based Design for Bridge Columns

One of the primary objectives of this research was to formulate a performance based methodology for seismic design of bridge piers. This design procedure should be capable of allowing the structural engineer to evaluate the adequacy of a reinforced concrete bridge pier against expected seismic action. Based on the findings of this study, and the fatigue life expression for flexural columns presented in Section 6.4, the following simple procedure is proposed:

a) Establish a series of ground motions from seismological prediction and/or historical records that best fit the bridge site. This would constitute the site-specific loading criteria.

b) Conduct an inelastic time history analysis of the bridge pier for each of the series of the selected records.
c) Determine the seismic demand from results of the preceding analysis in terms of number of half cycles at each drift amplitude.
d) Equation (6-16) can be utilized to define the degree of damage resulting from each half cycle at a given drift amplitude. Solving Equation (6-16) in terms of number of cycles to failure yields:

$$N_{fi} = 2.0 * \left(\frac{Drift}{10.6} \right)^{3.51} \qquad (7\text{-}1)$$

The quantity 2.0 accounts for the fact that only a half-cycle is being considered. Calculate the induced damage to the column using the following expression:

$$D.I. = \sum \frac{n_{di}}{N_{fi}} \qquad (7\text{-}2)$$

where n_{di} is the number of half cycles at a particular drift *"di"* obtained from the analysis indicated in step (a), and N_{fi} is the number of half cycles to failure at the same drift *"di"* obtained from Equation (7-1).

e) If the demand, based on the computed damage index, is close to or exceeds 1.0, then the bridge will either not survive the expected earthquake activity at the site under consideration or suffer irreparable damage. In fact, for practical considerations, values of the above damage index in excess of 0.75 would indicate a high probability of severe damage.

The above steps can also be used to estimate reserve capacity of a bridge column following a seismic event if recorded data at the site is available to estimate the drift response during the event.

7.4 Recommendations for Future Research

This research effort must be viewed as a preliminary attempt that contributes to the overall effort in calibrating a fatigue-based cumulative damage model which is a necessary first step towards developing a performance-based design guideline. The study provided a number of useful insights into the mechanics of damage progression and brought to the forefront a number of issues that still remain unresolved. The following recommendations for future work are based on the findings of this project:

1. The response of bridge columns with a much smaller aspect ratio must be investigated using essentially the same approach adopted in this study. This will highlight modes of shear failure as well as the applicability of fatigue-life expressions for elements responding primarily in shear.

2. A simple experimental study on the fatigue behavior of deformed reinforcing bars subjected to random cyclic loads needs to be investigated. Since the behavior of flexural elements is controlled largely by the response of the steel reinforcement, this study will provide the basis for developing future test programs that examine cumulative fatigue in RC members. In particular, the inter-dependence of small and large amplitude inelastic cycles must be studied to determine load path effects.
3. Circular columns were used in this study to limit the number of system variables. It is recommended to extend this study to rectangular columns to investigate effects of shape and cross-section aspect ratio. The study of rectangular columns should obviously cover both flexure and shear.
4. A final aspect of behavior that may deserve some attention is the influence of bidirectional moments on the deterioration and damage of bridge columns. Since bridge piers are constrained to respond in the lateral direction of the bridge span due to the relatively large deck that forces motion in the in-plane direction, it is unlikely that biaxial bending is a serious concern in bridge design. The use of circular columns also avoids this issue.
5. This testing methodology may also be extended to single bay bridge bents in which the interaction of the deck beams becomes significant. Single and double deck bents are common in highway construction. Testing such models at a realistic scale is time-consuming and difficult. Analytical studies of such structures using validated damage models can provide useful information.
6. Tests of retrofitted specimens may also be investigated using the test methodology presented in this report. The reliability and adequacy of proposed retrofit and rehabilitation techniques can be readily evaluated by examining the response of the original and repaired specimen under the same sequence of random load reversals.
7. Existing damage models need to be enhanced and improved to account adequately for damage resulting from different failure modes. In the present testing, it was obvious that failure was a combination of low-cycle fatigue damage and the deterioration of confining action of the spirals. The fatigue-life expressions proposed by Mander and Cheng (1995) were extended to composite concrete columns based on limited experimental testing. However, the proposed model needs to be enhanced further to better characterize damage resulting from other failure modes.

A performance-based design procedure wherein damage limit states can be identified is urgently needed by the profession. The proposed procedure in Section 7.3 must be viewed as an initial step in this direction.

References

AASHTO (1989), "Standard Specifications for Highway Bridges", (14th Edition), The American Association of State Highway and Transportation Officials (AASHTO), Washington, D.C.

ACI Design Handbook, (1985), Columns, Volume 2, Publication SP 17A, American Concrete Institute, Detroit, Michigan.

Ang, B.G., Priestley, M.J.N., and Paulay, T., (1985), "Seismic Shear Strength of Circular Bridge Columns", Research Report 85-5, Department of Civil Engineering, University of Canterbury, Christchurch, New Zealand, 408 pp.

Ang, B.G., Priestley, M.J.N., and Paulay, T., (1989), "Seismic Shear Strength of Circular Bridge Columns", ACI Structural Journal, Vol.86, No.1, pp. 45-59.

Building Research Institute (1975, 1978), "A Seismic Analysis of Building Structural Members: a List of Experimental results on Deformation Ability of Reinforced Concrete Column Under Large Deflection", No. 3, B.R.I., Ministry of Construction, Japan, 182 pages.

CALTRANS (1992), "Bridge Design Specifications," State of California, Department of Transportation, Office of Structure Design, Sacramento, California.

Cheok, G.S., and Stone, W.C., (1986), "Behavior of 1/6 Scale Model Bridge Columns Subjected to Cyclic Inelastic Loading", Report No. NBSIR 86-3494, U.S. Department of Commerce, , National Institute of Standards and Technology, Gaithersburg, MD, 270 pp.

Cheok, G.S., and Stone, W.C., (1990), "Behavior of 1/6 Scale Model Bridge Columns Subjected to Cyclic Inelastic Loading", ACI Structural Journal, Vol. 87, No. 6, pp. 630-638.

Chung, Y.S., Meyer, C. and Shinozuka, M., (1987), "Seismic Damage Assessment of RC Structures", NCEER Report 87-0022, State University of New York at Buffalo, New York.

Coffin, L. F. Jr., (1954), "A Study of the Effects of Cyclic Thermal Stresses on a Ductile Metal", Transactions of the American Society of Mechanical Engineers, New York, N. Y., 76, 931-950.

Davey, B.E., (1975), "Reinforced Concrete Bridge Piers Under Seismic Loading", Master of Engineering Report, Civil Engineering Department, University of Canterbury, Christchurch, New Zealand, February.

Hwang, T.H. and Scribner, C.F., (1984), "RC Member Cyclic Response During Various Loadings", Journal of Structural Engineering, ASCE, 110 (3), pp. 466-489.

Kanaan, A. and Powell, G.H., (1973). "General Purpose Computer Program for Inelastic Dynamic response of Plane Structures", EERC Report No.73-6, University of California, Berkeley.

Kratzig, W.B. and Meskouris, M., (1987), "Nonlinear Seismic Analysis of Reinforced Concrete Frames", Earthquake Prognostics (Vogel and Brandes, editors), Verlag Friedr, Vieweg and Sohn, Braunschweig, pp.453-462.

Kunnath, S.K., and Reinhorn, A.M., (1995), "Efficient Modeling Scheme for Transient Analysis of Inelastic RC Structures", Microcomputer in Civil Engineering, Vol.10, No.1, pp. 97-110.

Kunnath, S.K., Mander, J.B. and Lee, F., (1997), "Parameter Identification for Degrading and Pinched Hysteretic Structural Concrete Systems", Engineering Structures, Vol.19, No.3, pp.224-232.

Kunnath, S.K., Reinhorn, A.M and Lobo, R.F., (1992), "IDARC: Inelastic Damage Analysis of RC Structures- Version 3.0", Report NCEER-92-0022, State University of New York at Buffalo, New York.

Mander, J. B., Panthaki, F. D., and Kasalanati, A., (1994), " Low Cycle Fatigue Behavior of Reinforcing Steel", Journal of Materials in Civil Engineering, ASCE, Vol. 6, No. 4.

Mander, J.B. and Cheng, C.-T., (1995), "Renewable Hinge Detailing for Bridge Columns", Pacific Conference on Earthquake Engineering, Melbourne, Australia, November 20-22.

Mander, J.B. and Cheng, C.-T., (1995), "Replaceable Hinge Detailing for Bridge Columns", National Seismic Conference on Bridges and Highways, San Diego, CA, December 10-13.

Mander, J.B., Priestley, M.J.N., and Park, R., (1984), "Seismic Design of Bridge Piers", Research Report 84-2, University of Canterbury, Christchurch, New Zealand.

Mander, J.B., Priestley, M.J.N., and Park, R., (1988), "Observed Stress Strain Behavior for Confined Concrete", Journal of Structural Engineering, ASCE, 114 (8), pp. 1827-1849.

Mander, J.B., Priestley, M.J.N., and Park, R., (1988), "Theoretical Stress Strain Model for Confined Concrete", Journal of Structural Engineering, ASCE, 114 (8), pp. 1804-1826.

Manson, S. S., (1953), "Behavior of Materials under Conditions of Thermal Stress", Heat Transfer Symposium, University of Michigan Engineering Research Institute, Ann Arbor, Michigan, pp. 9-75.

Miner, M.A., (1945), "Cumulative Damage in Fatigue", Journal of Applied Mechanics, Vol.12, pp. A-159.

Munro, I.R.M., Park, R., and Priestley, M.J.N., (1976), "Seismic Behavior of Reinforced Concrete Bridge Piers", Report 76-9, Department of Civil engineering, University of Canterbury, Christchurch, New Zealand.

Newmark, N.M., (1959), "A Method of Computation for Structural Dynamics", ASCE Journal of Engineering Mechanics, Vol.85, pp.67-94.

Park, Y.J. and Ang, A.H-S., (1985), "Mechanistic Seismic Damage Model for Reinforced Concrete", Journal of Structural Engineering, ASCE, 111, pp. 722-739.

Powell, G. and Allahabadi, R., (1988), "Seismic Damage Prediction by Deterministic Methods: Concepts and Procedures", Earthquake Engineering and Structural Dynamics, Vol.16.

Priestley, M.J.N and Benzoni, G., (1996), "Seismic Performance of Circular Columns with Low Longitudinal Reinforcement Ratios", ACI Structural Journal, Vol. 93, No.4, pp.474-485.

Priestley, M.J.N. and Paulay, T., (1992), "Seismic Design of Reinforced Concrete and Masonry Buildings", John Wiley and Sons, New York.

Priestley, M.J.N., Seible, F. and Anderson, D.L., (1993), "Proof test of a Retrofit Concept for the San Francisco Double-Deck Viaducts: Part 1 – Design Concept, Details and Model", ACI Structural Journal, Vol. 90, No.5, pp. 467-479.

Priestley, M.J.N., Seible, F. and Anderson, D.L., (1993), "Proof test of a Retrofit Concept for the San Francisco Double-Deck Viaducts: Part 2 – Test Details and Results", ACI Structural Journal,
Vol. 90, No.6, pp. 616-631.

Priestley, M.J.N., Seible, F., Xiao, Y. and Verma, R., (1994), "Steel Jacket Retrofitting of Reinforced Concrete Bridge Columns for Enhanced Shear Strength – Part 1: Theoretical Considerations and Test Design", ACI Structural Journal, Vol. 91, No.4, pp. 394-405.

Priestley, M.J.N., Seible, F., Xiao, Y. and Verma, R., (1994), "Steel Jacket Retrofitting of Reinforced Concrete Bridge Columns for Enhanced Shear Strength – Part 2: Test Results and Comparison with Theory", ACI Structural Journal, Vol. 91, No.5, pp. 537-551.

Stone, W.C. and Cheok, G.S., (1989), "Inelastic Behavior of Full-Scale Bridge Columns Subjected to Cyclic Loading", NIST Building Science Series Report No. 166, U.S. Department of Commerce, National Institute of Standards and Technology, Gaithersburg, MD, 252 pp.

Stone, W.C., Cooper, J. D. and Carino, N. J., (1990), "Performance of Bridge and Highway Structures", NIST SP No. 778, National Institute of Standards and Technology, Gaithersburg, MD, 201 pp.

Tanaka, H. and Park, R., (1993), "Seismic Deisgn and Behavior of Reinforced Concrete Columns with Interlocking Spirals", ACI Structural Journal, Vol. 90, No.2, pp.192-203.

Williams, M.S., & Sexsmith, R.G. (1994), "Review of Methods Assessing Seismic Damage in Concrete Structures", Technical Report 94-02, Earthquake Engineering Research Facility, University of British Columbia, Canada.

Wong, Y.L., Paulay, T., and Priestley, M.J.N., (1990), "Squat Circular Bridge Piers Under Multi-Directional seismic Attack", Department of Civil Engineering, University of Canterbury, Report 90-4, 264 pp.

Wong, Y.L., Paulay, T., and Priestley, M.J.N., (1993), "Response of Circular Columns to Multi-Directional Seismic Attack", ACI Structural Journal, Vol. 90, No. 2, pp.180-191.

Appendix : Ultrasonic Testing

Non-destructive test methods are gaining popularity these days as a potential means of monitoring damage in structures. If it is possible to calibrate such methods with damage limit states, they could contribute to the overall effort of performance-based design.

Hence, in addition to the force-deformation hysteresis and strain gage data recorded during testing of the bridge columns reported in Sections 4 and 5, minimal non-destructive tests of the specimens were also carried out. The non-destructive methodology employed here consisted of ultrasonic measurements across the height of the specimen before and after testing. Measurements could not be taken during testing since the extraneous vibrations and noise of the hydraulic system to which the test specimen was anchored interfered with the ultrasonic readings. As such, it was not possible to calibrate the data with observed damage during testing. Rather, the testing was conducted primarily as a feasibility study.

Results of the ultrasonic measurements are presented in Figures A-1 through A-9. It is clear that damage is reflected through an increase in travel time of the sound waves. Also encouraging is the fact that the change in travel time increases non-linearly with the degree of damage (see variation across height of specimen). These preliminary studies indicate that such methodologies hold promise in damage measurement and could be calibrated for use in performance-based evaluat

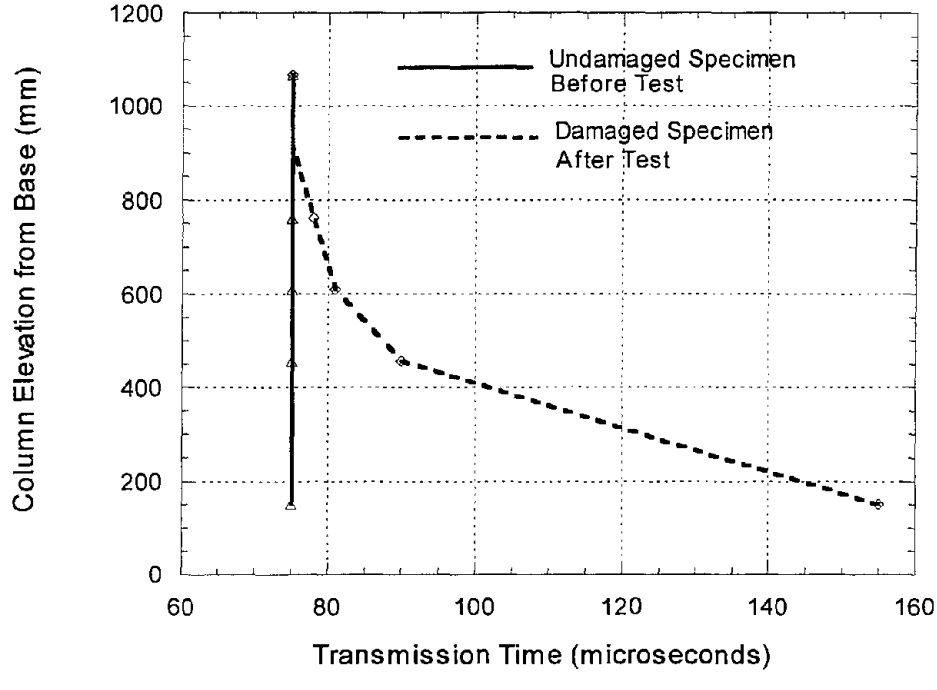

FIGURE A-1 Ultrasonic Readings Across Height of Specimen A4

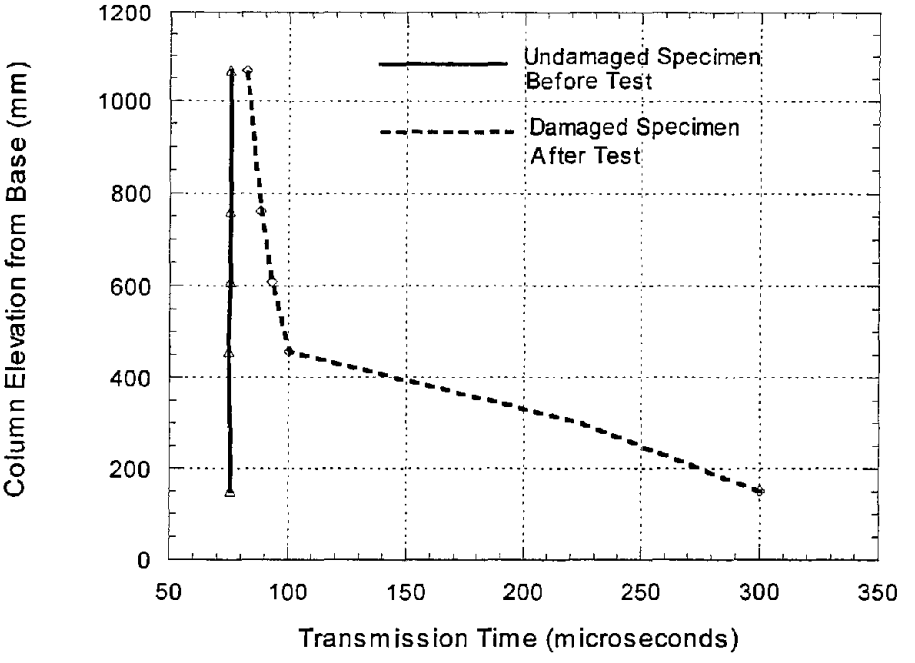

FIGURE A-2 Ultrasonic Readings Across Height of Specimen A5

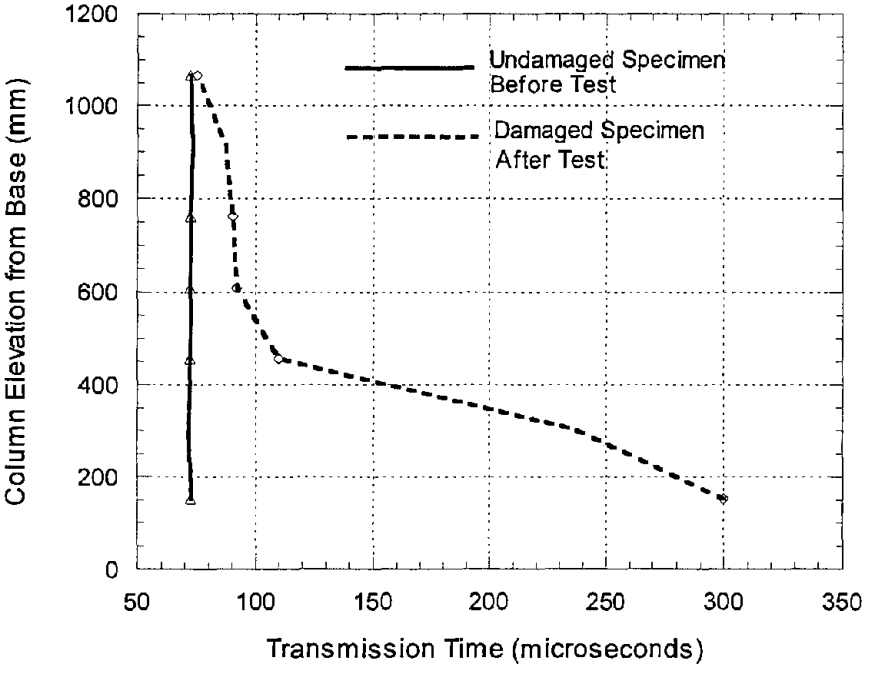

FIGURE A-3 Ultrasonic Readings Across Height of Specimen A6

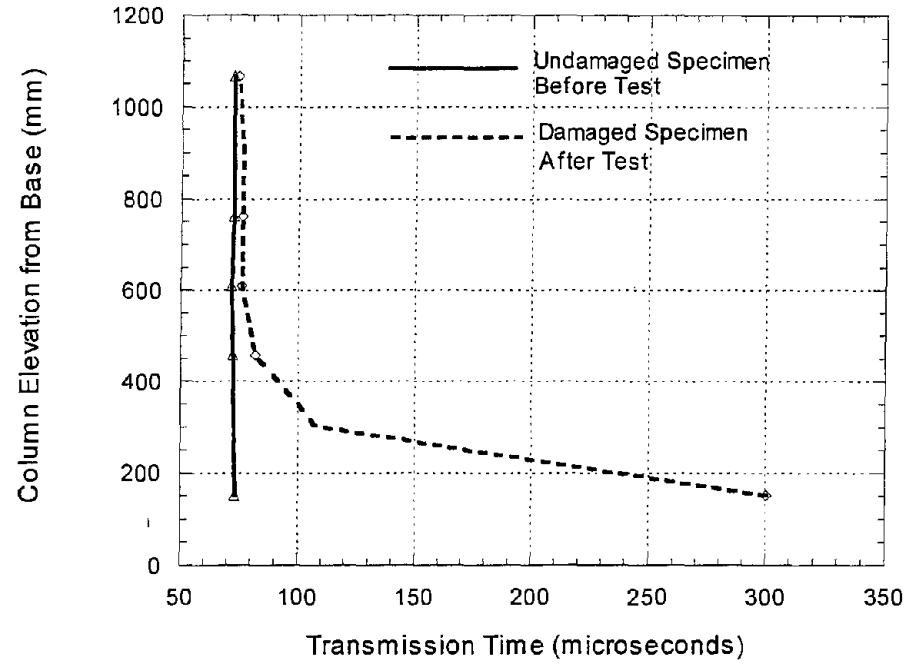

FIGURE A-4 Ultrasonic Readings Across Height of Specimen A7

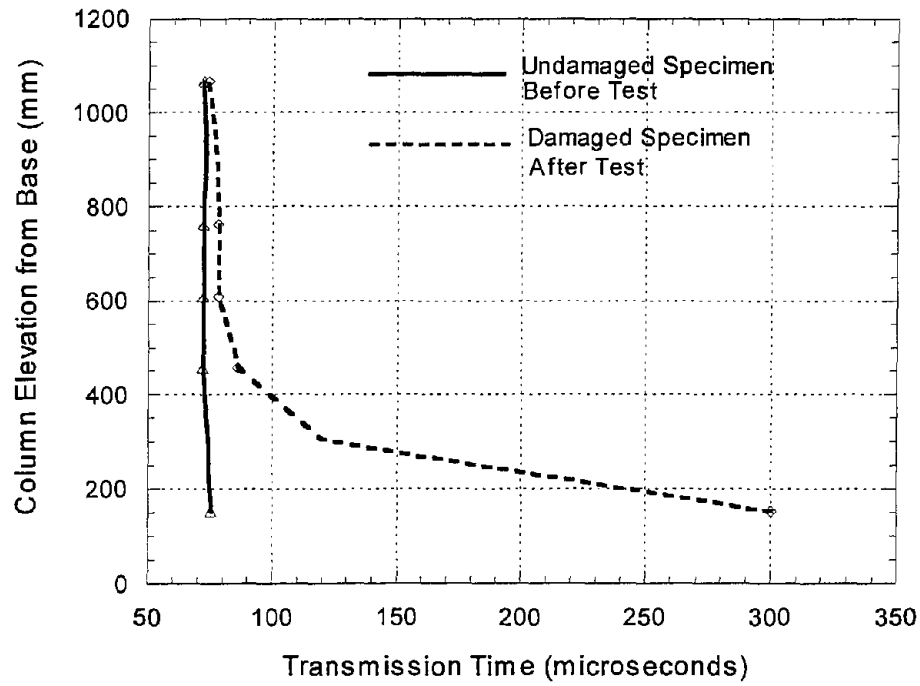

FIGURE A-6 Ultrasonic Readings Across Height of Specimen A9

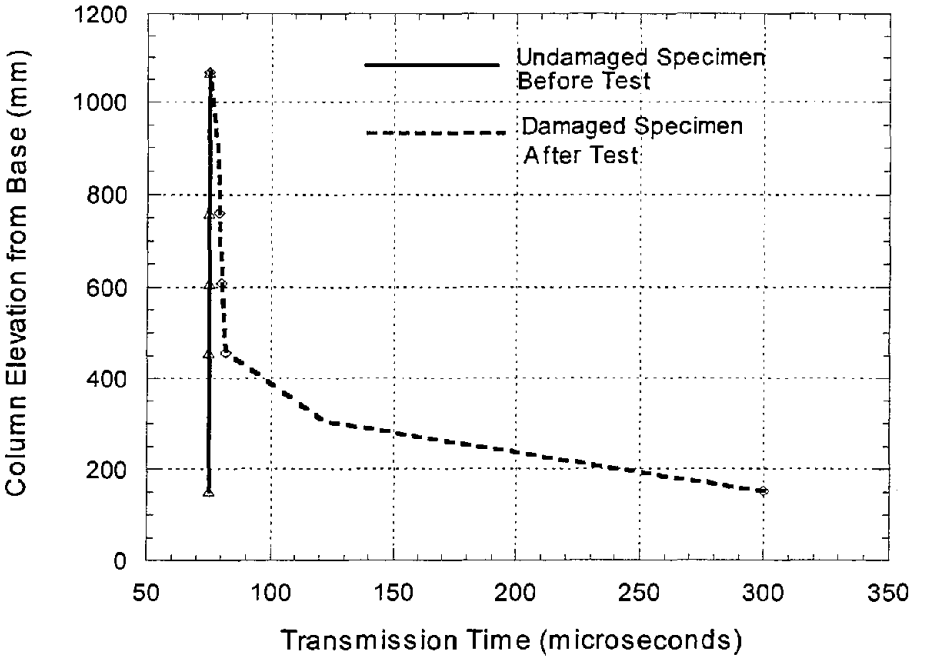

FIGURE A-7 Ultrasonic Readings Across Height of Specimen A10

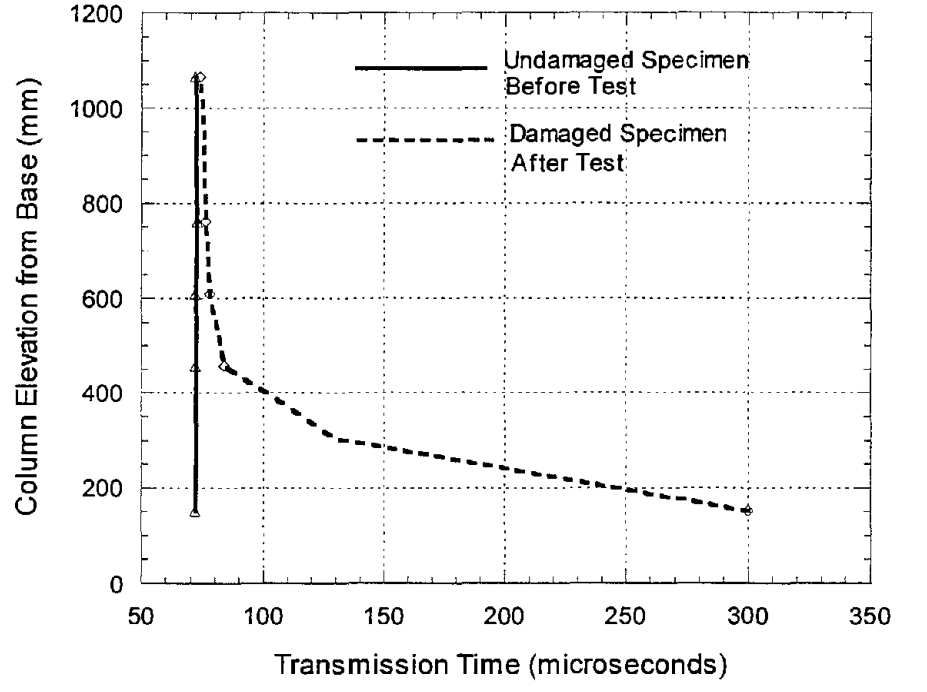

FIGURE A-8 Ultrasonic Readings Across Height of Specimen A11

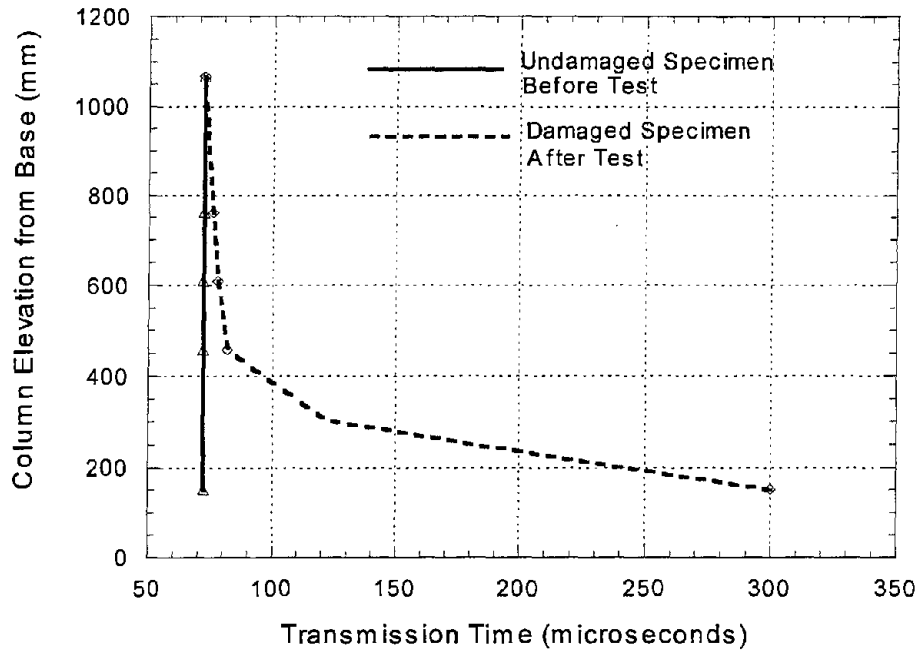

FIGURE A-9 Ultrasonic Readings Across Height of Specimen A12